# TELLURIUM SELENIDE-GADOLINIUM TUNGSTEN OXIDE QUANTUM DOT MATERIAL FOR SUPERCAPACITOR


By

**SINETHEMBA KABA**

(BSc Honours in Chemistry, Nelson Mandela University)

**A mini-thesis submitted in fulfilment of the requirement for the degree**

**of**

**MAGISTER SCIENTIAE IN NANOSCIENCE**

In the

**Faculty of Sciences, University of Western Cape, South Africa**

**Supervisors: Prof Emmanuel Iwuoha**

**Co-supervisors: Dr Chinwe O. Ikpo, Dr Assumpta C. Nwanya and Dr Miranda M. Ndipingwi**

**January 2022**

# ABSTRACT

Renewable energy has become the main alternative solution to the "energy crisis" the world is faced with. A supercapacitor is one of the energy storage devices capable of storing and releasing energy at a higher rate compared to other traditional devices but in order to capture and release this energy, suitable electrode materials are needed. In this work, hydrothermal synthesis, structure and electrochemical characterization of a newly developed tellurium selenide-gadolinium tungsten oxide quantum dot material for supercapacitor is presented. XRD results of the composite material revealed the presence of phases from the starting materials (i.e. $Gd_2(WO_4)_3$ and $Te_{0.39}Se_{0.61}$). Reflection peaks of the parent material $Gd_2(WO_4)_3$ were retained in the composite material with new additional peaks characteristic to $Te_{0.39}Se_{0.61}$. Annealing temperature variation of the composite material gave us a clear indication that at temperatures up to 700 °C the composite becomes amorphous but beyond 800 °C, becomes well crystalline in nature. EDS results gave us a confirmation that all elements from $Gd_2(WO_4)_3$ and $Se_{0.61}Te_{0.39}$ were present except selenium that was not detected in the composite material. The reason for this lies with the possibility of overlap between REE with selenium. EDS is unable to resolve the peak overlaps with Pr, Eu, Gd, Ho, Er, Tm, and Lu. The internal structure from HRTEM revealed a cubic structure for $Gd_2(WO_4)_3$ and there was no clear information about the structure of the composite. Furthermore, the band gap energy determined from UV-vis is 3.28 eV for $Gd_2(WO_4)_3$ and after incorporation $Te_{0.31}Se_{0.61}$, slightly increased to 3.39 eV for $Gd_2(WO_4)_3/Te_{0.39}Se_{0.61}$. The electrochemistry of all the synthesized materials was studied in a three-electrode system using 2 M KOH as an electrolyte. From the CV, the current peak ratio determined was not equal to 1 which indicated a quasi-reversible system and the current response were increasing with increasing scan rates of which both these characteristics belong to battery-type electrodes. Specific capacitance values were calculated from GCD, and higher values were achieved at low current density of 1.2 A $g^{-1}$. The calculated values were 64 .3 C $g^{-1}$, 17.3 C $g^{-1}$ and 23.8 C $g^{-1}$ for $Gd_2(WO_4)_3$, $Te_{0.39}Se_{0.61}$ and $Gd_2(WO_4)_3/Te_{0.39}Se_{0.61}$, respectively. $Gd_2(WO_4)_3$ showed superior electrochemical performance compared to the composite. GCD formed sloping and plateau regions confirming battery-type electrode characteristics. Even though $Gd_2(WO_4)_3$ showed superior performance, the composite was leaning towards a more pseudocapacitive nature.

# GRAPHICAL REPRESENTATION

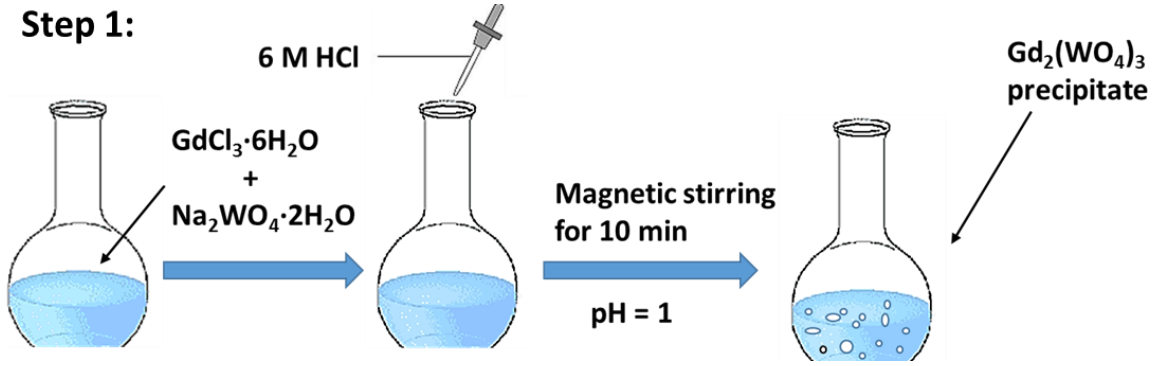


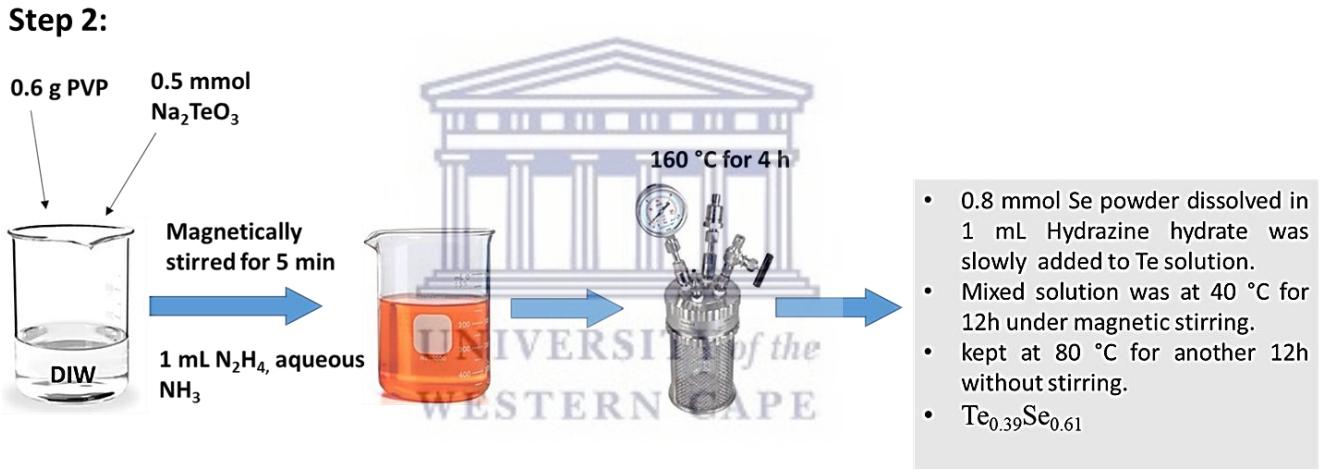


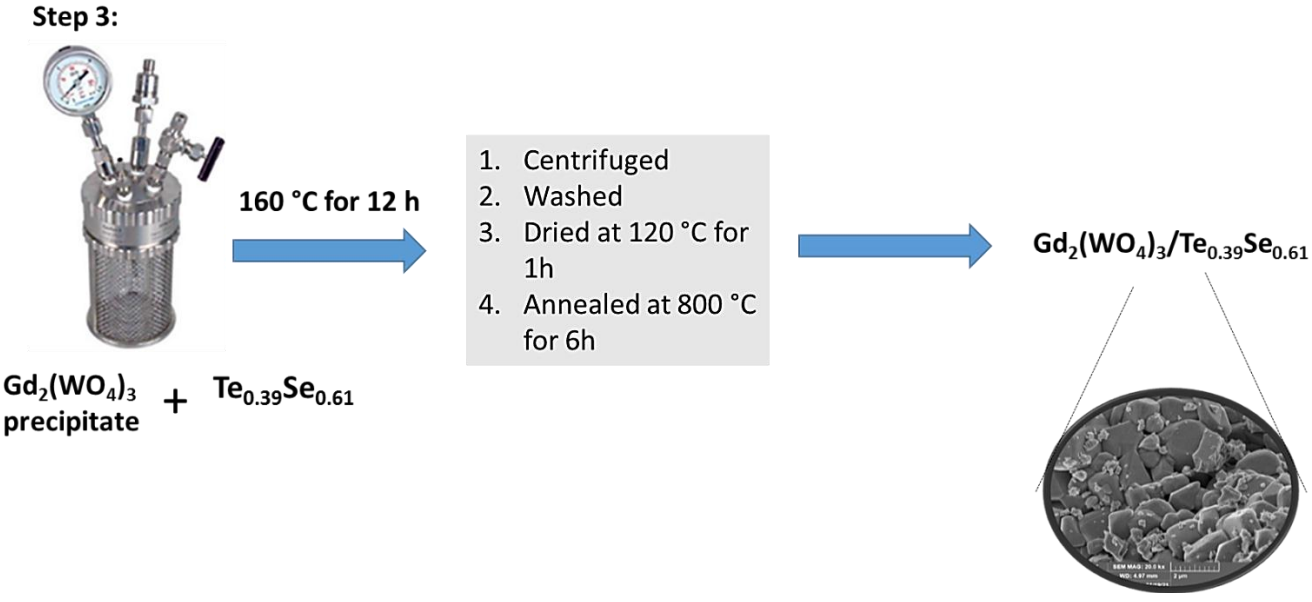

# DECLARATION

I declare that **"Tellurium selenide-gadolinium tungsten oxide quantum dot material for supercapacitor"** is my own work, that it has not been submitted before any degree or examination in any other university, and that all the sources I have used or quoted have been indicated and acknowledged as complete references.

Signature 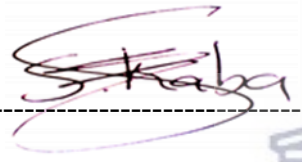 ----------

**Sinethemba Kaba** **February 2022**

# DEDICATION

This work is dedicated to my family and friends; Mr Xhasumzi Clifford Meva (Father), Miss Nomathemba Julia Kaba (Mother), Mr Vuyolwethu Meva (brother), Miss Olwethu Meva (sister), Miss Asanda Meva (sister), Miss Asalinto Mhlantla (sister), Mr hlumelo Nomntayi (brother), Mr Awomi Sikroba (son), Miss Nokuthula Sikroba (best friend), Mr Wandisile Siciko (friend), Mr Siyamyaleza Aviwe Brukwe (friend), Miss Zandile Mali (friend) for their patience, love, prayers and moral support throughout the process.

# ACKNOWLEDGEMENT

Firstly, I would like to thank the almighty God for carrying and giving me strength throughout this journey, even though he has granted us brains to carry out the tasks but I wouldn't have made it without his will "Jeremiah 29:11; For I know the plans I have for you, plans not to harm you but to prosper you, plans to give you hope and a future". For that I thank you Lord.

I would like to express my deepest gratitude to my supervisor Prof Immanuel Iwuoha for his expert guidance.

I would also like to extend my gratitude to my mentor Dr Miranda Ndipingwi for her enthusiastic encouragement and support when I was at my lowest point.

I would like to thank Dr Waryo for availing himself for any advice needed, and instrument related matters. I would also like to thank each and every member of the sensor lab for making the work environment friendly and easier to work in.

To my family and friends for their support, love and encouragement in my studies.

I would also love to extend my gratitude to MSc nanoscience Scholarship for financial support and to everyone who contributed to my studies, and played a role to my journey and made it possible to be where I am today.

# LIST OF PUBLICATIONS

1. Mabokela TE, Nwanya AC, Ndipingwi MM, Kaba S, Ekwere P, Werry ST, et al. Review—Recent Advances on High-Capacity Li Ion-Rich Layered Manganese Oxide Cathodes. J Electrochem Soc. 2021.

# TABLE OF CONTENTS

Abstract……...…….....i

Graphical representation……...…… ii

Declaration……...…...…… iii

Dedication……...…...……... iv

Acknowledgements……...…...…….…….... v

List of publications……vi

Table of Contents……..…….... vii

List of figures……...…….…...…xi

List of Tables…….…… xiii

Acronyms and Abbreviations…… xiv



## CHAPTER 1

1.0 Introduction...……...……1

1.1 Background……...…....1

1.2 Problem Statement……...…….……....3

1.3 Rationale and Motivation……...…….…4

1.4 Aim and Objectives……...……...…...5

1.4.1 Aim……...…...5

1.4.2 Objectives……...….5

1.5 Thesis Structure……...….6

1.6 References……...….7

## CHAPTER 2

2. Literature Review……...……...……...……...11

2.1 Background……...……..……11

2.1.1 Rare Earth Elements (REEs)……...……...11

2.2 Synthetic Routes for lanthanum tungstates……13

2.2.1 Sonochemical method……..……13

2.2.2 hydrothermal method……...……14

2.2.3 Solid-state method……...……15

2.2.4 Electrospinning method……....……...…16

2.3 Formulation of lanthanum tungstates……...……17

2.3.1 Tungsten oxide ……...……17

2.3.2 Lanthanum doped tungsten oxide……..……...……22

2.3.2.1 Lanthanum doped tungsten oxide based supercapacitor applications.....…….24

2.4 Conclusion……..……..…27

2.5 References……..……29

## CHAPTER 3

3 Experimental……..……40

3.1 Materials and Reagents……..……..….40

3.2 Chemical synthesis……41

3.2.1 Hydrothermal synthesis of $Gd_2(WO_4)_3$…….41

3.2.2 Hydrothermal synthesis of $Te_ySe_x$……..41

3.2.3 One pot synthesis of $Gd_2(WO_4)_3/Te_ySe_x$……42

3.3 Analytical techniques……43

3.4 References……51

## CHAPTER 4

4. Results and Discussion…….54

4.1 Structural characterization……...…...54

4.1.1 Fourier Transform Infrared Spectroscopy……54

4.1.2 X-ray Diffraction……...……57

4.2 Surface morphology characterization……61

4.2.1 Scanning Electron Microscopy……...…...61

4.2.1 Energy Dispersive Spectroscopy……...61

4.3 Internal Structure characterization…….……65

4.3.1 Transmission Electron Spectroscopy…….……65

4.3.2 SAED patterns……...65

4.4 Optical properties Characterization……..……70

4.4.1 Ultraviolet-Visible Spectroscopy……...70

4.5 Size distribution……...……...74

4.5.1 SAXS……74

4.6 Electrochemical characterization……77

4.6.1 Performance in three-electrode configuration……77

4.6.1.1 Cyclic Voltammetry……...77

4.6.1.2 Galvanostatic Charge-Discharge……...…81

4.6.1.3 Electrochemical Impedance Spectroscopy……85

4.7 References……..91

## CHAPTER 5

5. Conclusion and Recommendations……95

5.1 Conclusion……95

5.2 Recommendations……...97

Appendixes……98

# LIST OF FIGURES

**Figure 2.1:** SEM images for (A) Monoclinic phase (B) Hexagonal phase (C) Orthorhombic phase (D) Tetragonal phase……...20

**Figure 2.2:** Schematic diagram of (a) Cyclic Voltammetry (b) galvanostatic charge-discharge curves for a supercapacitor……...……22

**Figure 2.3:** Shows orthorhombic and imperfect scheelite structures of $Ln_2(WO_4)_3$, respectively……...……24

**Figure 2.4:** Shows cyclic voltammograms for (a)$Tb_2(WO_4)_3$ (b) $La_2(WO_4)_3$.....26

**Figure 2.5:** Comparative GCD study for (a) $Tb_2(WO_4)_3$ (b) $Sm_2(WO_4)_3$……...27

**Figure 4.1:** Overlaid FT-IR spectra of (A) $Gd_2(WO_4)_3$ and $Se_{0.61}Te_{0.39}$ (B) $Gd_2(WO_4)_3/Se_{0.61}Te_{0.39}$ nanocomposites at two different annealing temperatures……...56

**Figure 4.2:** Powder XRD pattern for (**A**) $Gd_2(WO_4)_3$ (**B**) $Se_{0.61}Te_{0.39}$ (**C**) overlaid patterns of $Gd_2(WO_4)_3$, $Se_{0.61}Te_{0.39}$, $Gd_2(WO_4)_3$/ $Se_{0.61}Te_{0.39}$ at 300 °C and 800 °C annealing temperatures……...……...57

**Figure 4.3:** SEM images with corresponding EDS spectrums for $Gd_2(WO_4)_3$, $Se_{0.61}Te_{0.39}$ and $Gd_2(WO_4)_3/Se_{0.61}Te_{0.39}$ respectively……61

**Figure 4.4:** TEM images of (A) $Gd_2(WO_4)_3$ (D) $Se_{0.61}Te_{0.39}$ (G) $Gd_2(WO_4)_3/Se_{0.61}Te_{0.39}$, HRTEM images of (B) $Gd_2(WO_4)_3$ (E) $Se_{0.61}Te_{0.39}$ (H) $Gd_2(WO_4)_3/Se_{0.61}Te_{0.39}$ and SAED pattern for (C) $Gd_2(WO_4)_3$ (F) $Se_{0.61}Te_{0.39}$ (I) $Gd_2(WO_4)_3/Se_{0.61}Te_{0.39}$……66

**Figure 4.5:** (A) Overlaid UV-vis spectra (B) Tauc plot for $Gd_2(WO_4)_3$ (C) Tauc plot for $Te_{0.39}Se_{0.61}$ (D) Tauc plot for $Gd_2(WO_4)_3/Te_{0.39}Se_{0.61}$.....71

**Figure 4.6:** SAXS plot of the particle size distribution for (A-C) $Gd_2(WO_4)_3$, (D-F) $Gd_2(WO_4)_3/Te_{0.39}Se_{0.61}$……...….75

**Figure 4.7:** Cyclic voltammograms for $Gd_2(WO_4)_3$, $Se_{0.61}Te_{0,39}$ and $Gd_2(WO_4)_3/Se_{0.61}Te_{0.39}$ in 2 M KOH at 10 $mVs^{-1}$…….....78

**Figure 4.8:** Multi-scan rates cyclic voltammograms of (A1) $Gd_2(WO_4)_3$ (A2) $Se_{0.61}Te_{0.39}$ (A3) $Gd_2(WO_4)_3/Se_{0.61}Te_{0.39}$ at scan rates 10 – 100 mV/S in 2 M KOH and (B1-B3) corresponding $I_{pa}$ proportion to the square root of scan rates……...79

**Figure 4.9:** (A) GCD curves at current density of 1.2 A $g^{-1}$ of $Gd_2(WO_4)_3$, $Te_{0.39}Se_{0.61}$, $Gd_2(WO_4)_3/Te_{0.39}Se_{0.61}$ (B) $Q_s$ vs current density plot of $Gd_2(WO_4)_3$, $Te_{0.39}Se_{0.61}$, $Gd_2(WO_4)_3/Te_{0.39}Se_{0.61}$…….83

**Figure 4.10:** Shows GCD curves at various current density for $Gd_2(WO_4)_3$, $Se_{0.61}Te_{0.39}$, $Gd_2(WO_4)_3/Se_{0.61}Te_{0.39}$…….85

**Figure 4.11:** Shows Nyquist plots and their equivalent circuits for synthesized nanoparticles…….87

# LIST OF TABLES

**Table 1:** Sample parameters with resulting phases and shape……..….20

**Table 2:** Rietveld refinement parameters and calculated crystal size values for the synthesized samples……...……...…...60

**Table 3:** Band gap energy values for the synthesized nanoparticles from Tauc plot……...…74

**Table 4:** Calculation of diffusion coefficient of the synthesized materials……...81

**Table 5:** Fitted equivalent circuit values for the synthesized nanoparticles……90

# ACRONYMS AND ABBREVIATIONS

| | |
|---|---|
| CNTs | Carbon Nanotubes |
| CV | Cyclic Voltammetry |
| EDLCs | Electrochemical Double Layer Capacitors |
| EDS | Energy Dispersive Spectroscopy |
| $E_g$ | Band gap energy |
| $E_p$ | Peak potential |
| $E_{pa}$ | Anodic peak potential |
| $E_{pc}$ | Cathodic peak potential |
| EIS | Electrochemical Impedance Spectroscopy |
| ESS | Energy Storage Systems |
| ESR | Equivalent Series Resistance |
| FTIR | Fourier Transform Infrared Spectroscopy |
| GCD | Galvanostatic Charge-Discharge |
| $Gd_2(WO_4)_3$ | Gadolinium tungsten oxide |
| $I_{pa}$ | Anodic peak current |
| $I_{pc}$ | Cathodic peak current |
| MTMOs | Mixed Transition Metal Oxides |
| NIR | Near Infrared |

| | |
|---|---|
| REE | Rare Earth Elements |
| SAED | Selected Area Electron Diffraction |
| SAXS | Small Angle X-ray Scattering |
| SEM | Scanning Electron Microscopy |
| SCs | Supercapacitors |
| $Te_ySe_x$ | Tellurium Selenide |
| TEM | Transmission Electron Microscopy |
| TMOs | Transition Metal Oxides |
| UV | Ultraviolet |
| UV-vis | Ultraviolet-Visible Spectroscopy |
| XRD | X-ray Diffraction |

# CHAPTER 1

## 1.0 INTRODUCTION

### 1.1 Background

Energy is closely related to all aspects of life, meaning both living and non-living organisms depend solely on the availability of energy. Human beings need energy to carry out their daily activities to support life. For example, we need electricity which is an energy carrier that provide us with light, heat, hot water and energy to power on our computers. The leading source of this electricity comes from fossil fuels (i.e. Coal, crude oil, natural gas, bitumen, uranium, thorium etc.) [1]. This however has a negative reflection on the natural reserves due to large scale use of non-renewable energy sources which led to their depletion. Another major setback is that when energy is produced in industries, various fossils are burned and gases such as carbon dioxide ($CO_2$), organosulphur compounds and nitrogen ($NO_X$) based compounds are released into the atmosphere [2, 3]. At an advanced stage, the presence of these by-products in the atmosphere may pose threats to human health, and may disrupt natural processes thereby causing acid rain and ozone depletion which results to global warming [4, 5]. This burning issue has left scientist with no choice but a quest for cleaner and reliable energy sources. Many research inputs have identified and proven that renewable energy sources present an alternative to traditional fossil-based fuels. Renewable energy is described as the energy that is derived from natural sources such as the wind, sun, rain and kinetics of flowing rivers [6]. The aforementioned sources are more advantageous than traditional fossil-based fuels for the following reason: Firstly, unlike non-renewable sources which are formed from animals and plants that were buried underneath the earth's surface from hundreds to billions of years ago,

energy can be captured and stored in any day when sunlight is shining onto the earth surface, wind is blowing in the atmosphere and from kinetics of flowing rivers. Secondly, nature provides these sources without any cost of going to depletion and lastly, they pose no threats to human health and the environment [7-11].

However, to fully rely on renewable energy sources, technological breakthrough in existing Energy Storage Systems (ESS) need to be developed. ESS are complex electronic devices that can convert electrical energy from power systems into a form that can be stored and converted back to electrical energy when needed. Therefore, in designing reliable storage systems, factors such as techno-economic performance, size, response time, lifetime, maintenance costs and environmental impacts need to be considered [12-15]. To date, various ESS that serve this purpose are available. These systems include fuel cells, batteries, capacitors and supercapacitors (SCs), each having unique properties [16]. Most research contributions have shown that SCs are the most promising storage devices with outstanding electrochemical performances due to their fascinating properties such as excellent capacitive properties, long lasting life cycling span, fast charge-discharge rate, high power density, superior reversibility, almost maintenance free, safety and reliability [17-20]. Supercapacitors are energy storage devices that have high capacitance and lower voltage limits than the normal capacitors that can store and release energy at a high rate compared to traditional batteries. SCs have two different types of operating mechanisms: Electrochemical Double Layer Capacitors (EDLCs) and pseudocapacitors [21]. EDLCs store energy by employing reversible ion adsorption on the surface of the electrode whereas pseudocapacitors store charge by means of fast reversible redox reactions at the electrode surfaces. But because both mechanisms used for EDLCs and pseudocapacitors have their own advantages and disadvantages, this has led to another third type of a mechanism which operates by combining the working principle of both EDLCs and

pseudocapacitors. This type of a mechanism can be categorised into three types of applicable electrode compartments: (i) asymmetric electrode hybrids- consists of two different electrodes, one occurring via faradic process and another via non-faradic process simultaneously. (ii) composite electrode hybrids- the physical and mechanical mechanisms are incorporated within one electrode. (iii) inorganic-organic hybrids- combines a battery type and supercapacitor type electrodes. The inorganic-organic hybrids (also called supercapatteries) are the latest development of ESS that offer enhanced electrochemical performance due to combined operating principles of EDLCs and pseudocapacitors [22, 23].

### 1.2 Problem Statement

Today the supply of energy is still centred around fossil-based fuels, and their consumption is proportional to the growing population and changing technologies. Meaning, with today's fast-paced population growth there's a higher demand for energy production which also requires a large-scale use of fossil fuels. As previously mentioned, the major problems that arises with fossil fuel usage is environmental pollution and depletion of these non-renewable resources. Even with clean and reliable energy sources found, today researchers are still left with a battle of finding suitable energy storage devices that can potentially store most of this energy for later use. A SC is highly beneficial for storing energy and its electrochemical performance is highly dependent on the electrode materials used. The main underlying problem with existing SCs is that the electrochemical performance of materials used as electrodes limits their application as storage devices. Transition metal oxides (TMOs) are most commonly used electrode materials for supercapacitors (particularly for pseudocapacitors) mainly because they have the large specific surface area, high chemical stability and excellent electrical conductivity. However, the major drawback for these materials is the wide band gap energy, poor electronic properties,

uncontrollable volume expansion and even though their energy density has shown an enhancement to a certain degree compared to EDLCs, they still suffer from low power density since the charge storage mechanism (via redox reactions) occurs at or near the surface of the electrode [24, 25].

### 1.3 Rationale or Motivation

Synthesis of bivalent mixed transition metal oxide (MTMO) doped with chalcogenides is the effective way to enhance the electronic properties of TMO as supercapacitor electrode materials. It is reported that, MTMO can facilitate diverse redox reactions due to coexistence of two different metals in one structure, the metal oxide in MTMO is responsible for generating more active sites and to enlarge the working potential window which can lead to enhanced specific capacitance compared to TMO [26-28]. However, since MTMO suffer from poor conductivity due to a wide bandgap energy, altering the structure of a parent MTMO by doping it with chalcogenide materials can lower the bandgap energy ($E_g$) of the material to achieve better conductivity. Tungsten oxide is one of the most investigated materials due to its multiple polymorphs (at least five). Many reports of tungsten oxide applications as electrode material for SCs are available but they only report a single phase $WO_3$ [29-32]. In this project, a parent material of tungsten oxide that incorporates a second metal from the lanthanide group to form lanthanide tungstate and a composite material of lanthanide tungstate doped with chalcogenide is proposed. Lanthanide ion are known for their unique optical and magnetic properties due to their f-electronic configurations and their tungstates have been found to offer properties such as excellent mechanical strength, high oxide ion conductivity, high thermal and chemical stabilities [33]. Tellurium is an interesting dopant that has attracted a huge attention due to its fast photoconductivity, high thermoelectricity, piezoelectricity and has $E_g$ that can be tuned

from approximately 0.35 to 1.0 eV. Therefore, when tellurium is incorporated into a structure of metal oxide, it would improve the bandgap of the metal oxide resulting to enhanced electrochemical performance [34].

## 1.4 Aims and Objectives

### 1.4.1 Aims

The main aim of this project is to synthesize and study electrochemical performance of the newly developed tellurium selenide-gadolinium tungsten oxide quantum dot material for supercapacitor.

### 1.4.2 Objectives

1. To synthesise a parent MTMO material (gadolinium tungsten oxide), a double chalcogenide material (tellurium selenide) and a nanocomposite material (tellurium selenide-gadolinium tungsten oxide) using one pot hydrothermal synthesis.
2. To investigate the crystal structure and size of the synthesized materials using X-ray diffraction spectroscopy (XRD), microscopic properties using High-Resolution Transmission Electron Microscope (HRTEM) and High-Resolution Scanning Electron Microscope (SEM), determination of the size using Small Angle X-ray Scattering (SAXS) and confirmation of elemental composition using Energy Dispersive X-ray Spectroscopy (EDS), determine the optical properties using Ultraviolet-visible Spectroscopy (UV-vis), determine the electrochemical behaviour using cyclic voltammetry (CV), galvanostatic charge-discharge (GCD) and Electrochemical Impedance Spectroscopy (EIS) in a three-electrode and two-electrode configuration.

## 1.5 Thesis outline

The thesis is structured into five chapters which are summarised as follows:

**Chapter One:** Presents a descriptive introduction, problem statement which has led to this study, motivation of the study, aims and objectives.

**Chapter Two:** presents a critical review of trivalent rare earth mixed-metal tungsten oxides electrode materials for supercapacitors, their synthetic routes, supercapacitive properties and applications.

**Chapter Three:** Presents materials and reagents, synthetic method routes and characterization. The theory behind the analytical techniques used are also described thoroughly.

**Chapter Four:** Discussion of results obtained from analytical techniques used for characterization and electrochemical performance tests.

**Chapter Five:** Summary of the conclusion and recommendation for future work.

## 1.6 References


[1] Bengt Sunden, "Chapter 1-Introduction and Backgorund," *Hydrog. Batter. Fuel Cells*, no. 1, pp. 1–23, 2019, doi: 10.1016/B978-0-12-816950-6.00001-4.

[2] Tomas Kåberger, "Progress of renewable electricity replacing fossil fuels," *Glob. Energy Interconnect.*, vol. 1, no. 1, pp. 48–52, 2018, doi: 10.14171/j.2096-5117.gei.2018.01.006.

[3] Simplice Asongu, Mary Oluwatoyin Agboola, Andrew Adewale Alola, and Festas Victor Bekun, "The criticality of growth, urbanization, electricity and fossil fuel consumption to environment sustainability in Africa," *Sci. Total Environ.*, vol. 712, p. 136376, 2020, doi: 10.1016/j.scitotenv.2019.136376.

[4] Mehmet Sefik Üney and Nurettin Çetinkaya , "Comparison of $CO_2$ emissions fossil fuel based energy generation plants and plants with Renewable Energy Source," *Proc. 2014 6th Int. Conf. Electron. Comput. Artif. Intell. ECAI 2014*, pp. 29–34, 2015, doi: 10.1109/ECAI.2014.7090175.

[5] Solomon Nathaniel, Ozoemena Nwodo, Abdulrauf Adediran, Gagan Sharma, Muhammad Shah, and Ngozi Adeleye, "Ecological footprint, urbanization, and energy consumption in South Africa: including the excluded," *Environ. Sci. Pollut. Res.*, vol. 26, no. 26, pp. 27168–27179, 2019, doi: 10.1007/s11356-019-05924-2.

[6] Abdul Olabi, "Renewable energy and energy storage systems," *Energy*, vol. 136, pp. 1–6, 2017, doi: 10.1016/j.energy.2017.07.054.

[7] Mukrimin Sevket Guney and Yalcin Tepe, "Classification and assessment of energy storage systems," *Renew. Sustain. Energy Rev.*, vol. 75, no. November 2016, pp. 1187–1197, 2017, doi: 10.1016/j.rser.2016.11.102.

[8] Tabbi Wilberforce, Mohamad Ramadan, Mohammad Ali Abdelkareem, and Abudul Hai Al – Alami, "Critical review of energy storage systems," *Energy*, vol. 214, p.

118987, 2021, doi: 10.1016/j.energy.2020.118987.

[9] Mohamad Ali Abdelkareem, Tabbi Wilberforce, and Enas Taha Sayed, "Application of graphene in energy storage device – A review," *Renew. Sustain. Energy Rev.*, vol. 135, no. June 2020, 2021, doi: 10.1016/j.rser.2020.110026.

[10] Tabbi Wilberforce, Zakki El Hassan, and Bassel. Soudan, "Overview of ocean power technology," *Energy*, vol. 175, pp. 165–181, 2019, doi: 10.1016/j.energy.2019.03.068.

[11] Tabbi Wilberforce, "Design of experiment (DOE) analysis of 5-cell stack fuel cell using three bipolar plate geometry designs," *Sustain.*, vol. 12, no. 11, 2020, doi: 10.3390/su12114488.

[12] Mohamed Becherif, Haitham Saad Ramadan, "Hydrogen Energy Storage: New Techno-Economic Emergence Solution Analysis," *Energy Procedia*, vol. 74, no. 0, pp. 371–380, 2015, doi: 10.1016/j.egypro.2015.07.629.

[13] Tugrul Daim, Xin Li, Jisun Kim, and Scott Simms, "Evaluation of energy storage technologies for integration with renewable electricity: Quantifying expert opinions," *Environ. Innov. Soc. Transitions*, vol. 3, pp. 29–49, 2012, doi: 10.1016/j.eist.2012.04.003.

[14] Syed Shabbar Raza, Isam Janajreh, and Chaouki Ghenai, "Sustainability index approach as a selection criteria for energy storage system of an intermittent renewable energy source," *Appl. Energy*, vol. 136, pp. 909–920, 2014, doi: 10.1016/j.apenergy.2014.04.080.

[15] Kelly Cowan, Tugrul Daim, and Tim Anderson, "Exploring the impact of technology development and adoption for sustainable hydroelectric power and storage technologies in the Pacific Northwest United States," *Energy*, vol. 35, no. 12, pp. 4771–4779, 2010, doi: 10.1016/j.energy.2010.09.013.

[16] Annette Evans, Vladimir Strezov, and Tim Evans, "Assessment of utility energy storage options for increased renewable energy penetration," *Renew. Sustain. Energy Rev.*, vol. 16, no. 6, pp. 4141–4147, 2012, doi: 10.1016/j.rser.2012.03.048.

[17] Chengxing Lu , Anran Li, Tengfei Zhai, and Chongrui Nui, "Interface design based on $Ti_3C_2$ MXene atomic layers of advanced battery-type material for supercapacitors," *Energy Storage Mater.*, vol. 26, no. June 2019, pp. 472–482, 2020, doi: 10.1016/j.ensm.2019.11.021.

[18] Chi Huey, Hong Ngee Lim, and Nai Ming Huang, "Cesium Lead Halide Inorganic-Based Perovskite-Sensitized Solar Cell for Photo-Supercapacitor Application under High Humidity Condition," *ACS Appl. Energy Mater.*, vol. 1, no. 2, pp. 692–699, 2018, doi: 10.1021/acsaem.7b00103.

[19] Pailin Ngaotrakanwiwat and Vissanu Meeyoo, "$TiO_2$-$V_2O_5$ nanocomposites as alternative energy storage substances for photocatalysts," *J. Nanosci. Nanotechnol.*, vol. 12, no. 1, pp. 828–833, 2012, doi: 10.1166/jnn.2012.5381.



[20] A. Manuscript, "Materials Chemistry A 6589," 2014.

[21] Hainan Wang and Laurent Pilon, "Accurate simulations of electric double layer capacitance of ultramicroelectrodes," *J. Phys. Chem. C*, vol. 115, no. 33, pp. 16711–16719, 2011, doi: 10.1021/jp204498e.

[22] Ahmed Afif, Sheik Rahman, Atia Tasfiah Azad, Juliana Zaini, Md Aminul Islan, and Abul Kalam Azad, "Advanced materials and technologies for hybrid supercapacitors for energy storage – A review," *J. Energy Storage*, vol. 25, no. July, p. 100852, 2019, doi: 10.1016/j.est.2019.100852.

[23] Zhang and Pan, "Supercapacitors performance evaluation," *Adv. Energy Mater.*, vol. 5, no. 6, pp. 1–19, 2015, doi: 10.1002/aenm.201401401.

[24] Yazhou Xu, Junchao Wei, Licheng Tan, Jin Yu, and Yiwan Chen, "A Facile approach to $NiCoO_2$ intimately standing on nitrogen doped graphene sheets by one-step hydrothermal synthesis for supercapacitors," *J. Mater. Chem. A*, vol. 3, no. 13, pp. 7121–7131, 2015, doi: 10.1039/c5ta00298b.

[25] Gongming Wang, Yi Yang, Dongdong Han, and Yat Li, "Oxygen defective metal oxides for energy conversion and storage," *Nano Today*, vol. 13, pp. 23–39, 2017, doi: 10.1016/j.nantod.2017.02.009.

[26] Yufei Zhang, Laiquan Li, Haiquan Su, Wei Huang, and Xiaochen Dong, "Binary metal oxide: Advanced energy storage materials in supercapacitors," *J. Mater. Chem. A*, vol. 3, no. 1, pp. 43–59, 2015, doi: 10.1039/c4ta04996a.

[27] Subbukalai Vijayakumar, Seong-Hun Lee, and Kwang-Sun Ryu, "Synthesis of $Zn_3V_2O_8$ nanoplatelets for lithium-ion battery and supercapacitor applications," *RSC Adv.*, vol. 5, no. 111, pp. 91822–91828, 2015, doi: 10.1039/c5ra13904j.

[28] Ejikeme Raphael Ezeigwe, Poi Sim Khiew, Chiu Wee Siong, and Michele Tan, "Solvothermal synthesis of $NiCo_2O_4$ nanocomposites on liquid-phase exfoliated graphene as an electrode material for electrochemical capacitors," *J. Alloys Compd.*, vol. 693, pp. 1133–1142, 2017, doi: 10.1016/j.jallcom.2016.09.244.

[29] Vaibhav Lokhande, Abhishek Lokhande, Gon Namkoong, Jin Hyeok Kim, and Taeksoo Ji, "Charge storage in $WO_3$ polymorphs and their application as supercapacitor electrode material," *Results Phys.*, vol. 12, no. February 2019, pp. 2012–2020, 2019, doi:

10.1016/j.rinp.2019.02.012.

[30] Songhun Yoon, Changshin Jo, Soon Young Noh, Chul Wee Lee, Jun Ho Song, and Jinwoo Lee, "Development of a high-performance anode for lithium ion batteries using novel ordered mesoporous tungsten oxide materials with high electrical conductivity," *Phys. Chem. Chem. Phys.*, vol. 13, no. 23, pp. 11060–11066, 2011, doi: 10.1039/c1cp20940j.

[31] Pragati Shinde, Abhishek Lokhande, Nilesh Chodankar, Amar Patil, Jin Kim, and Chandrakant Lokhande, "Temperature dependent surface morphological modifications of hexagonal $WO_3$ thin films for high performance supercapacitor application," *Electrochim. Acta*, vol. 224, pp. 397–404, 2017, doi: 10.1016/j.electacta.2016.12.066.

[32] Pragati Shinde, Vaibhav Lokhande, Nilesh Chodankar, Taeksoo Ji, Jin Kim, and Chandrakant Lokhande, "Enhanced electrochemical performance of monoclinic $WO_3$ thin film with redox additive aqueous electrolyte," *J. Colloid Interface Sci.*, vol. 483, pp. 261–267, 2016, doi: 10.1016/j.jcis.2016.08.011.



[33] Ali Sobhani-Nasab, "Sonochemical synthesis of terbium tungstate for developing high power supercapacitors with enhanced energy densities," *Ultrason. Sonochem.*, vol. 45, pp. 189–196, 2018, doi: 10.1016/j.ultsonch.2018.03.011.

[34] Weichun Huang, Ye Zhang, Xiuwen Zhang, and Han Zhang, "Enhanced Photodetection Properties of Tellurium@Selenium Roll-to-Roll Nanotube Heterojunctions," *Small*, vol. 15, no. 23, pp. 1–10, 2019, doi: 10.1002/smll.201900902.

# Chapter 2

## 2.0 Literature Review

## Inner transition metal ion-doped tungsten oxide electrode materials with scheelite structure for energy storage applications

---

### 2.1 Background

#### 2.1.1 Rare Earth Elements (REEs)

Rare earth elements are a group made up of seventeen elements of which in a periodic table, fifteen elements that are chemically similar are subdivided into a subgroup called lanthanides (from lanthanum (57) to lutecium (71)). The REEs are found in mines in an oxide state and usually occur as trivalent cations. These elements possess unique 4f-electron structures that are characterized by the presence of two subsystems: the *spd* states and the highly localized *f* states. Therefore, the chemical and physical properties of their oxides are critically dependent on the coupling between localized *f* and *spd* states. One of the most interesting features of rare earth ions is their ability to form various energy transition levels due to their partially filled 4f orbitals (from $4f^0$ (for $La^{3+}$) to $4f^{14}$ (for $Lu^{3+}$)), as a result, they can coordinate to form complexes with other elements that have coordination numbers ranging from 3 to 12. Because of such unique properties, REE materials have been widely employed in various applications for different purposes:

(i) Since REEs are commonly found in the form of mixture of oxides, they are used to produce high quality glasses as well as additives to ceramics due to their capability of not losing lustre when they are subjected or exposed to radiation.

(ii) Another important use of REEs is their application as phosphors to produce luminescent materials. Due to their abundant 4f orbitals structures, rare earth ions are used in the fluorescent materials in the lighting industry since they have strong fluorescence emissions that occurs via 4f-5d transitions which allows their excitation wave lengths to vary from the ultraviolet (UV) to near infrared (NIR) regions.

(iii) REEs have also been widely used in the metallurgy industry and in magnets. In metallurgy they are used as additive alloys for aluminium to increase their strength at high temperatures.

(iv) Because of their multivalent compounds, REEs have been known to possess pseudocapacitive behaviour which resulted in their use as electrode materials for supercapacitors.

By doping electrode materials, reports show that rare earth metals were able to improve electronic conductivity and enlarging the surface areas of the electrode materials.



Amongst other nanomaterials, metal tungstates have become one of the hot topics as electrode materials for energy storage systems. They constitute an important class of inorganic materials that have high potential to be applied as electrode materials for supercapacitors. This can be attributed to their various functional properties, which depend mainly on different arrangements of their structures. Generally, rare earth tungstates are known to exist in many different types, including structural form $AB(WO_4)_2$, $B_2W_3O_{12}$, $B_2(WO_4)_2$ etc. where A= alkali metal, B= lanthanide (trivalent metal). Among the types of rare earth tungstates mentioned, $B_2(WO_4)_3$ structure has been widely investigated due to trivalent cation conducting behaviour.

Even though REEs have been applied to various industries, their application as ESS is still uncommon. Therefore, this review discusses recent developments of REEs nanomaterials for

electrochemical energy storage applications (particularly, batteries and supercapacitors). Tungsten oxide is one of the most studied metal oxides due to its five polymorphs of which their crystal structures have a huge influence on their electrochemical performance. So firstly, in this study, a general presentation about synthetic methods for rare-earth ions-based tungsten oxides are presented which include sonochemical method, hydrothermal method, sol-gel method and solid-state method. Secondly, an in-depth supercapacitive properties of rare-earth ions-tungsten oxides and factors that affect their electrochemical performance are discussed. Because lanthanide elements possess chemical similarities, in some instances, only one or two elements will be used as examples to explain their chemical behaviour.

## 2.2 Synthetic Routes for lanthanum tungstates

### 2.2.1 Sonochemical method

Sonochemical method (also known as Ultra sound) is a powerful synthetic technique that is commonly used for synthesis of novel nanosized materials. This is one of the simplest inexpensive techniques that is based on the irradiation of liquid samples with ultrasonic waves resulting in a phenomenon called acoustic cavitation. During ultrasonic irradiation of liquid samples, bubbles generated within the oscillating system are collapsed by the acoustic field causing very high temperatures (> 5000 K) that are accompanied by high cooling rates (> $10^{10}$ K $s^{-1}$) are obtained. Under these distinct conditions, nanosized materials are successfully synthesized. Sonochemical approach offers a number of advantages over other traditional synthetic methods, for example, this method offers a green route synthesis for a wide range of nanomaterials due to decreased need of reducing agent, simple sample preparation, inexpensive, fast response, high possibility of coupling properties such as high surface area and crystallinity, generation of high intensity energy that can result in synthetic reaction at ambient

temperature and pressure, highly selective and sensitive determination of analyte at low concentrations [19-25]. Recently, synthesis of lanthanum tungstate ($La_2(WO_4)_3$) were separately reported by Sundaresan and Sobhani groups via sonochemical route. In their synthesis approach, lanthanum nitrates and sodium tungstate hydrates were used as precursors which were then dissolved in water and placed under ultrasonic irradiation [26, 27].

### 2.2.2 Hydrothermal method

Hydrothermal method is considered as the most widely used traditional method for synthesis of nanomaterials. This method is a solution reaction-based approach used to carry out simple and complex reactions at high temperatures and pressure. Multiple research investigations based on rare earth compounds via traditional hydrothermal method have been reported. For example, rare earth tungstates ($Gd_2(WO_4)_3$), rare earth orthochromites $LaCrO_3$, rare earth nanotubes ($Yb(OH)_3$, $Tm(OH)_3$, $Sm(OH)_3$), doped metal oxides (e.g. $Y_2O_3$-doped $ZrO_2$) have been carried successfully via hydrothermal synthesis [26-31]. This method offers several advantages such as ability to control the morphology, size, composition of nanomaterial, nanoparticles have well defined crystallinity and crystal phases. One of the most critical parameters that play an important role during hydrothermal synthesis are: the temperature of the stainless-steel lined autoclave, duration of the reaction (usually ranges from 2hr to days) and the pH of the aqueous solution [32-36]. In a typical hydrothermal process, usually two soluble powders (e.g. tungstates, nitrates and chlorides) are completely dissolved in water in separate beakers, then mixed together under magnetic stirring. Then the pH is either adjusted by an acid or base, depending on whether a precipitate forms at lower or higher pH values (for example, HCl is added to the mixture for $pH < 7$ and NaOH or $NH_4OH$ for $pH > 7$). The mixture is then stirred for a couple of minutes before being transferred into a stainless-steel autoclave

where it is subjected and maintained at high temperatures (usually 150-350 ° C) for some time depending on the experiment conditions. Then, the reaction mixture is allowed to cool down naturally to room temperature, where the product formed (precipitate) is collected, washed, dried, calcined and weighed. Shruthi and his group reported a successful synthesis of $Gd_2(WO_4)_3$ phosphor with a monoclinic crystal structure via a hydrothermal method [31]. Even though this method has been successfully used for synthesis of nanoparticles, its disadvantages are associated with difficulties in controlling its processes since its subjected at high temperatures. Secondly, this method suffers from limitation of reliability and reproducibility. When the reaction mixture has reached high temperature and pressure, solute molecules are excited and begin to move with high speeds where they collide to form larger particles in the solution (process called nucleation). After some time when the reaction is switched off and the reaction mixture allowed to cool down naturally, precipitation takes place and crystals are formed [37].



### 2.2.3 Solid-state method

A solid-state method is a simplest technique yet with difficult parameters to control. It involves grinding and heating. In most cases, it is used for syntheses that cannot be achieved via chemical and other synthetic routes. This method has been successfully used for synthesis of single crystals and polycrystalline powders of transition metals [38, 39]. In a typical solid-state method, precursor powders are first separately grinded in a pestle and mortar, then placed on separate crucibles where they are subjected in an oven to be preheated at high temperature between 350 and 450 °C to remove volatile impurities such as water molecules ($H_2O$), carbon dioxide ($CO_2$) and nitrates ($NO_x$). Then the two preheated precursor powders are mixed in one mortar and homogenously grinded as fine as possible to achieve small grain size particles, and

heated again at high temperatures close to 1000 °C or beyond depending on the experimental conditions. After heating the mixture, the oven is switched off and allowed to cool down back to room temperature where the product is then grinded and weighed [40-42]. Since this method is used in the absence of solvents, it offers products without impurities and due to grinding, a decrease in grain size and increase to specific surface area are achieved. The disadvantage of this method is that its time consuming because of the slow ramping rate and high temperatures used might decompose the product. The key aspects of this method which need extra attention are: the heating rate, temperature of the reaction, the cooling rate and grinding. The heating rate and temperature are very crucial parameters because fast heating rate damages the product including high temperatures, hence one needs to investigate properly the melting point properties of precursor powders.

Lopatin group reported a successful synthesis of $La_2(WO_4)_3$ via solid-state state method [43]. As an example, they prepared $Gd_2(WO_4)_3$ from precursors $Gd_2O_3$ and $WO_3$ which were annealed from 600 °C to 1100 °C. The synthesis was carried according to the following equation:



$$Gd_2O_3 + 3WO_2 \rightarrow Gd_2(WO_4)_3 \quad (1)$$

### 2.2.4 Electrospinning method

Electrospinning technique is a simple synthetic route that is used for generating fine fibres of materials. The basis of this method is driven by voltage where fibres are made from polymer solution. For this technique to be carried out through with success, three major components are needed: high voltage supplier, syringe with a metal needle and a conductive collector. During this process, voltage is applied between the needle and the conductive collector plate, and the surface charge builds up on the surface of the solution leading to high repulsive force that is

able to overcome the surface tension and viscosity of the polymer solution which therefore results in a stream of fluid coming through the needle to form fibres on the collector plate [44]. This technique is associated with many advantages such as a simple procedure, inexpensive setup and offers an ability to control the composition of the material including the desired diameter of the nanofibers. Because this method involves use of organic solvents, the disadvantage that is associated with is environmental pollution. There's quite a number of publication available which reported a successful synthesis of lanthanum tungstates nanoparticles. For example, Yanee Keereeta and group reported synthesis of lanthanum tungstate interconnecting by high voltage electrospinning [44].

## 2.3 Formulation of lanthanum tungstates

### 2.3.1 Tungsten oxide

Tungsten oxide ($WO_3$) is another type of metal oxide which is commonly investigated and applied in energy storage system applications due to its high conductivity nature, desirable crystal structure, small radius, and is known to possess pseudocapacitive behaviour [45-50]. This metal oxide has five polymorphs with different crystalline structures which have huge influence on the electrochemical performance of its electrodes materials when applied in energy systems [51]. Various methods have been successfully employed for synthesis of $WO_3$ materials and these methods include but not limited to the synthetic routes mentioned above. Among the types of synthetic methods mentioned, hydrothermal approach is the most suitable method since the morphology and phases of $WO_3$ can be controlled through managing parameters such as the pH of the solution mixture, hydrothermal temperature of the autoclave and the time of the reaction mixture. Many research publications are available that report on the application of tungsten oxide as electrode material for supercapacitors. Vaibhav and group

reported charge storage in $WO_3$ polymorphs and their applications as supercapacitor electrode materials.

In a typical hydrothermal method, the formation of $WO_3$ can be explained by the following equations:

$$Na_2WO_4 \rightarrow 2Na^+ + WO_4^{2-} \quad (2)$$

$$WO_4^{2-} + 2H^+ \rightarrow H_2WO_4 \quad (3)$$

$$H_2WO_4 \rightarrow WO_3 + H_2O \quad (4)$$

In the first step, sodium tungstate is dissolved in water to form $Na^+$ and $WO_4^{2-}$ ions. Then tungstate ions are protonated in step two when the pH of the mixture is driven to high acidic mixture with an acid solution (usually with 6 M HCl) to form a milky tungstic precipitate [52]. The last step involves removal of water molecules from the tungstic particles, where tungsten-oxygen bonds (W-O) reform and oxygen atoms interconnect to form a stable desired structure [53]. The summary of the parameters for reported structures are included in Table 1. As it can be seen from the table below, the key parameters for designing the desired phases depend solely on the pH of the solution mixture and the temperature of the autoclave. At high acidic conditions the rate of particle formation is also high. The higher acidic a system is, the smaller the particle size and vice versa. The resulting smaller particle size is another important factor that is very crucial for the performance of a material. Small particles are known to have high surface reactivity as compared to their bulk materials and because of that, their oxidation-reduction reactions occurring at or near the surface of the electrode material have been reported to have superior electrochemical performance. Figure 2.1 shows SEM images for different phases taken at 150 kX magnification of $WO_3$ morphologies reported according to Table 1.

**Table1:** Sample parameters with resulting phases and shape.

| pH | Autoclave Temp. (°C) | Phase | Shape | Ref |
|---|---|---|---|---|
| 0.5-1 | 180 | Monoclinic | Cube | [46] |
| 3 | 160 | Hexagonal | Cube | [54] |
| 2 | 180 | Orthorhombic | Rods | [52] |
| 1 | 200 | Tetragonal | Cubic Plate | [53] |

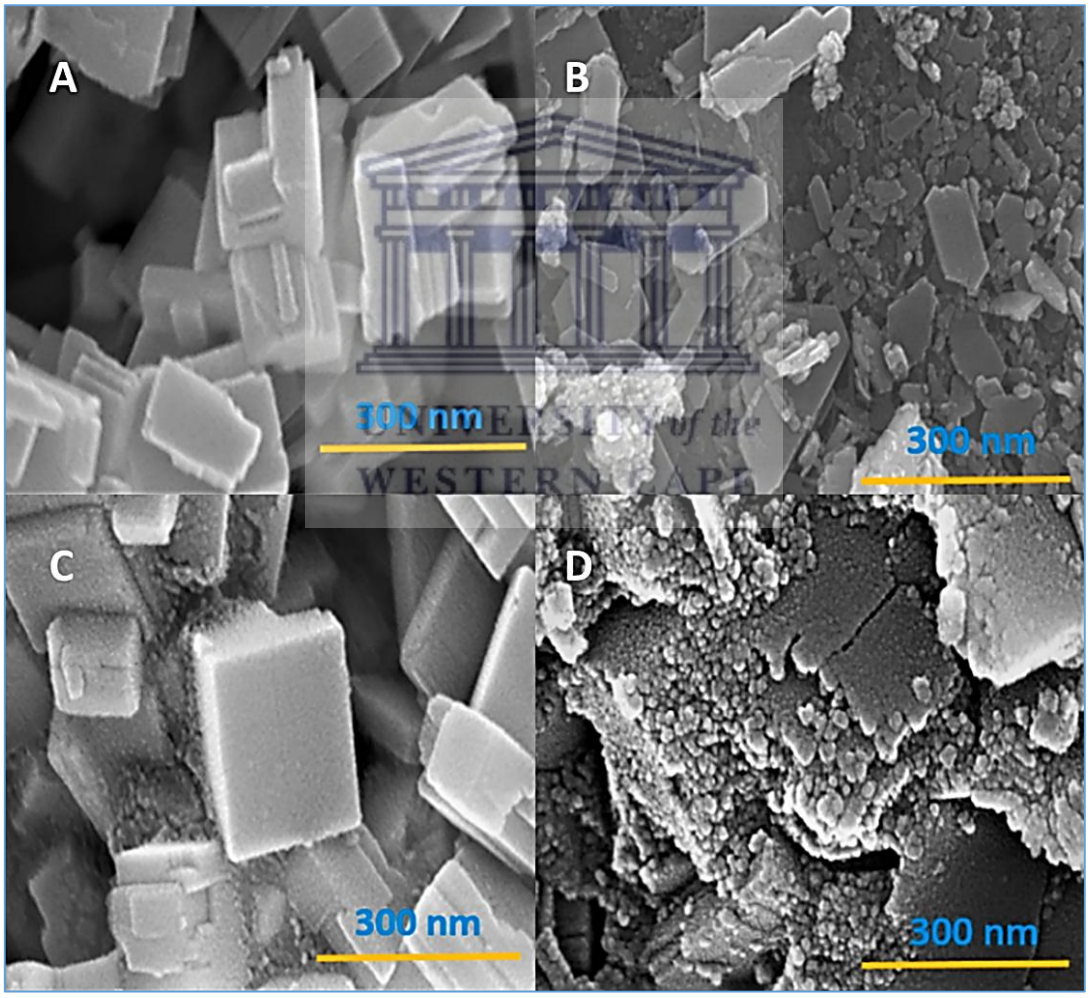


**Figure 2.1:** SEM images for (A) Monoclinic phase (B) Hexagonal phase (C) Orthorhombic phase (D) Tetragonal phase. Reprinted with permission [53]. Copyright 2019, Elsevier.

For comparative studies to determine the best suitable phase candidate as an electrode material for supercapacitive application, the electrochemical performance of the tungsten oxide phases was examined using cyclic voltammetry, galvanostatic charge-discharge and electrochemical impedance techniques in a three electrode system. Before diving directly into the electrochemical characterization of $WO_3$ phase, it is best to first touch on the interpretation of the aforementioned techniques because of the available misinterpretation of the data. A double layer forms when two opposite polarities co-exist between the electrode and electrolyte interface. Therefore, the charge stored by a supercapacitor varies linearly with the applied voltage and a typical response from a charge-discharge processes will have a linear relationship between voltage versus time curve, and a rectangular shape for cyclic voltammograms (Figure 2.2). Then the charge storage can then be reported as capacitance using equation 5 in farads not capacity (which follows a non-linear relationship with the applied potential), which is one common mistake made by researchers [55-57].

$$C = Q/V = \int (it/v) \quad (5)$$



where C is the capacitance (F), Q is the charge (C), V is the voltage (V), i is the electric current (A), t is the time (s) and $v$ is the scan rate (V $s^{-1}$).

Another common misinterpretation comes from interpretation of electrochemical impedance data. There are two general ways of reporting the impedance data: firstly, by a Nyquist plot which is presented with an imaginary impedance against real impedance at different frequencies. Secondly, by Bode plots which is represented by a phase angle and the modulus (Z) as a function of frequency. A typical Nyquist plot representation for consists of high (left, real Z) and low frequency regions (right, real Z). A characteristic of a supercapacitor Nyquist

plot will show a 45 ° line starting from the equivalent resistance (ESR) followed by 90°- line (vertical line) that extends straight to low frequencies.

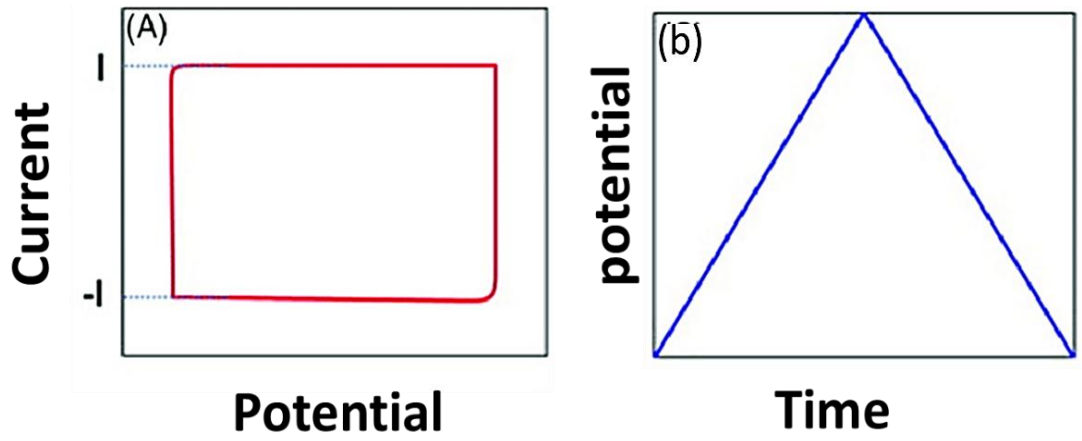


**Figure 2.2:** Schematic diagram of (a) cyclic voltammetry (b) galvanostatic charge-discharge curves for a supercapacitor.

Supercapacitors should never show a semi-circle at high frequency regions since they store charge in a physical manner. Many research publications incorrectly report the presence of a semicircle at high frequency regions for supercapacitors and explain that this is attributed to charge transfer resistance [58-64]. Diard explained that the reason for observing semicircles is because of the artificial impedance occurring at the active material interface [55]. Furthermore, battery type electrodes are characterised by diffusion-controlled processes which is normally caused by scan rate dependence. On the other hand, supercapacitors have charge storage mechanism that is independent of scan rates (non-diffusion controlled processes) at the surface of the electrodes. Literature results showed a larger specific capacitance of 377.5 F $g^{-1}$ for a hexagonal phase followed by tetragonal phase which demonstrated 368 F $g^{-1}$. The electrochemical impedance studies performed showed a semicircle in the high frequency region followed by a tail (Warburg diffusion resistance) which indicated the dependence of the active

material to the scanning rate. hexagonal showed a small charge resistance transfer of 1.59 $\boldsymbol{\Omega}$ which indicated that this phase has fast kinetics and charge transfer compared to other phases.

The study of different tungsten oxide phases for their electrochemical performance determination as electrode materials for supercapacitors reveal that these phases exhibit diffusion-controlled processes which makes them more useful for battery type electrodes [53]. So in a quest to optimize the electrochemical performance of these phases, incorporating lanthanum metals ($Ln^{3+}$) was proposed since they can form a wide range of coordination complexes with an ease of electron mobility and enhanced material conductivity.

### 2.3.2 Lanthanum doped tungsten oxide

Lanthanum ($Ln^{3+}$) doped tungstates have been widely investigated due to their electronic properties but very few publications have been reported on the highlights of their electrochemical performance-based electrode for ESS [65-68]. Therefore, this section focuses on factors that play important role on the performance of lanthanum tungstate materials as potential candidates for supercapacitive application. Since the performance of electrode material is mostly dependent on the mobility of electrons, our discussion will be focused on understanding the ion conduction and supercapacitive application of lanthanum doped tungsten oxide compounds with scheelite structure ($Ln_2(WO_4)_3$). Generally, there are two types of crystalline structure formation reported for $Ln_2(WO_4)_3$, the orthorhombic and the imperfect scheelite structure (monoclinic). The difference between the two structures lies with the number of bonded oxygen atoms: the orthorhombic structure is characterized by the presence of $WO_4^{2-}$ tetrahedrons of which in this structure, the tetrahedron units are formed when hexavalent tungsten ion ($W^{6+}$) attaches to four oxide anions. This structure is known to have reduced electrostatic interaction between $Ln^{3+}$ and oxygen anion ($O^{2-}$) of which this results in

$Ln^{3+}$ ion diffusing in the structure. In the imperfect scheelite structure the hexavalent tungsten oxide ($W^{6+}$) is surrounded by eight oxygen anions ($O^{2-}$) unlike the orthorhombic structure which is surrounded by six. The migration of $Ln^{3+}$ cation is hindered by the strong electrostatic interaction between $Ln^{3+}$ and $O^{2-}$ anions in the imperfect scheelite structure.

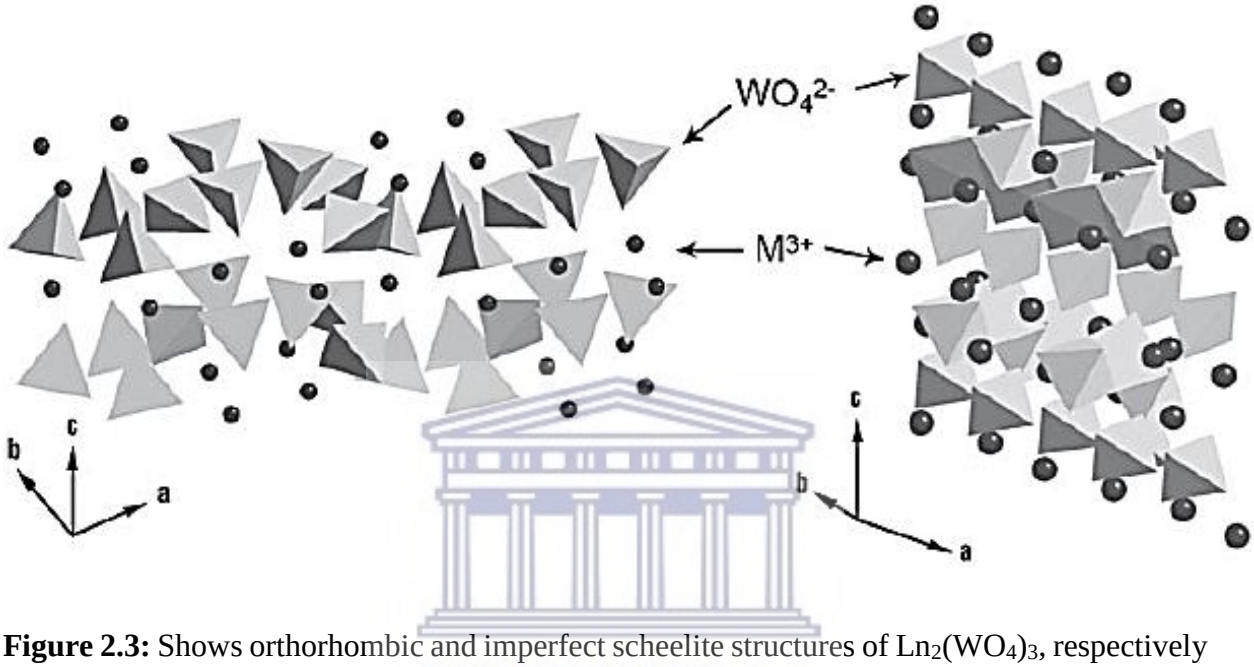


**Figure 2.3:** Shows orthorhombic and imperfect scheelite structures of $Ln_2(WO_4)_3$, respectively [66].



To understand the nature of mobile carriers in $Ln_2(WO_4)_3$, Lopatin carried Tubandt experiments in two section cells at a temperature of 850 °C [43]. According to this method, the change in mass of the two sections (cathode and anode sections) are recorded. Taking one lanthanum metal for demonstration, the following reaction may occur in the cathode and anode sections:

$$(-)\ 3Ho_2(WO_4)_3 + 4O_2 + 16e^- = HoWO_{12} + 8WO_4^{2-} \quad (6)$$

$$(+)\ WO_4^{2-} = WO_3 + \tfrac{1}{2}O_2 + 2e^- \quad (7)$$

and then the transfer of ions was calculated according to the following formula:

$$t(WO_4^{2-}) = (\Delta m^{(-)}/M_{WO3})*Z_{WO4^{2-}}*(F/Q) \quad (8)$$

where $\Delta m^{(-)}$ corresponds to $WO_3$ mass equivalent to $[WO_4]^{2-}$ ions migration, $M_{WO3}$ is the molar mass of $WO_3$ in g $mol^{-1}$, Z = 2, Q is the amount of electricity that passes through the system and F is the faraday's constant.

Based on the method, $[WO_4]^{2-}$ ions had no significant contribution towards charge transfer and therefore, oxygen were the mobile species in $Ln_2(WO_4)_3$. This can be attributed to the fact that structural vacancies open channels for oxygen ions migration which in turn increases chances of oxygen conductivity [43,69,70].

#### 2.3.2.1 Lanthanum doped tungsten oxide-based supercapacitors application

Prior to characterizing the electrochemical performance of the synthesized $Ln_2(WO_4)_3$ particles, three-electrode setups were prepared in such a way that the mixtures of active material; carbon black; PVDP binder were mixed by the following ratio 7:2:1, respectively (Note: the ratios of the mentioned ingredients may differ from researcher to researcher according to what is desired). This section will only be limited to the evaluation of electrochemical studies of $Ln_2(WO_4)_3$ and in any case, one metal will be chosen as an example since lanthanum metals show common/similar characteristics. So the only techniques that will be discussed is CV, GCD and EIS. Figure 2.9 shows a cyclic voltammograms for $Tb_2(WO_4)_3$ and $La_2(WO_4)_3$. One notable characteristic from the CV profile is the dependence of the current with the scan rate. The specific capacitance of $Ln_2(WO_4)_3$ were calculated using equation 9.

$$SC = i/mv = \int i(v)\, dV/mv\Delta V \quad (9)$$

where i is the electric current (A), m is the mass of electrode material (g), *v* is the scan rate (V $s^{-1}$), dV shows voltage differential, ΔV is the difference between the initial and final voltages (V).

The literature values of the calculated specific capacitance for $Tb_2(WO_4)_3$ and $Sm_2(WO_4)_3$ based on equation (9), showed a decreasing trend with the increasing scan rate (from 336 to 205 F $g^{-1}$), a characteristic usually seen for pseudocapactive electrodes. It is also notable in Figure 2.4 (a) that $Tb_2(WO_4)_3$ has a quasi-rectangular shape, while Figure 2.4 (b) is completely reversible for $Sm_2(WO_4)_3$. From the cyclic voltammograms, it is clear that the $Ln_2(WO_4)$ material do exhibit a supercapacitive behaviour but basing finding only on one technique is forbidden.

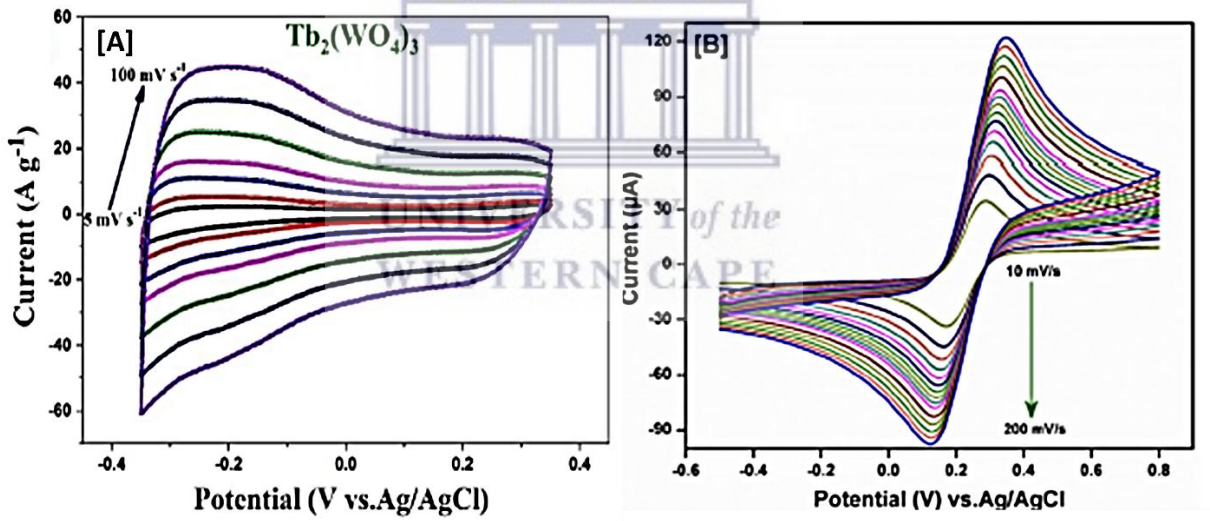


**Figure 2.4:** Shows cyclic voltammograms for (a)$Tb_2(WO_4)_3$ (b) $La_2(WO_4)_3$. Reprinted with permission [26]. Copyrights 2017, Springer.

Furthermore, the galvanostatic charge/discharge technique employed to study the behaviour of $Tb_2(WO_4)_3$ and $Sm_2(WO_4)_3$ under the same conditions can be found below in Figure 2.5.

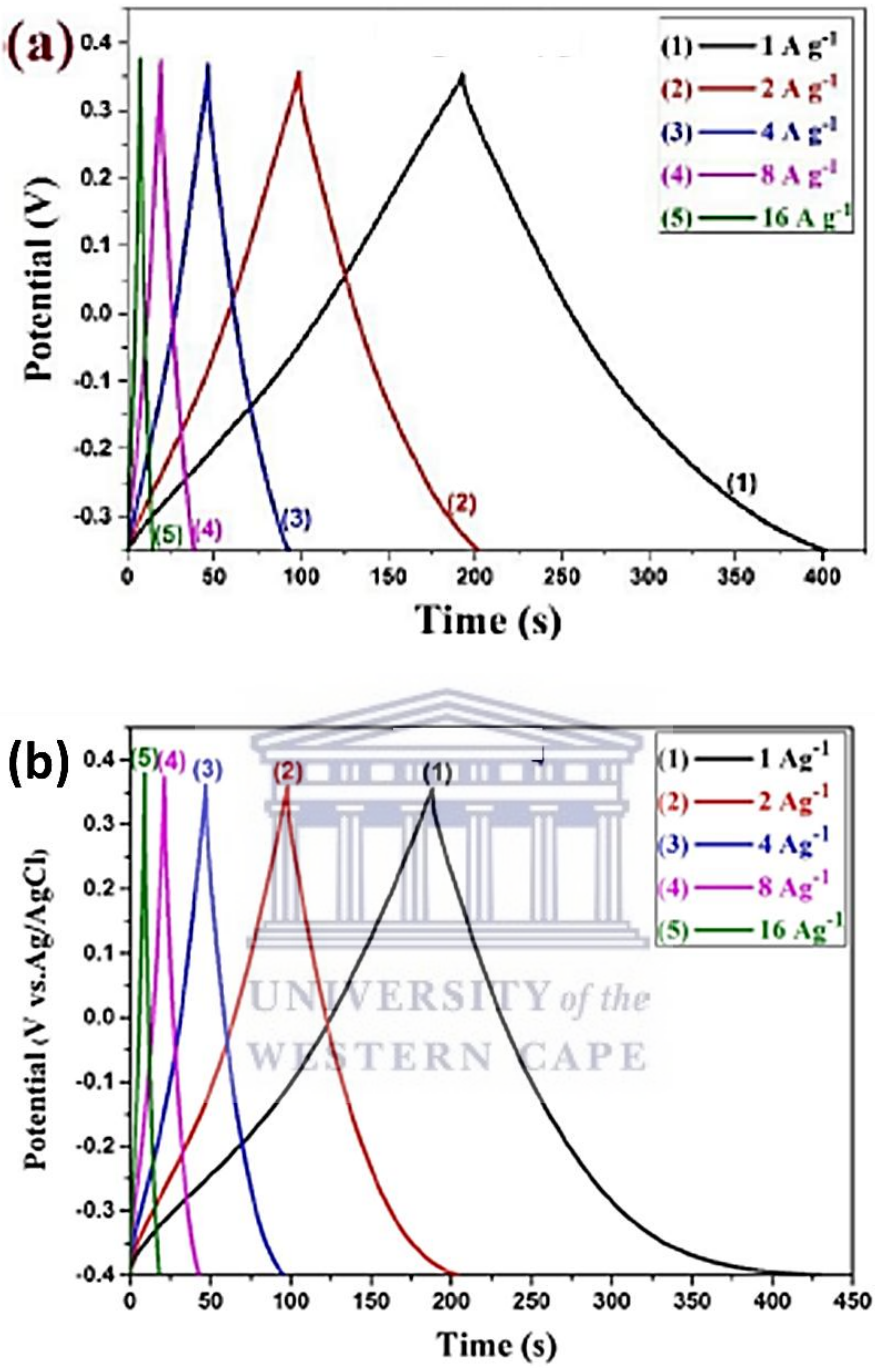


**Figure 2.5:** Comparative GCD study for (a) $Tb_2(WO_4)_3$ (b) $Sm_2(WO_4)_3$. Reprinted with permission. Copyrights 2017, Springer Nature.

The tests were carried in a three electrode system at current densities of 1-16 A $g^{-1}$. Both lanthanum tungstates behaved in a similar manner showing a symmetric triangular shape

during charging/discharging processes. This is a characteristic of an ideal pseudocapacitor of which this is in good agreement with what has been observed in cyclic voltammetry characterization. $Sm_2(WO_4)_3$ showed a superior energy density of 30.8 W h $Kg^{-1}$ compared to $Tb_2(WO_4)_3$ which showed 20.4 W h $Kg^{-1}$. This studies both show that Lanthanum tungsten oxides electrode materials can actually be applied as electrodes for supercapacitors. Also studies of electrochemical impedance which showed a semicircle at high frequencies followed by a Warburg resistance were in good agreement with the data from CV and GCD characterization.

**2.4 Conclusion**

There are many different methods that can be used to prepare lanthanum tungsten oxides but sonochemical method presents the best, easy and cheap approach. There are four phases reported for tungsten oxides of which hexagonal and tetragonal phases showed superior electrochemical performance when compared to others. Among doping tungsten oxide with lanthanum metals, only two crystalline structures $Ln_2(WO_4)_3$ can form, the orthorhombic and imperfect scheelite structure. Even through electrochemical studies to evaluate the behaviour of the tungstates oxides phases ($WO_3$) had a battery-type like performance, after doping with lanthanum metals, pseudocapacitors behaviour was observed. Meaning Lanthanum metals ($M^{3+}$) had an effect of pushing the behaviour of the $Ln_2(WO_4)_3$ electrodes towards pseudocapacitive characteristics. With the performance reported, $Ln_2(WO_4)_3$ materials do actually qualify as candidates for supercapacitors but a lot of work still needs to be done. One possible way of optimizing the electrochemical performance of $Ln_2(WO_4)_3$ is by doping with chalcogenides. Chalcogenides have demonstrated proven records of a wider energy band gap that can be tuned from approximately 0.35 to 1.0 eV. Therefore, when incorporated into a

structure of metal oxide, it will improve the bandgap of the metal oxide thereby enhancing the electrochemical performance.

## 2.5 Reference


[1] Georgianna Moldoveanu and Vladimiros Papangelakis, "Recovery of rare earth elements adsorbed on clay minerals: I. Desorption mechanism," *Hydrometallurgy*, vol. 117–118, pp. 71–78, 2012, doi: 10.1016/j.hydromet.2012.02.007.

[2] Naumov, "Review of the world market of rare-earth metals," *Russ. J. Non-Ferrous Met.*, vol. 49, no. 1, pp. 14–22, 2008, doi: 10.3103/S1067821208010045.

[3] Stefania Massari and Marcello Ruberti, "Rare earth elements as critical raw materials: Focus on international markets and future strategies," *Resour. Policy*, vol. 38, no. 1, pp. 36–43, 2013, doi: 10.1016/j.resourpol.2012.07.001.

[4] Nobuhito Imanaka, Yasuhuki Kobayashi, Kazuyasu Fujiwara, Takuya Asano, Yusuka Okazaki, and Gin-ya Adachi, "Trivalent Rare Earth Ion Conduction in the Rare Earth Tungstates with the $Sc_2(WO_4)_3$-Type Structure," *Chem. Mater.*, vol. 10, no. 7, pp. 2006–2012, 1998, doi: 10.1021/cm980157e.

[5] Anita Hastir, Nipin Kohli, and Ravi Chad Singh, "Comparative study on gas sensing properties of rare earth ( Tb , Dy and Er ) doped ZnO sensor," *J. Phys. Chem. Solids*, vol. 105, no. February, pp. 23–34, 2017, doi: 10.1016/j.jpcs.2017.02.004.

[6] Changli Wang, "Nano rare-earth oxides induced size-dependent vacuolization : an independent pathway from autophagy," pp. 601–609, 2010, doi: 10.2147/IJN.S11513.

[7] Hong Jiang, Patrick Rinke, and Mattias Scheffler, "Electronic properties of lanthanide oxides from the GW perspective," vol. 125115, pp. 1–13, 2012, doi: 10.1103/PhysRevB.86.125115.

[8] Shili Gai, Chunxia Li, Piapong Yang, and Jun Lin, "Recent Progress in Rare Earth Micro

/ Nanocrystals : Soft Chemical Synthesis , Luminescent Properties , and Biomedical Applications," 2014.

[9] Mikaela Nichkova, Dosi Dosev, Shirly Gee, Bruce Hammock, and Ian Kennedy, "Microarray Immunoassay for Phenoxybenzoic Acid Using Polymer Encapsulated Eu : $Gd_2O_3$ Nanoparticles as Fluorescent Labels," vol. 77, no. 21, pp. 6864–6873, 2005.

[10] Sam Niedbala, Hans Feindt, Keith Kardos, Timotty Vail, Jareth Burton, Barbara Bielska, Shang Lee, and David Milunic, "Detection of Analytes by Immunoassay Using Up-Converting Phosphor Technology," vol. 30, pp. 22–30, 2001, doi: 10.1006/abio.2001.5105.

[11] Patrick Judeinstein and Clement Sanchez, "Hybrid organic-inorganic materials : a land of multidisciplinarity Chemistry : Synthesis of Hybrid Materials," vol. 6, no. 4, pp. 511–525, 1996.

[12] Røyset and Ryum, "Scandium in aluminium alloys," *Int. Mater. Rev.*, vol. 50, no. 1, pp. 19–44, 2005, doi: 10.1179/174328005X14311.

[13] Zhang Wang , "Simultaneous phase and size control of upconversion nanocrystals through lanthanide doping," *Nature*, vol. 463, no. 7284, pp. 1061–1065, 2010, doi: 10.1038/nature08777.

[14] Bo Zhou, Bingyang Shi, Dayong Jin, and Xiaogang Liu, "Controlling upconversion nanocrystals for emerging applications," *Nat. Nanotechnol.*, vol. 10, no. 11, pp. 924–936, 2015, doi: 10.1038/nnano.2015.251.

[15] Xiaofei Shi, Zhihao Wang, Toshiaki Takei, Qi Zhu, and Ji-Guang Li, "Selective Crystallization of Four Tungstates ($La_2W_3O_{12}$, $La_2W_2O_9$, $La_{14}W_8O_{45}$, and $La_6W_2O_{15}$)

via Hydrothermal Reaction and Comparative Study of $Eu^{3+}$ Luminescence," *Inorg. Chem.*, vol. 57, no. 11, pp. 6632–6640, 2018, doi: 10.1021/acs.inorgchem.8b00807.

[16] Nobihito Imanaka and Shinji Tamura, "Development of multivalent ion conducting solid electrolytes," *Bull. Chem. Soc. Jpn.*, vol. 84, no. 4, pp. 353–362, 2011, doi: 10.1246/bcsj.20100178.

[17] Ruhollah Talebi, "Simple sonochemical synthesis and characterization of nickel tungstate nanoparticles and its photocatalyst application," *J. Mater. Sci. Mater. Electron.*, vol. 27, no. 4, pp. 3565–3569, 2016, doi: 10.1007/s10854-015-4192-8.

[18] Xu Hangxun, Brad Zeiger, and Kenneth Suslick, "Sonochemical synthesis of nanomaterials," *Chem. Soc. Rev.*, vol. 42, no. 7, pp. 2555–2567, 2013, doi: 10.1039/c2cs35282f.

[19] Vera Granado, Manuel Gutiérrez-Capitán, Cesar Fernández-Sánchez, Teresa Gomes, Alisa Rudnitskaya, and Cecilia Jimenez-Jorquera, "Thin-film electrochemical sensor for diphenylamine detection using molecularly imprinted polymers," *Anal. Chim. Acta*, vol. 809, pp. 141–147, 2014, doi: 10.1016/j.aca.2013.11.038.

[20] Mohammadreza Kamali, Maria Costa, Gonzalo Otero-Irurueta, and Isabel Capela, "Ultrasonic irradiation as a green production route for coupling crystallinity and high specific surface area in iron nanomaterials," *J. Clean. Prod.*, vol. 211, pp. 185–197, 2019, doi: 10.1016/j.jclepro.2018.11.127.

[21] Rüllmann., "Compact and Foamed Magnetorheological Polyurethanes," no. 3, pp. 2–3, 2006.

[22] Andrew Cádiz Bedini, Benjamin Klingebiel, Martina Luysberg, and Reinhard Carius,

"Sonochemical synthesis of hydrogenated amorphous silicon nanoparticles from liquid trisilane at ambient temperature and pressure," *Ultrason. Sonochem.*, vol. 39, no. May, pp. 883–888, 2017, doi: 10.1016/j.ultsonch.2017.06.011.

[23] Shirin Shaker-Agjekandy and Aziz Habibi-Yangjeh, "Ultrasonic-assisted preparation of novel ternary ZnO/AgI/$Ag_2CrO_4$ nanocomposites as visible-light-driven photocatalysts with excellent activity," *Mater. Sci. Semicond. Process.*, vol. 44, pp. 48–56, 2016, doi: 10.1016/j.mssp.2015.12.025.

[24] Sara Naghizadeh-Alamdari and Aziz Habibi-Yangjeh, "Sonochemical preparation of AgBr-ZnO nanocomposites in water using one-pot method as highly efficient photocatalysts under visible light," *J. Iran. Chem. Soc.*, vol. 12, no. 11, pp. 1961–1971, 2015, doi: 10.1007/s13738-015-0670-4.

[25] Hadi Nouri and Aziz Habibi-Yangjeh, "Sonochemical green method for preparation of Mg-doped ZnO nanostructures in water with enhanced photocatalytic activity," *Phys. Chem. Res.*, vol. 3, no. 2, pp. 99–110, 2015, doi: 10.22036/pcr.2015.7800.

[26] Periyasamy Sundaresan, Periyasami Gnanaprakasam, Shen-Ming Chen, Ramalinga Vitswanathan Mangalaraja, Wu Lei, and Qingli Hao, "Simple sonochemical synthesis of lanthanum tungstate ($La_2(WO_4)_3$) nanoparticles as an enhanced electrocatalyst for the selective electrochemical determination of anti-scald-inhibitor diphenylamine," *Ultrason. Sonochem.*, vol. 58, no. June, p. 104647, 2019, doi: 10.1016/j.ultsonch.2019.104647.

[27] Ali Sobhani-Nasab, Hamid Naderi, Mehdi Rahimi-Nasrabadi, and Mohammad Reza Ganjali, "Evaluation of supercapacitive behavior of samarium tungstate nanoparticles synthesized via sonochemical method," *J. Mater. Sci. Mater. Electron.*, vol. 28, no. 12,

pp. 8588–8595, 2017, doi: 10.1007/s10854-017-6582-6.

[28] Kripasindhu Sardar, Martin Lees, Reza Kashtiban, Jeremy Sloan, and Richard Walton, "Direct hydrothermal synthesis and physical properties of rare-earth and yttrium orthochromite perovskites," *Chem. Mater.*, vol. 23, no. 1, pp. 48–56, 2011, doi: 10.1021/cm102925z.

[29] Xheng Wang, Xau Sun, Dibal Yu, Bhadgi Zou, and Young Li, "Rare earth compound nanotubes," *Adv. Mater.*, vol. 15, no. 17, pp. 1442–1445, 2003, doi: 10.1002/adma.200305164.

[30] Masahiro Yoshimura and Shigeyuki Somiya, "Hydrothermal synthesis of crystallized nano-particles of rare earth-doped zirconia and hafnia," *Mater. Chem. Phys.*, vol. 61, no. 1, pp. 1–8, 1999, doi: 10.1016/S0254-0584(99)00104-2.

[31] Jagannatha Reddy and Anil Kumar, "Synthesis, structural and spectroscopic investigation of $Gd_2(WO_4)_3$ phosphor," *J. Phys. Conf. Ser.*, vol. 1644, no. 1, 2020, doi: 10.1088/1742-6596/1644/1/012049.

[32] Xu Gan, Azil Jayatissa, Zou Yu, Xao Chen, and Micherano Li, "Hydrothermal Synthesis of Nanomaterials," *J. Nanomater.*, vol. 2020, 2020, doi: 10.1155/2020/8917013.

[33] Hamandei Hayashi and Yhameki Hakuta, "Hydrothermal Synthesis of metal oxide nanoparticles in supercritical water," *Materials (Basel).*, vol. 3, no. 7, pp. 3794–3817, 2010, doi: 10.3390/ma3073794.

[34] B. E. Etschmann., "An in situ XAS study of copper(I) transport as hydrosulfide complexes in hydrothermal solutions (25-592 °C, 180-600 bar): Speciation and solubility in vapor and liquid phases," *Geochim. Cosmochim. Acta*, vol. 74, no. 16, pp.

4723–4739, 2010, doi: 10.1016/j.gca.2010.05.013.

[35] Kunio Kawamura, Hiroki Nagayoshi, and Toshio Yao, "In situ analysis of proteins at high temperatures mediated by capillary-flow hydrothermal UV-vis spectrophotometer with a water-soluble chromogenic reagent," *Anal. Chim. Acta*, vol. 667, no. 1–2, pp. 88–95, 2010, doi: 10.1016/j.aca.2010.04.013.

[36] Anna Kaczmarek, Ying-Ya Liu, Pascal Van Der Voort, and Rik Van Deun, "Tuning the architecture and properties of microstructured yttrium tungstate oxide hydroxide and lanthanum tungstate," *Dalt. Trans.*, vol. 42, no. 15, pp. 5471–5479, 2013, doi: 10.1039/c3dt32699c.

[37] Jianlin Li, Qingliu Wu, and Ji Wu, "Handbook of Nanoparticles," *Handb. Nanoparticles*, 2015, doi: 10.1007/978-3-319-13188-7.

[38] Youseff Ben Smida, Riadh Marzouki, and Mohammed Faouzi Zid, "Synthesis, structural and electrical properties of a new cobalt arsenate $NaCo_2As_3O_{10}$," *J. Solid State Chem.*, vol. 221, pp. 132–139, 2015, doi: 10.1016/j.jssc.2014.09.029.

[39] Riadh. Marzouki, Youssef Ben Smida, Mannel Sonni, Maxim Avdeev, and Mohammed Faouzi Zid, "Synthesis, structure, electrical properties and $Na^+$ migration pathways of $Na_2CoP_{1.5}As_{0.5}O_7$," *J. Solid State Chem.*, vol. 285, no. August 2019, p. 121058, 2020, doi: 10.1016/j.jssc.2019.121058.

[40] Helen Kitchen, Simon Vallence, Jennifer Kennedy, Nuria Tapia-Ruiz, Lucia Carassit, Andrew harrason, and Duncan Gregory, "Modern microwave methods in solid-state inorganic materials chemistry: From fundamentals to manufacturing," *Chem. Rev.*, vol. 114, no. 2, pp. 1170–1206, 2014, doi: 10.1021/cr4002353.

[41] Saremi-Yarahmadi, Bala Vaidhyanathan, and Upul Wijayantha, "Microwave-assisted low temperature fabrication of nanostructured α-$Fe_2O_3$ electrodes for solar-driven hydrogen generation," *Int. J. Hydrogen Energy*, vol. 35, no. 19, pp. 10155–10165, 2010, doi: 10.1016/j.ijhydene.2010.08.004.

[42] Wael Eisa, Abdelrahman Abdelgawad, and Orlando Rojas, "Solid-State Synthesis of Metal Nanoparticles Supported on Cellulose Nanocrystals and Their Catalytic Activity," *ACS Sustain. Chem. Eng.*, vol. 6, no. 3, pp. 3974–3983, 2018, doi: 10.1021/acssuschemeng.7b04333.

[43] D. A. Lopatin, A. F. Guseva, N. N. Pestereva, E. L. Vostrotina, and L. I. Baldina, "Electrical Properties of Tungstates $Ln_2(WO_4)_3$ (Ln – Gd, Ho)," *KnE Mater. Sci.*, vol. 1, no. 1, p. 103, 2016, doi: 10.18502/kms.v1i1.570.

[44] Yanee Keereeta, Titipun Thongtem, and Somchai Thongtem, "Synthesis of lanthanum tungstate interconnecting nanoparticles by high voltage electrospinning," *Appl. Surf. Sci.*, vol. 351, pp. 1075–1080, 2015, doi: 10.1016/j.apsusc.2015.05.194.

[45] Songhun Yoon, Eunae Kang, Jin Kon Kim, Chul Wee Lee, and Jinwoo Lee, "Development of high-performance supercapacitor electrodes using novel ordered mesoporous tungsten oxide materials with high electrical conductivity," *Chem. Commun.*, vol. 47, no. 3, pp. 1021–1023, 2011, doi: 10.1039/c0cc03594g.

[46] Minshen Zhu, Wenjun Meng, Yan Huang, Yang Huang, and Chunyi Zhi, "Proton-insertion-enhanced pseudocapacitance based on the assembly structure of tungsten oxide," *ACS Appl. Mater. Interfaces*, vol. 6, no. 21, pp. 18901–18910, 2014, doi: 10.1021/am504756u.

[47] Shobhnath Gupta, Mahendra More, Dattatray Late, and Pravin Walke, "High-rate quasi-solid-state hybrid supercapacitor of hierarchical flowers of hydrated tungsten oxide nanosheets," *Electrochim. Acta*, vol. 366, 2021, doi: 10.1016/j.electacta.2020.137389.

[48] Amir Inamdar and Naom Naresh, "Highly efficient electro-optically tunable smart-supercapacitors using an oxygen-excess nanograin tungsten oxide thin film," *Sol. Energy Mater. Sol. Cells*, vol. 166, no. February, pp. 78–85, 2017, doi: 10.1016/j.solmat.2017.03.006.

[49] Kuo-Hsin Chang, Chi-Chang Hu, Chao-Ming Huang, Ya-Ling Liu, and Chih-I Chang, "Microwave-assisted hydrothermal synthesis of crystalline $WO_3$-$WO_3 \cdot 0.5H_2$ O mixtures for pseudocapacitors of the asymmetric type," *J. Power Sources*, vol. 196, no. 4, pp. 2387–2392, 2011, doi: 10.1016/j.jpowsour.2010.09.078.

[50] Gyoung Hwa Jeong, Hae-Min Lee, Ji-goo Kang, Heewoong Lee, Chang-Koo Kim, Jae-Hyeok Lee, Jae-Ho Kim, and Sang-Wook Kim, "$ZrO_2$-$SiO_2$ nanosheets with ultrasmall $WO_3$ nanoparticles and their enhanced pseudocapacitance and stability," *ACS Appl. Mater. Interfaces*, vol. 6, no. 22, pp. 20171–20178, 2014, doi: 10.1021/am505747w.

[51] Maryam Afsharpour, Samaneh Bayatpour, and Leila Seifikar Gomi, "Inorganic–Organic Hybrids of Tungsten Oxide as the High Performance Intercalation Supercapacitor Electrodes," *J. Inorg. Organomet. Polym. Mater.*, vol. 30, no. 7, pp. 2406–2417, 2020, doi: 10.1007/s10904-019-01422-7.

[52] A. Manuscript, "ce Ac pte d M us pt," pp. 0–12, 2019.

[53] Vaibhav Lokhandea, Abhishek Lokhandeb, Gon Namkoongc Jin Hyeok, and Kimb Taeksoo Jia, "Charge storage in $WO_3$ polymorphs and their application as

supercapacitor electrode material," *Results Phys.*, vol. 12, no. February 2019, pp. 2012–2020, 2019, doi: 10.1016/j.rinp.2019.02.012.

[54] Sun Hwa Parka,Young Heon Kimb, Tae Geol Leeb, Hyun Kyong Shonb, Hyun Min ParkabJae, and Yong Songbc, "Synthesis and electrochemical capacitance of long tungsten oxide nanorod arrays grown vertically on substrate," *Mater. Res. Bull.*, vol. 47, no. 11, pp. 3612–3618, 2012, doi: 10.1016/j.materresbull.2012.06.053.

[55] Tyler Mathis, Narendra Kurra, Xuehang Wang, David Pinto, Patrice Simon, and Yury Gogotsi, "Energy Storage Data Reporting in Perspective—Guidelines for Interpreting the Performance of Electrochemical Energy Storage Systems," *Adv. Energy Mater.*, vol. 9, no. 39, pp. 1–13, 2019, doi: 10.1002/aenm.201902007.

[56] Yury Gogotsi, and Reginald Penner, "Energy Storage in Nanomaterials - Capacitive, Pseudocapacitive, or Battery-like?," *ACS Nano*, vol. 12, no. 3, pp. 2081–2083, 2018, doi: 10.1021/acsnano.8b01914.

[57] Xuehang Wang, Tyler S. Mathis, Ke Li, Zifeng Lin, Lukas Vlcek, Takeshi Torita, Naresh Osti, Christine Hatter, Patrick Urbankowski, Asia Sarycheva, Madhusudan Tyagi, Eugene Mamontov, Patrice Simon, and Yury Gogotsi, "and Supercapacitors Begin ?," *Science (80-. ).*, vol. 343, no. March, pp. 1210–1211, 2014.

[58] Mirko Marracci, Bernardo Tellini, Marcantonio Catelani, and Lorenzo Ciani, "Ultracapacitor Degradation State Diagnosis via Electrochemical Impedance Spectroscopy," *IEEE Trans. Instrum. Meas.*, vol. 64, no. 7, pp. 1916–1921, 2015, doi: 10.1109/TIM.2014.2367772.

[59] Ibrahim M.Badawya, Abdussalam Elbannaa, Mohamed Ramadana, and Nageh Allama,

"Insights into the energy storage mechanism of hybrid supercapacitors with redox electrolytes by Electrochemical Impedance Spectroscopy," *Electrochim. Acta*, vol. 263, pp. 110–117, 2018, doi: 10.1016/j.electacta.2017.12.167.

[60] Nadia Laschuk, Bradley Easton, and Olena Zenkina, "Reducing the resistance for the use of electrochemical impedance spectroscopy analysis in materials chemistry," *RSC Adv.*, vol. 11, no. 45, pp. 27925–27936, 2021, doi: 10.1039/d1ra03785d.

[61] Anna Ragoisha, "Challenge for electrochemical impedance spectroscopy in the dynamic world," *J. Solid State Electrochem.*, vol. 24, no. 9, pp. 2171–2172, 2020, doi: 10.1007/s10008-020-04679-y.

[62] F. Rafik, H. Gualous, R. Gallay, A. Crausaz, and A. Berthon, "Frequency, thermal and voltage supercapacitor characterization and modeling," *J. Power Sources*, vol. 165, no. 2, pp. 928–934, 2007, doi: 10.1016/j.jpowsour.2006.12.021.

[63] Jean Macdonald, "Impedance spectroscopy," *Ann. Biomed. Eng.*, vol. 20, no. 3, pp. 289–305, 1992, doi: 10.1007/BF02368532.

[64] George Chen, "Supercapacitor and supercapattery as emerging electrochemical energy stores," *Int. Mater. Rev.*, vol. 62, no. 4, pp. 173–202, 2017, doi: 10.1080/09506608.2016.1240914.

[65] Hongyang Zhaoab, Jiale Xiaab, Dandan Yinab, Meng-Luoab ChunhuaYan, and YapingDu, "Rare earth incorporated electrode materials for advanced energy storage," *Coord. Chem. Rev.*, vol. 390, pp. 32–49, 2019, doi: 10.1016/j.ccr.2019.03.011.

[66] N. Pestereva, Guseva, I. Vyatkin, and D. Lopatin, "Electrotransport in tungstates $Ln_2(WO_4)_3$ (Ln = La, Sm, Eu, Gd)," *Solid State Ionics*, vol. 301, pp. 72–77, 2017, doi:

10.1016/j.ssi.2017.01.009.

[67] Soumya Kuriakose, Anjaly Jose, Mathew John, and Thomas Varghese, "Structural and optical characterization of lanthanum tungstate nanoparticles synthesized by chemical precipitation route and their photocatalytic activity," *Opt. Mater. (Amst).*, vol. 99, no. November 2019, p. 109571, 2020, doi: 10.1016/j.optmat.2019.109571.

[68] Marrero-Lópeza, Canales-Vázquez, and Ruiz-Morales, "High temperature properties of rare-earth tungstates $RE_2W_2O_9$," *J. Alloys Compd.*, vol. 622, pp. 557–564, 2015, doi: 10.1016/j.jallcom.2014.10.139.

[69] Merceya and Lüders, "The role of oxygen vacancies on the weak localization in $LaNiO_{3-\delta}$ epitaxial thin films," *J. Phys. Chem. Solids*, vol. 123, no. November 2017, pp. 1–5, 2018, doi: 10.1016/j.jpcs.2018.07.003.

[70] Porras-Vázquez, Dos Santos-Gómez, Marrero-López, and Enrique Losilla, "Effect of tri- and tetravalent metal doping on the electrochemical properties of lanthanum tungstate proton conductors," *Dalt. Trans.*, vol. 45, no. 7, pp. 3130–3138, 2016, doi: 10.1039/c5dt03833b.

# Chapter 3

## 3.0 Experimental

This chapter describes materials, reagents and synthetic routes used for the synthesis of gadolinium tungsten oxide, tellurium selenide and tellurium selenide-gadolinium tungsten oxide composite material.

### 3.1 Materials and Reagents

Aqueous ammonia solution ($NH_3$, 25-28 %, w/w %), hydrazine monohydrate ($N_2H_4$, 64-65 %, reagent grade, 98 %), 1-methyl-2-pyrrolidinone (anhydrous, 99.5 %), hydrochloric acid (ACS reagent, 37 %), acetone ($CH_3COCH_3$, 99 %), absolute ethanol ($C_2H_5OH$, 99.9 %), gadolinium (III) chloride hexahydrate ($GdCl_3 \cdot 6H_2O$, 99.999 % trace metals basis), sodium tungstate dehydrate ($Na_2O_4W \cdot 2H_2O$, 99.995 % trace metals basis), tellurium dioxide ($TeO_2$, 99.995 % trace metals basis), potassium hydroxide pellets (≥85 % KOH basis), polyvinylpyrrolidone (average mol wt 40,000), selenium powder (Se, 99 %), sodium borohydride powder ($NaBH_4$), nickel foam. All the chemicals were used without further purification except nickel foam which was soaked in 3 M HCl solution for 15 min in a sonicator and in a mixture of water and absolute ethanol for another for removal of impurities.



### 3.2 Chemical synthesis

#### 3.2.1 Hydrothermal synthesis of $Gd_2(WO_4)_3$

The $Gd_2(WO_4)_3$ nanoparticles were prepared by a simple hydrothermal technique where 0.6788 g $GdCl_3 \cdot 6H_2O$ and 0.6002 g $Na_2WO_4 \cdot 2H_2O$ were dissolved in 10 mL of deionized water

separately at room temperature under magnetic stirring for 10 min, and the two solutions were then mixed and stirred for another 10 min. 6 M of hydrochloric acid solution was used to adjust the pH of the mixture to ~1. The reason for adjusting the pH to ~ 1 was to form a precipitate. At this pH range, the mixture turned milky white forming a white precipitate. The mixture was then transferred into a 100 mL Teflon liner and sealed in autoclave. The hydrothermal temperature was set to 160 °C and the mixture was hydrothermally heated for 8 hr. The autoclave was then allowed to cool down naturally. The precipitate was collected, washed with alternating proportions of deionized water and ethanol for three times, dried in an oven at 120 °C for 1 h and annealed at 300 °C for 2 h. The formation of $Gd_2(WO_4)_3$ is based on the equation below:

$$2Gd^{3+} + 3WO_4^{2-} \rightarrow Gd_2(WO_4)_3 \quad (10)$$

### 3.2.2 Hydrothermal synthesis of $Te_ySe_x$

Prior to preparation of $Te_ySe_x$, tellurium nanoparticles were synthesized and used to further prepare $Te_ySe_x$ by incorporating selenium into the tellurium solution. For the synthesis of tellurium nanoparticles, 0.6 g of PVP (poly vinyl pyrrolidone) was put into a Teflon-lined stainless steel autoclave with a volume capacity of 100 mL and dissolved in 20 mL of double distilled water under vigorous magnetic stirring to form a homogeneous solution at room temperature. After that, 0.0798 g of tellurium dioxide ($TeO_2$, 0.5mmol) was put into that solution and dissolved, and then 1 mL of hydrazine hydrate (85%, w/w %) and 2 mL of aqueous ammonia solution (25-28%, w/w %) were added into the mixed solution, respectively. The final solution was clear and turned dark brown with an addition of small amount of sodium borohydride, and distilled water was added again to up to 80% capacity of the total volume of

the Teflon vessel. The container was closed and maintained at 180 °C. When the reaction had proceeded for 4 h, it was cooled to room temperature rapidly with cold tap water.

In preparation of the $T_ySe_x$, 37 mL of freshly prepared tellurium nanowires (~0.4 mmol) was precipitated by adding about 100 mL of acetone. The precipitated Te nanowires were then dispersed in 79 mL of deionised water with magnetic stirring at room temperature for about 1 hour. Se powder (0.8 mmol) dissolved in 1 mL of hydrazine hydrate (85%, wt/wt %) was slowly added to the previous solution (solution mixture with molar ratios of 1:2 for [Te]: [Se]). The mixed solution was kept at 40 °C for 12 h with magnetic stirring. Finally, the mixed solution was kept at 80 °C for another 12 h without stirring.

### 3.2.3 Synthesis of $Gd_2(WO_4)_3$/ $Te_ySe_x$ composite material

The procedure of the nanocomposite material followed that of a one pot hydrothermal technique. A solution mixture of 0.6788 g $GdCl_3 \cdot 6H_2O$ and 0.6002 g $Na_2WO_4 \cdot 2H_2O$ which was adjusted to a pH value of ~1 with 6 M hydrochloric acid was mixed with a freshly prepared solution of tellurium selenide (with molar ratios of 1:2 for [Te]: [Se]) in a 100 mL Teflon-lined stainless-steel autoclave and hydrothermally treated at 160 °C for 12 h. The precipitate was collected, washed with alternating proportions of deionized water and ethanol for three times, dried in an oven at 120 °C for 1 h and annealed at 800 °C for 6 h.



## 3.3 Analytical techniques

### 3.3.1 Fourier Transmission Infrared Spectroscopy

FTIR is a qualitative characterization technique that is used to identify functional groups that are present in a sample/material. When IR radiation is passed through a sample, some radiations are absorbed and others are transmitted through the sample. Since different materials are

composed of different atoms and different atomic arrangement, they absorb IR radiation at different regions (wavelengths, measured in $cm^{-1}$) producing a positive identification of every kind of chemical bond and functional group present in the sample [1]

### 3.3.2 X-ray Diffraction

XRD is an analytical technique that is commonly used to retrieve information about the crystal structure, atomic spacing and the average particle size of materials can also be determined. The working principle of XRD is based on constructive interference of monochromatic X-rays that are generated by a cathode tube, filtered to produce monochromatic radiation which is then focused and directed towards the sample. From this interaction of incident rays and the sample, useful interferences are created when conditions fulfil Bragg's Law: $n\lambda = 2d\ sine\ \theta$, where n is an integer, $\lambda$ is the wavelength of the X-rays, $d$ is the interplanar spacing responsible for generating the diffraction and $\theta$ is the diffraction angle. According to this law, the wavelength of the X-rays is related to the diffraction angle and the lattice spacing in a crystalline sample. Diffraction directions are identified by scanning, processing and counting the X-rays through a range of $2\theta$ angles which are then converted to d-spacing that enables identification of the compound because each compound has unique set of $d$-spacing [2].



### 3.3.3 Scanning Electron Microscopy

SEM is a type of microscopic technique that fall under surface characterization techniques. It gives information about the composition, morphology, crystallographic information and surface topography of materials. SEM uses focussed beams of high energy electrons that are scanned across the surface of the sample which then produces signals at or near the surface of the sample that can be translated to the information desired. The advantages of SEM, include its capability to carry out analysis only on selected points on the sample and adjustable

magnifications from reading glass magnification. In this work, SEM images were recorded using SEM Gemini LEO 1525 Model microscope [3]

### 3.3.4 Transmission Electron Microscopy

TEM is considered as the most common and useful technique for characterizing nanomaterials in electron microscopy. This technique utilizes energetic electrons to reveal details about the morphology and crystallographic information of nanomaterials. In a typical TEM system, high energy electrons from an electron gun are accelerated down a column which then interact with and pass through a thin sample that results into scattered electrons. The scattered electrons are then then focussed by the electromagnetic lenses into an image/diffraction pattern/nano analytical pattern, depending on the operational mode chosen. In this study, TEM images were recorded using FEI Tecnai G2 20 transmission electron microscope coupled with EDX, operating at an acceleration voltage of kV [4, 5].

### 3.3.5 Ultraviolet-Visible Spectroscopy



UV-vis refers to a reflectance or absorption spectroscopy in the ultraviolet-region. This technique is used to characterise different types of organic, inorganic and biological materials by passing light through the sample and measuring the light that is absorbed by the sample. In theory, when a material is irradiated with electromagnetic waves; absorption, reflectance and scattering of electrons takes place. In UV-vis, when light is passed through the sample, absorption occurs whenever the frequency of the incoming light is equal to the energy difference between a molecules' ground and excited state resulting to excitation of electrons, a phenomenon called electron transition [6, 7]. The whole principle of UV-vis is governed by Beer Lambert's law which describes absorbance to be directly proportional to a samples

concentration, molar absorptivity and cuvette path length. The mathematical expression of the Beer Lambert's law is as follows:

$$A = \varepsilon bc \quad (11)$$

Where $\varepsilon$ is molar absorptivity of the material, $b$ is the path length of the cuvette and $c$ is the concentration of the sample. In this study, UV-vis was used for the determination of the bandgap of the synthesized materials.

### 3.3.6 Cyclic Voltammetry

CV is a powerful electrochemical technique that used study oxidation-reduction reactions of molecular species. This technique is based on measuring the current response when the electrode material is scanned at a specific scan rate and a linear sweep potential is applied between two potential limits. CV can be carried either in a three electrode or two electrode system depending on the experiment investigation but the resulting voltammogram obtained gives the same information needed. In a typical cyclic voltammogram, an information about reversibility, mass transfer and diffusion coefficient of the system can be obtained. There are three types of systems that are known to exist in cyclic voltammetry which are as follows: reversible, irreversible and quasi-irreversible systems. These systems are best analysed using the parameters developed by Nicholson and Shain for cyclic voltammetry, peak potential ($E_{pc}$, $E_{pa}$) and peak current ($i_{pc}$, $i_{pa}$) [8]. For reversible systems, the peak current is described by the Randles-Sevcik equation which is as follows:

$$i_p = (2.69 \times 10^5) n^{\frac{3}{2}} A C D^{\frac{1}{2}} v^{\frac{1}{2}} \quad (12)$$

Where $I_p$ is the forward peak current (A), n is the number of electrons exchanged per molecule of the anodic species, $A$ is the coated area of the electrode ($cm^2$), $D$ is the diffusion coefficient

($cm^2.s^{-1}$), *C* is the concentration ($mol.cm^{-3}$) and *v* is the scan rate ($V.s^{-1}$) [9, 10]. The formal potential for a reversible couple is given by:

$$E^0 = (E_{pa} + E_{pc})/2 \quad (13)$$

And the separation between the peak potentials is given by:

$$\Delta E_p = E_{pa} - E_{pc} = 59\, mV/n$$

The equation given for separation between the peak potentials is used to determine the number of electrons that are transferred for a redox reaction. In a reversible system, both the cathodic and anodic peaks are independent of the scan rates [11].

Irreversible and quasi-irreversible systems differ to reversible system by their dependency to scan rate. These systems have peak potentials that shift with scan rates:

$$E_p = E^0 - (\frac{RT}{\alpha n_a F})[0.78 - \ln(\frac{k^0}{D^{\frac{1}{2}}}) + \ln(\frac{\alpha n_a F v}{RT})^2] \quad (14)$$



Where α is the transfer coefficient, $n_a$ is the number of electrons that are involved. Since for these system a voltammogram is known to become more drawn out as αn decreases, then the peak current is given by:

$$i_p = (2.99 \times 10^5) n(\alpha n_a)^{\frac{1}{2}} A C D^{\frac{1}{2}} v^{\frac{1}{2}} \quad (15)$$

For quasi-irreversible systems, the current is dependent on both the charge transfer and mass transport. When compared to irreversible systems, quasi-irreversible voltammograms are more drawn out and have larger separation of peak potentials [12].

For SCs, CV is also used to calculate and determine the specific capacitance of the sample under in investigation. The following equation is used for the calculation of specific capacitance:

$$C_s = \frac{\int IdV}{2vm\Delta V} \quad (16)$$

Where $C_s$ is the specific capacitance (F $g^{-1}$), I is the current (A), V is the potential is V, *v* is the scan rate (V.$s^{-1}$), m is the mass of the active material (g) and ΔV is the potential window (V) [13, 14].

In this project, CV was carried through to study the reversibility of the sample, the electron kinetics of the materials under study and to determine their specific capacitance. In order to carry the above measurements, VMP-300 Biologic potentiostat operated on the EC-lab software at room temperature was used. 2 M KOH was used an aqueous electrolyte for the three electrode system, platinum wire as the counter electrode, Ag/AgCl as the reference electrode and nickel foam coated with the material under investigation was used as the working electrode. The measurements were carried through different scan rates, from 10 mV.$s^{-1}$ to 100 mV.$s^{-1}$.



### 3.3.7 Galvanostatic Charge-Discharge

GCD is the most common and widely used technique for the investigation of specific capacitance and the cycling stability of electrode materials. This technique is used in conjunction with cyclic voltammetry for determining electrochemical behaviour, but even though the same information is achieved in CV, GCD is considered to be more reliable and accurate. In a typical GCD, a current that is proportional to the mass of the active material is applied into the electrode system and a potential response over time as the system charges and

discharges is obtained. The specific capacitance from GCD is determined by using the following equation [15-17]:

$$C = \frac{4I\Delta t}{m\Delta V} \quad (17)$$

Where I is the current (A), Δt is the discharge time (s), m is the mass of the active electrode material ($g$) and $\Delta V$ is the potential window ($V$). As can be seen from the equation above, specific capacitance is more accurate because it is calculated directly from the charging and discharging profile over the applied current, unlike from the CVs which are dependent on the scan rates. In order to obtain the GCD measurements, the same instrument used for CV was used and the samples were scanned at different current densities. GCD has four areas of interest which are illustrated below: (i) The initial process (ii) Charging behaviour (iii) Ohmic potential drop and (iv) Discharging behaviour.

### 3.3.8 Electrochemical Impedance Spectroscopy



EIS is a powerful analysing technique that is used to evaluate barrier properties (corrosion resistance), coating performance, information about the kinetics and mechanistic properties based on coating deterioration and is also used to determine the equivalent circuit through data fitting [18-22]. EIS is normally presented by the inverse of Nyquist plots, which is described by imaginary (y-axis) vs real (x-axis) parts of the impendence. Fitting the Nyquist plot allows the EES kinetic processes to be modelled. The EIS spectra which is represented by Nyquist plot has two distinct parts of interest that explain the electrochemical behaviour of the sample: the semicircle (sometimes two semicircles) and a linear tail. The semicircle (which corresponds to high frequency values) gives description about the electron transfer process while the tail (which corresponds to low frequency values) gives information about diffusion process of the sample. In order to fully understand EIS, the equivalent circuit is usually plotted in conjunction

with nyquist plot so as to understand the electrical properties of the sample under investigation. The equivalent circuit is described by the following parameters: $R_S$ is the solution resistance between working electrode and reference electrode, $R_{ct}$ is the charge transfer resistance at the electrode/electrolyte interface, $Z_W$ is the diffusion impedance between working electrode and solution [23].

### 3.4 References


[1] A. Dutta, *Fourier Transform Infrared Spectroscopy*, vol. 2. Elsevier Inc., 2017.

[2] Gabriela Udriştioiu and Aboul-Enein, "X-Ray Diffraction: Instrumentation and Applications," *Crit. Rev. Anal. Chem.*, vol. 45, no. 4, pp. 289–299, 2015, doi: 10.1080/10408347.2014.949616.

[3] D. Su, "Advanced electron microscopy characterization of nanomaterials for catalysis," *Green Energy Environ.*, vol. 2, no. 2, pp. 70–83, 2017, doi: 10.1016/j.gee.2017.02.001.

[4] Senthil Kumar and Grace Pavithra, "*Characterization techniques for nanomaterials,*" Elsevier Inc., 2019.

[5] A. K. Singh, *Experimental Methodologies for the Characterization of Nanoparticles*. 2016.

[6] Y. N. Chang, M. Zhang, L. Xia, J. Zhang, and G. Xing, "The toxic effects and mechanisms of CuO and ZnO nanoparticles," *Materials (Basel).*, vol. 5, no. 12, pp. 2850–2871, 2012, doi: 10.3390/ma5122850.

[7] X. Huang and M. J. Beck, "Determining the oxidation state of small, hydroxylated metal-oxide nanoparticles with infrared absorption spectroscopy," *Chem. Mater.*, vol. 27, no. 8, pp. 2965–2972, 2015, doi: 10.1021/acs.chemmater.5b00259.

[8] G. Z. Chen, "Supercapacitor and supercapattery as emerging electrochemical energy stores," *Int. Mater. Rev.*, vol. 62, no. 4, pp. 173–202, 2017, doi: 10.1080/09506608.2016.1240914.

[9] J. Theerthagiri *et al.*, "Synthesis of Hierarchical Cobalt Phosphate Nanoflakes and Their Enhanced Electrochemical Performances for Supercapacitor Applications," *ChemistrySelect*, vol. 2, no. 1, pp. 201–210, 2017, doi: 10.1002/slct.201601628.

[10] G. A. Mabbott, "An introduction to cyclic voltammetry," *J. Chem. Educ.*, vol. 60, no. 9, pp. 697–702, 1983, doi: 10.1021/ed060p697.

[11] G. K. Veerasubramani, K. Krishnamoorthy, S. Radhakrishnan, N. J. Kim, and S. J. Kim, "In-situ chemical oxidative polymerization of aniline monomer in the presence of

cobalt molybdate for supercapacitor applications," *J. Ind. Eng. Chem.*, vol. 36, pp. 163–168, 2016, doi: 10.1016/j.jiec.2016.01.031.

[12] P. T. Kissinger and W. R. Heineman, "Cyclic voltammetry," *J. Chem. Educ.*, vol. 60, no. 9, pp. 702–706, 1983, doi: 10.1021/ed060p702.

[13] H. D. Yoo *et al.*, "'rocking-Chair'-Type Metal Hybrid Supercapacitors," *ACS Appl. Mater. Interfaces*, vol. 8, no. 45, pp. 30853–30862, 2016, doi: 10.1021/acsami.6b08367.

[14] C. Peng, J. Jin, and G. Z. Chen, "A comparative study on electrochemical co-deposition and capacitance of composite films of conducting polymers and carbon nanotubes," *Electrochim. Acta*, vol. 53, no. 2, pp. 525–537, 2007, doi: 10.1016/j.electacta.2007.07.004.

[15] J. Yan, J. Liu, Z. Fan, T. Wei, and L. Zhang, "High-performance supercapacitor electrodes based on highly corrugated graphene sheets," *Carbon N. Y.*, vol. 50, no. 6, pp. 2179–2188, 2012, doi: 10.1016/j.carbon.2012.01.028.

[16] K. S. Ryu *et al.*, "Electrochemical supercapacitor based on polyaniline doped with lithium salt and active carbon electrodes," *Solid State Ionics*, vol. 175, no. 1–4, pp. 765–768, 2004, doi: 10.1016/j.ssi.2003.12.049.



[17] S. Grover, S. Goel, V. Sahu, G. Singh, and R. K. Sharma, "Asymmetric Supercapacitive Characteristics of PANI Embedded Holey Graphene Nanoribbons," *ACS Sustain. Chem. Eng.*, vol. 3, no. 7, pp. 1460–1469, 2015, doi: 10.1021/acssuschemeng.5b00184.

[18] G. Bierwagen, D. Tallman, J. Li, L. He, and C. Jeffcoate, "EIS studies of coated metals in accelerated exposure," *Prog. Org. Coatings*, vol. 46, no. 2, pp. 149–158, 2003, doi: 10.1016/S0300-9440(02)00222-9.

[19] R. Severens, J. Bastiaanssen, and D. Schram, "High-quality a-Si:H grown at high rate using an expanding thermal plasma," *Surf. Coatings Technol.*, vol. 97, no. 1, pp. 719–722, 1997, doi: 10.1016/S0257-8972.

[20] J. R. Macdonald, "Impedance spectroscopy," *Ann. Biomed. Eng.*, vol. 20, no. 3, pp.

289–305, 1992, doi: 10.1007/BF02368532.

[21] J. Remmlinger, M. Buchholz, M. Meiler, P. Bernreuter, and K. Dietmayer, “State-of-health monitoring of lithium-ion batteries in electric vehicles by on-board internal resistance estimation,” *J. Power Sources*, vol. 196, no. 12, pp. 5357–5363, 2011, doi: 10.1016/j.jpowsour.2010.08.035.

[22] M. E. Huerta Garrido and M. D. Pritzker, “EIS and statistical analysis of copper electrodeposition accounting for multi-component transport and reactions,” *J. Electroanal. Chem.*, vol. 594, no. 2, pp. 118–132, 2006, doi: 10.1016/j.jelechem.2006.05.026.

[23] V. Freger, “Diffusion impedance and equivalent circuit of a multilayer film,” *Electrochem. commun.*, vol. 7, no. 9, pp. 957–961, 2005, doi: 10.1016/j.elecom.2005.06.020.

# Chapter 4

## 4.0 Results and discussions

The main focus of this chapter is on the characterization of the synthesized nanoparticles using various characterization techniques to better understand the properties of these nanoparticles. As discussed in chapter three, the nanoparticles under study are as follows: $Gd_2(WO_4)_3$, $Te_ySe_x$ and $Gd_2(WO_4)_3/Te_ySe_x$. The x and y values for $Te_ySe_x$ were determined experimentally from the masses of the synthesized materials.

$$TeO_2 \rightarrow Te \quad (18)$$

mass weighed for Te precipitate = 0.1099 g

mass weighed for TeSe precipitate = 0.1795 g, Then

$$X = m_{Te}/m_{TeSe} = 0.1099\ g/\ 0.1795\ g = 0.6122 \quad (19)$$

$$Y = (m_{TeSe}-m_{Te})/m_{TeSe} = (0.1795\ g - 0.1099\ g)/0.1795\ g = 0.3900 \quad (20)$$



where, $m_{Te}$ is the mass of tellurium precipitate weighed, $m_{TeSe}$ is the mass of tellurium selenide precipitate weighed. Therefore, tellurium selenide is presented as $Te_{0.39}Se_{0.61.}$

### 4.1 Structural characterization

#### 4.1.1 Fourier Transform Infrared Spectroscopy (FT-IR)

PerkinElmer Spectrum 100 FTIR Spectrometer was used in the range 400-4000 $cm^{-1}$ to examine the functional groups present in the parent material of $Gd_2(WO_4)_3$ and the functionality changes after tellurium selenide has been incorporated. It is expected that $Gd_2(WO_4)_3$ be comprised of bands corresponding to tungsten-oxide bonds (W-O), tungsten-water molecules (W-$OH_2$) and gadolinium-tungsten metal-metal bonds (Gd-W). The recorded

spectra of gadolinium tungsten oxide after annealing at 300 °C for 2 h in Figure 4.1a shows that the broad absorption band observed at ~ 3359 $cm^{-1}$ and the bands observed at ~ 2032 $cm^{-1}$, ~1632 $cm^{-1}$, ~ 1419 $cm^{-1}$ are due to structural water molecules (δHOH), δ (OH) bending and stretching vibrations, respectively [1- 4]. The absorption band seen ~ 1122 $cm^{-1}$ are due to the insertion of a proton into tungsten oxide. The absorption band seen ~ 997 $cm^{-1}$ is assigned to W=O stretching band. The broad band observed between 1000 and 500 $cm^{-1}$ is attributed to tungsten-oxygen framework vibrations. These several peaks tha are observable from 940-598 $cm^{-1}$ belong to the stretching vibrations of O-W-O [5-9]. The recorded FT-IR spectra of $Te_{0.39}Se_{0.61}$ in Figure 4.1a shows the absorption band at ~ 1732 $cm^{-1}$ corresponding to water molecules, and observable peaks at ~ 798-540 $cm^{-1}$ which correspond to symmetrical equatorial and asymmetrical axial stretching vibrations of Te-O bonds [10-13]. Peaks below 500 $cm^{-1}$ are due to metal frameworks.



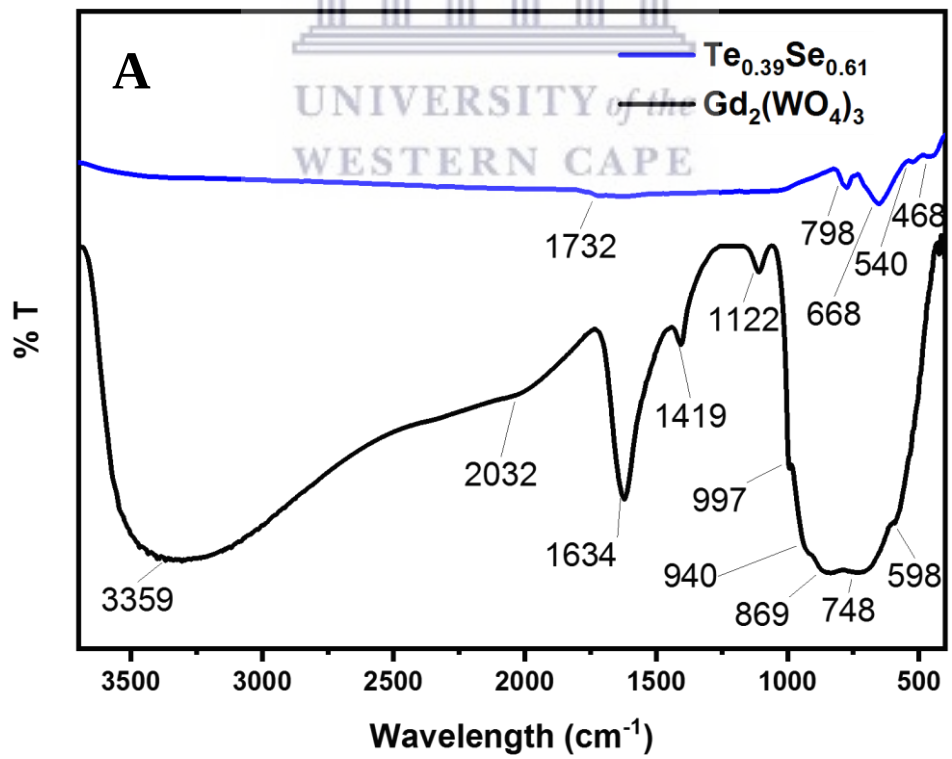

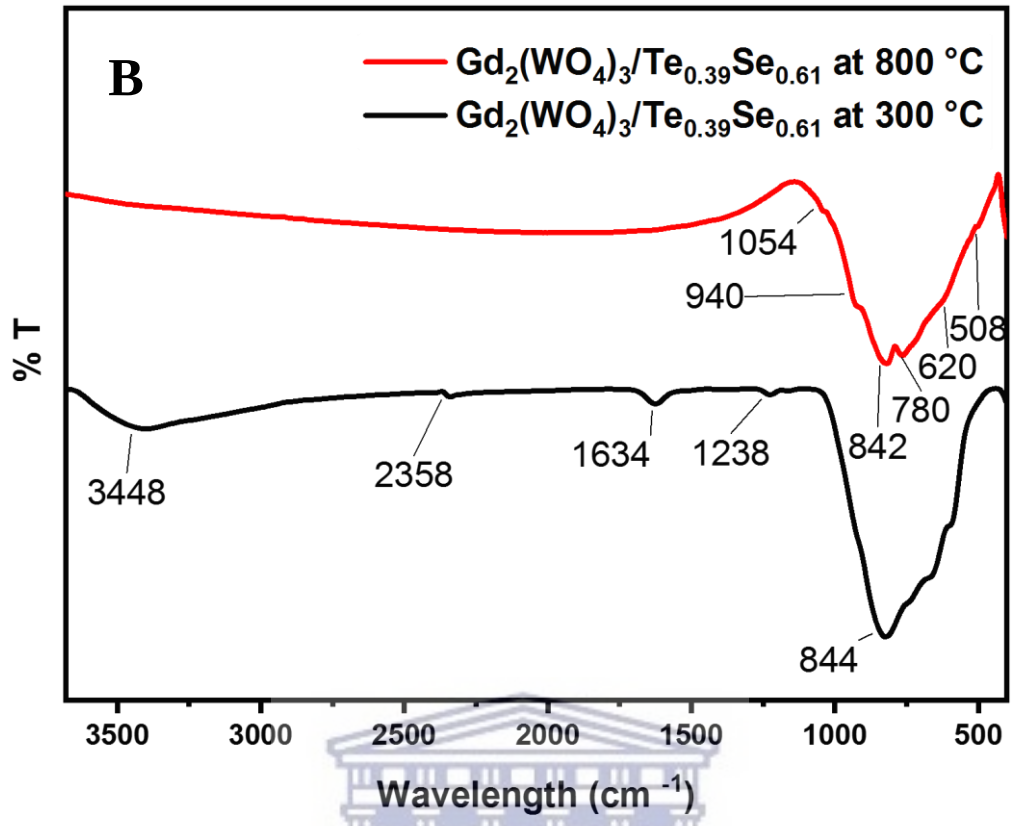


**Figure 4.1:** Overlaid FT-IR spectra of (**A**) $Gd_2(WO_4)_3$ and $Te_{0.39}Se_{0.61}$ (**B**) $Gd_2(WO_4)_3/Te_{0.39}Se_{0.61}$ nanocomposites at two different annealing temperatures.



Figure 4.1b shows the FT-IR spectrum of gadolinium tungsten oxide that is doped with tellurium selenide investigated at two different annealing temperatures. Theoretically, at higher annealing temperatures, we would expect that volatile and/ unwanted impurities be removed from the structure of the synthesized particles. As can be seen from the recorded spectrum, water molecules observed at ~ 3448 $cm^{-1}$, 2358 $cm^{-1}$, 1634 $cm^{-1}$ and 12 38 $cm^{-1}$ at a temperature of 300 °C are completely removed at a temperature of 800 °C. It is also notable that the absorption bands that are characteristic of $Gd_2(WO_4)_3$ and $Te_{0.39}Se_{0.61}$ (Figure 4.1a) are still visible in the $Gd_2(WO_4)_3/Te_{0.39}Se_{0.61}$ nanocomposite revealing that the doping has occurred successfully. The absorption band seen at ~ 1122 $cm^{-1}$ for gadolinium tungsten oxide shifted to 1054 $cm^{-1}$ for the doped nanocomposite which still corresponds to proton insertion into

tungsten oxide. The absorption band seen at ~ 940 $cm^{-1}$ for the nanocomposite corresponds to W=O stretching band (997 $cm^{-1}$ for the parent material). The absorption bands observed at ~ 842 $cm^{-1}$, 780 $cm^{-1}$, 620 $cm^{-1}$ and 508 $cm^{-1}$ correspond to tungsten-oxygen frameworks vibrations and stretching vibration of Te-O bonds.

### 4.1.2 X-ray diffraction (XRD)

The structural analysis was further investigated using the X-ray diffraction technique to study the phase composition, crystallinity and size of the synthesized particles. XRD measurements were recorded using Bruker AXS D8 Advance diffractometer (voltage 40 KV; current 40 mA) at 2θ range 10-90 degrees. Figure 4.2 Shows the XRD patterns for (A) $Gd_2(WO_4)_3$ (B) $Te_{0.39}Se_{0.61}$ and (**C**) $Gd_2(WO_4)_3/Te_{0.39}Se_{0.61}$. The results obtained for XRD were refined using MATCH software so as to get only the available peaks for diffraction. It is observable in Figure 4.2 (A and B) that the sharp intense and well defined peaks reveal that they are in well crystallized nature. In Figure 4.2**C**, $Gd_2(WO_4)_3/Te_{0.39}Se_{0.61}$ annealed at 300 °C showed a broad peak observable at $2\theta \approx 24$ ° signifying poor crystallinity. This indicates that the nanocomposite remains amorphous around this annealing temperature [13]. Furthermore, the crystallinity of $Gd_2(WO_4)_3/Te_{0.39}Se_{0.61}$ was studied at a temperature of 800 °C and the change was recorded. After $Gd_2(WO_4)_3/Te_{0.39}Se_{0.61}$ composite was annealed at 800 °C, well-defined and sharp intense peaks emerged revealing a crystallized nature of the composite. This pattern agrees with the pattern seen in FT-IR i.e. at higher temperatures, water molecules and other unwanted impurities are removed from the structure resulting in purified structure and increased crystallinity [14].

The crystalline structure of $Gd_2(WO_4)_3$ exhibits a monoclinic crystal structure with unit cell parameters a = 7.3000 Å b = 7.5300 Å and c = 7.6800 Å. For the $Gd_2(WO_4)_3$ sample annealed

at 300 °C for 2 h, several intense diffraction peaks seen at $2\theta$ = 20.3°, 22.9°, 27.2°, 27.9°, 30.7°, 35.8°, 38.9°, 45.5°, 46.6°, 47.9°, 52.7°, 55.0°, 58.1°, 60.3° and 73.3° can be assigned to (001), (002), (102), (023), (112), (103), (200), (210), (104), (212), (105), (301), (312), (215) and (116) reflections of monoclinic $Gd_2(WO_4)_3$, respectively. The structure of $Te_{0.39}Se_{0.61}$ (Figure 4.2b) exhibits a tetragonal crystal structure that is described by unit cell parameters a = b = 7.6951 Å and c = 7.4815 Å. The $Te_{0.39}Se_{0.61}$ grew along the (101) plane which is observable by the long sharp peak when compared to other several peaks. The diffraction peaks seen at $2\theta$ = 23.5°, 29.4°, 41.3°, 43.6°, 45.3°, 47.8°, 51.5°, 56.0°, 61.4°, 65.0°, 68.1°, 71.6°, 76.9°, 78.2°,81.7° and 86.5° are assigned to (100), (101), (110), (102), (111), (200), (201), (112), (202), (210), (211), (113), (203), (301), (104) and (302) reflections of tetragonal $Te_{0.39}Se_{0.61}$, respectively. Figure 4.2C shows comparison of $Gd_2(WO_4)_3$ with $Gd_2(WO_4)_3/Te_{0.39}Se_{0.61}$ at two different annealing temperatures.

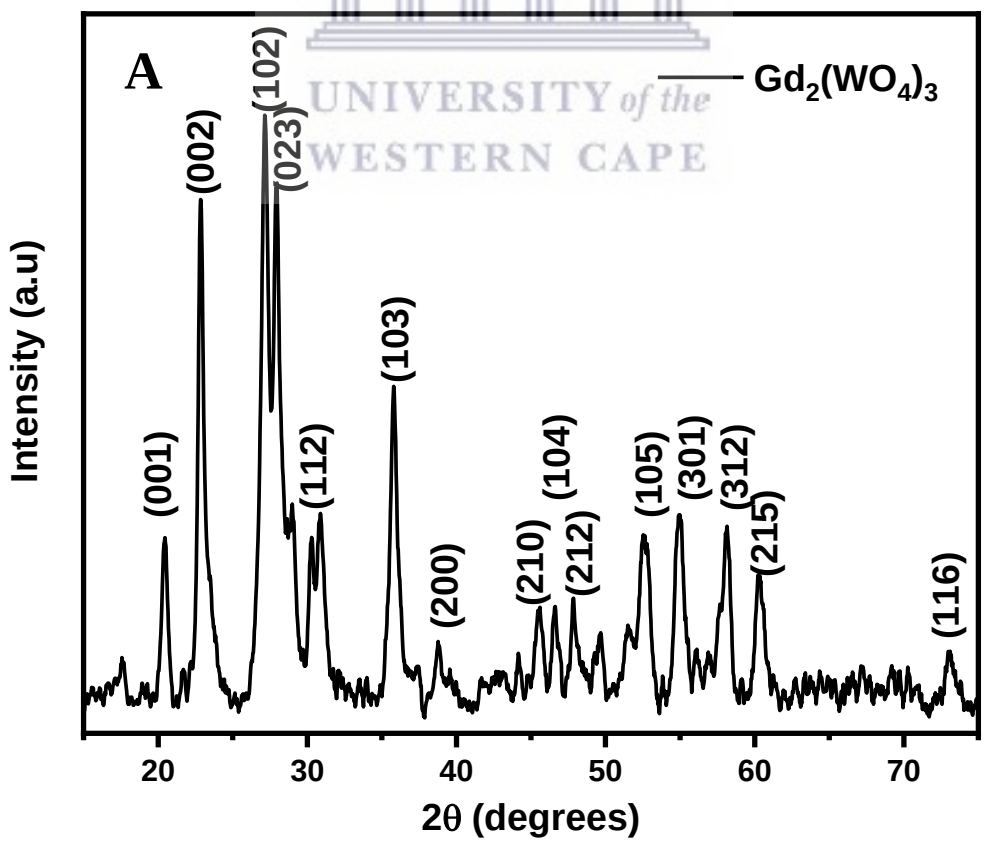

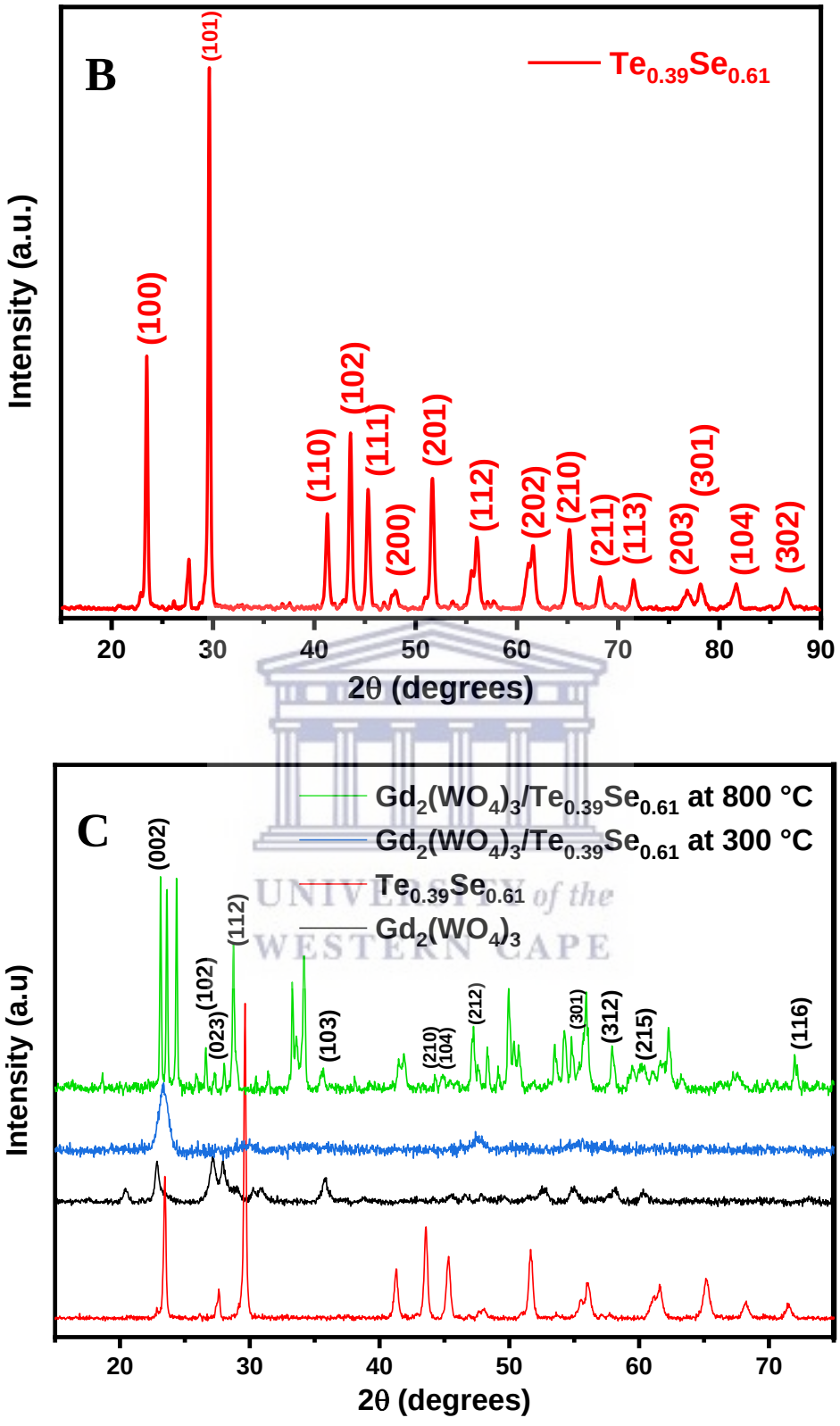


**Figure 4.2:** Powder XRD pattern for (**A**) $Gd_2(WO_4)_3$ (**B**) $Te_{0.39}Se_{0.61}$ (**C**) overlaid patterns of $Gd_2(WO_4)_3$, $Te_{0.39}Se_{0.61}$, $Gd_2(WO_4)_3$/ $Te_{0.39}Se_{0.61}$ at 300 °C and 800 °C annealing temperatures.

The peaks that were characteristic reflections of monoclinic $Gd_2(WO_4)_3$ at 800 °C are still present in $Gd_2(WO_4)_3/Te_{0.39}Se_{0.61}$. This suggests that gadolinium tungsten oxide has withhold its phase composition which is in good agreement with the functional groups retained in FT-IR after incorporating tellurium selenide at 800 °C. The crystal structure of $Gd_2(WO_4)_3/Te_{0.39}Se_{0.61}$ exhibits a monoclinic structure with unit cell parameters a = 8.9295 Å b = 24. 961 and Å c = 8.2973 Å. It is also observable that there are new peaks that have emerged at $2\theta$ = 23.7°, 33.4°, 34.2°, 41.7°, 50.1°, 53.6°, 54.3°, 62.3° and 67.6°. This is a clear indication of additional phases. The Powder XRD patterns were also used to calculate the crystal size of the synthesized particles. This was achieved by using Scherrer's equation given below:

$$D = k\lambda/\beta\cos\theta \quad (21)$$

where D is the average crystalline size, k is the Scherrer constant which is equal to 0.9, $\lambda$ is the wavelength of the X-ray which has the value 1.5406 Å (or 0.15404 nm), β is the full width at half maximum (FWHM) and $\theta$ is the glancing angle in radians. The calculated crystallite size for the synthesized compounds are given in table 2.



**Table 2:** Rietveld refinement parameters and calculated crystal size values for the synthesized samples.

| **Compound** | **Crystal system** | **Lattice parameters (Å)** | | | | **Crystal size (nm) D=kλ/βcosθ** |
|---|---|---|---|---|---|---|
| | | **a** | **b** | **c** | **β (°)** | |
| **$Gd_2(WO_4)_3$** | monoclinic | 7.3000 | 7.5300 | 7.6800 | 90.9 | 5.016 |
| **$Te_{0.39}Se_{0.61}$** | tetragonal | 7.6951 | 7.6951 | 7.4815 | 90.0 | 17.14 |
| **$Gd_2(WO_4)_3/Te_{0.39}Se_{0.61}$** | monoclinic | 8.9295 | 24.9613 | 8.2973 | 116.107 | 30.64 |

## 4.2 Surface morphology characterization

### 4.2.1 SEM and EDS analysis

The surface morphology was characterized with scanning electron microscopy coupled with corresponding Energy Dispersive X-ray spectroscopy for elemental composition. In this work, SEM images were recorded using SEM Gemini LEO 1525 Model microscope. Figure 4.3 shows SEM images and their corresponding EDS spectrums. $Gd_2(WO_4)_3$ has a spherical like morphology as observed in Figure 4.3A. Figure 4.3C shows spherical morphology with elongated rod-like particles for $Te_{0.39}Se_{0.61}$. The synthesized $Gd_2(WO_4)_3/Te_{0.39}Se_{0.61}$ shows a cube-like morphology in Figure 4.3E. The EDS spectrum seen for $Gd_2(WO_4)$ in Figure 4.3B shows that the structure has no impurity (the synthesized consists of only Gd, W and O).

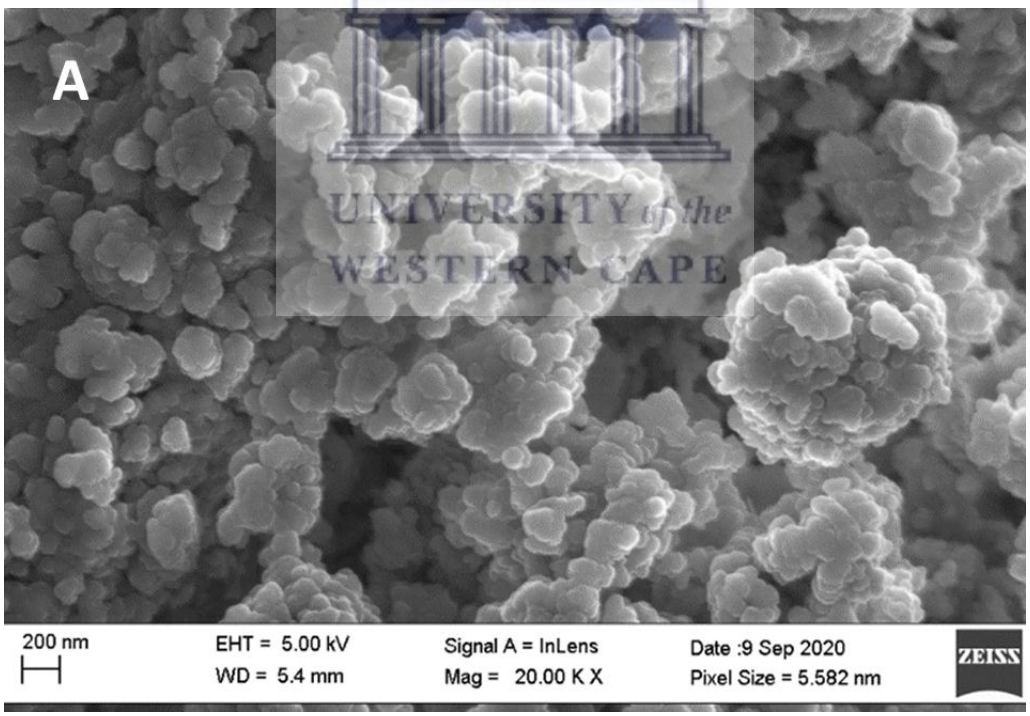

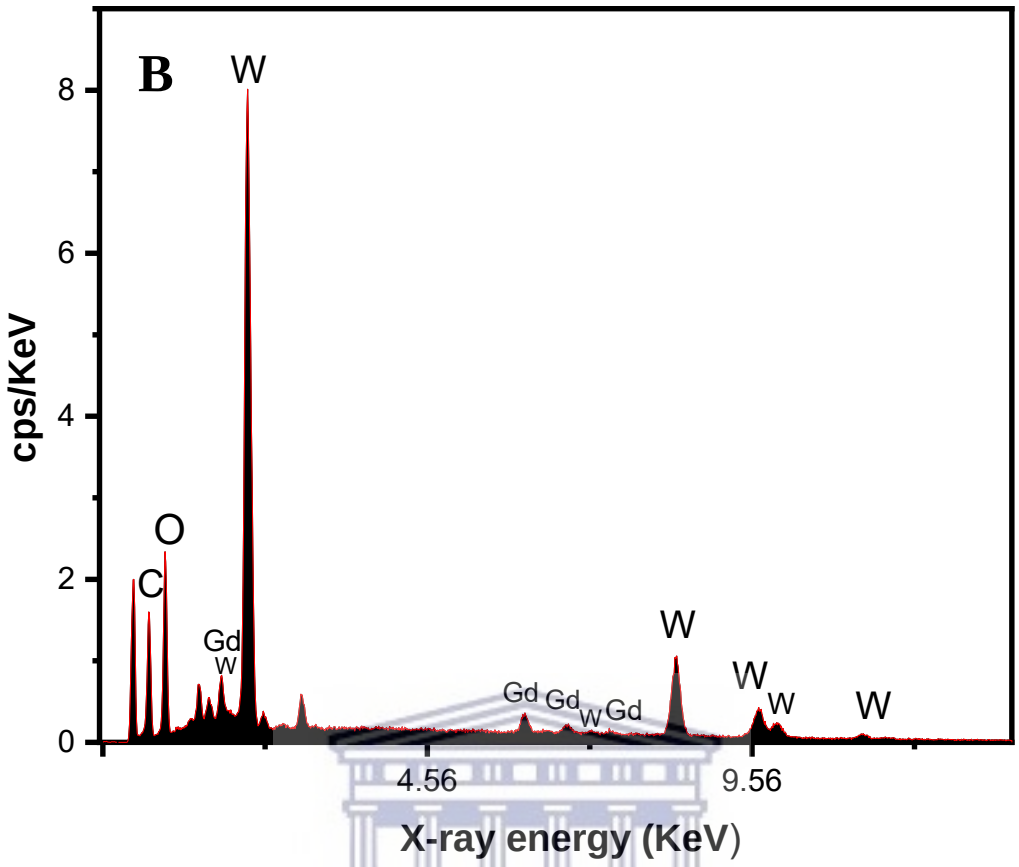


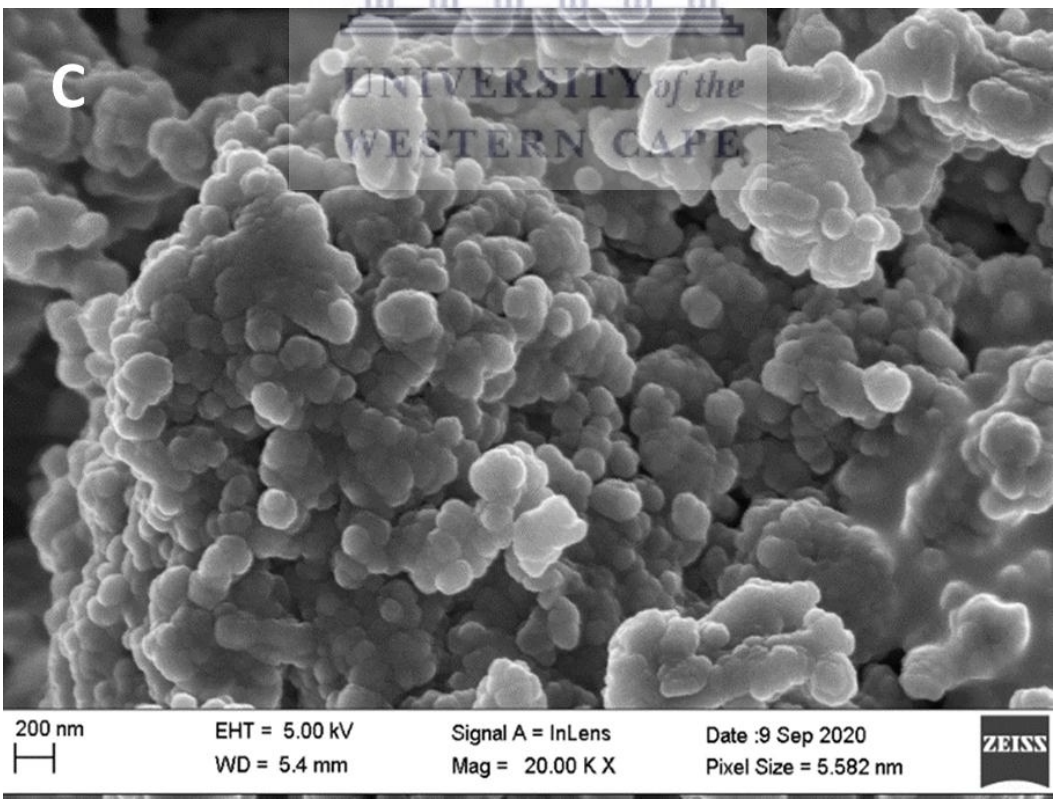

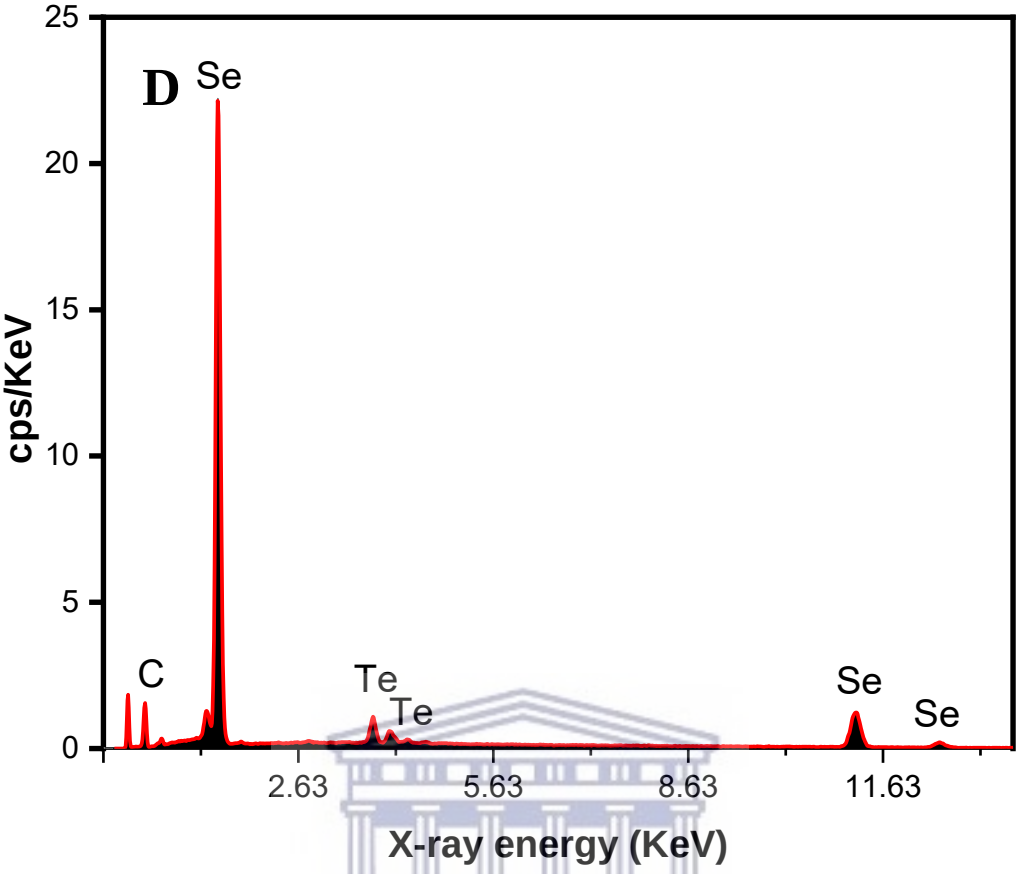


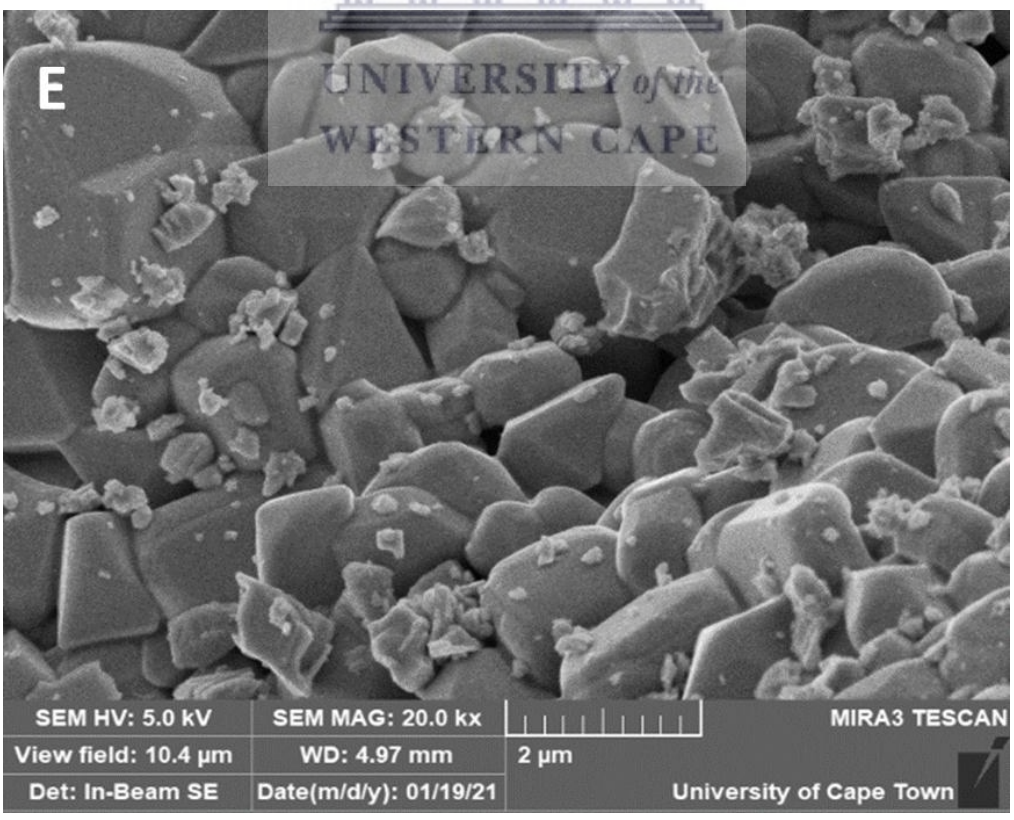

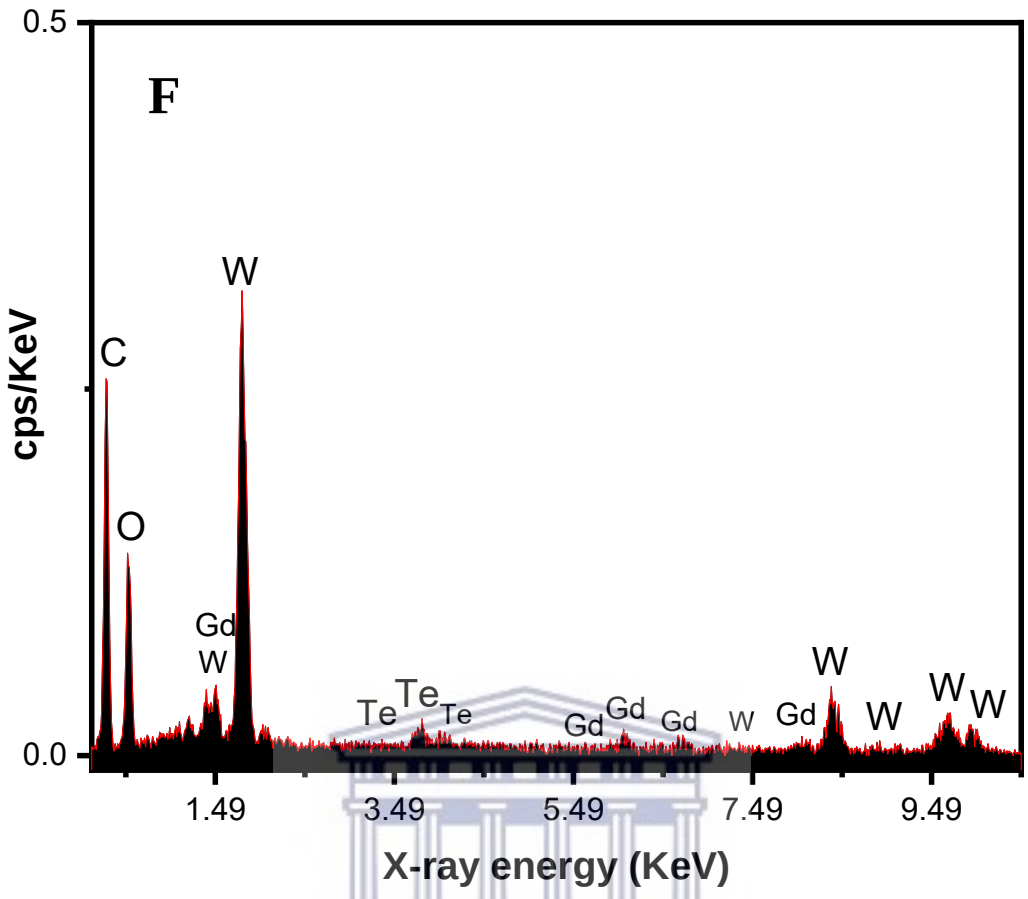


**Figure 4.3:** SEM images with corresponding EDS spectra for $Gd_2(WO_4)_3$, $Te_{0.39}Se_{0.61}$ and $Gd_2(WO_4)_3/Te_{0.39}Se_{0.61}$ respectively.



The carbon (C) which is observed in the spectrum comes from the carbon grid that was used to coat the prepared samples [16-18]. Also the EDS spectrum for $Te_{0.39}Se_{0.61}$ shows that the synthesized material is only made up of Se and Te elements. The synthesized $Gd_2(WO_4)_3/Te_{0.39}Se_{0.61}$ EDS spectrum is only showing Gd, W, O and Te. The reason for this lies with the possibility of overlap between REE with selenium. EDS is unable to resolve the peak overlaps with Pr, Eu, Gd, Ho, Er, Tm, and Lu [19, 20].

## 4.3 Internal structure

### 4.3.1 TEM and SAED pattern analysis

The internal structure of the synthesized nanoparticles was evaluated with Transmission Electron Microscopy technique (TEM) in conjunction with Selected Area Electron Diffraction (SAED) for confirmation of the crystal structure. In this study, TEM images were recorded using Tecnai F20 transmission electron microscope coupled with EDX, operating at an acceleration voltage of kV. It can be seen from Figure 4.4 that $Gd_2(WO_4)_3$ formed a cubic like structure (Figure 4.4A), while $Se_{0.61}Te_{0.39}$ showed a combination of nanowires and spherical nanoparticles (Figure 4.4D). The nanowires represent tellurium nanowires while the spheres observed are selenium particles. This combination of shapes is a clear indication that selenium telluride alloy has formed with success. The TEM micrograph of $Gd_2(WO_4)_3/Te_{0.31}Se_{0.61}$ composite did not reveal much information about the internal structure of the nanoparticle. Furthermore, the internal structure was investigated with High Resolution Transmission Electron Microscopy (HRTEM), of which the HRTEM micrographs were used to determine the crystal lattice spacing of the synthesized particles from a software called image J. Gadolinium tungsten oxide in Figure 4.4B showed a clear crystal lattice spacing of ~ 6.5 Å, selenium telluride showed multiple crystal lattice spacing of ~ 6.3 Å, 2.4 Å and 1.4 Å which are due to different phases of selenium and tellurium growing in different directions. $Gd_2(WO_4)_3/Se_{0.61}Te_{0.39}$ showed crystal lattice spacing of ~ 2.6 Å and 1.7 Å.

SAED pattern results for $Gd_2(WO_4)_3$, $Te_{0.39}Se_{0.61}$ and $Gd_2(WO_4)_3/Te_{0.39}Se_{0.61}$ in Figure 4.4 (C, F and I, respectively) reveal that the synthesized $Gd_2(WO_4)_3$ was single crystalline while both $Te_{0.39}Se_{0.61}$ and $Gd_2(WO_4)_3/Te_{0.39}Se_{0.61}$ were poly crystalline [15]. However, it can be seen that $Gd_2(WO_4)_3/Te_{0.39}Se_{0.61}$ SAED pattern result doesn't show clear ring patterns which strongly

suggest a semi-crystalline structure. Furthermore, planes (from XRD) have been linked with the corresponding crystals seen in SAED patterns.

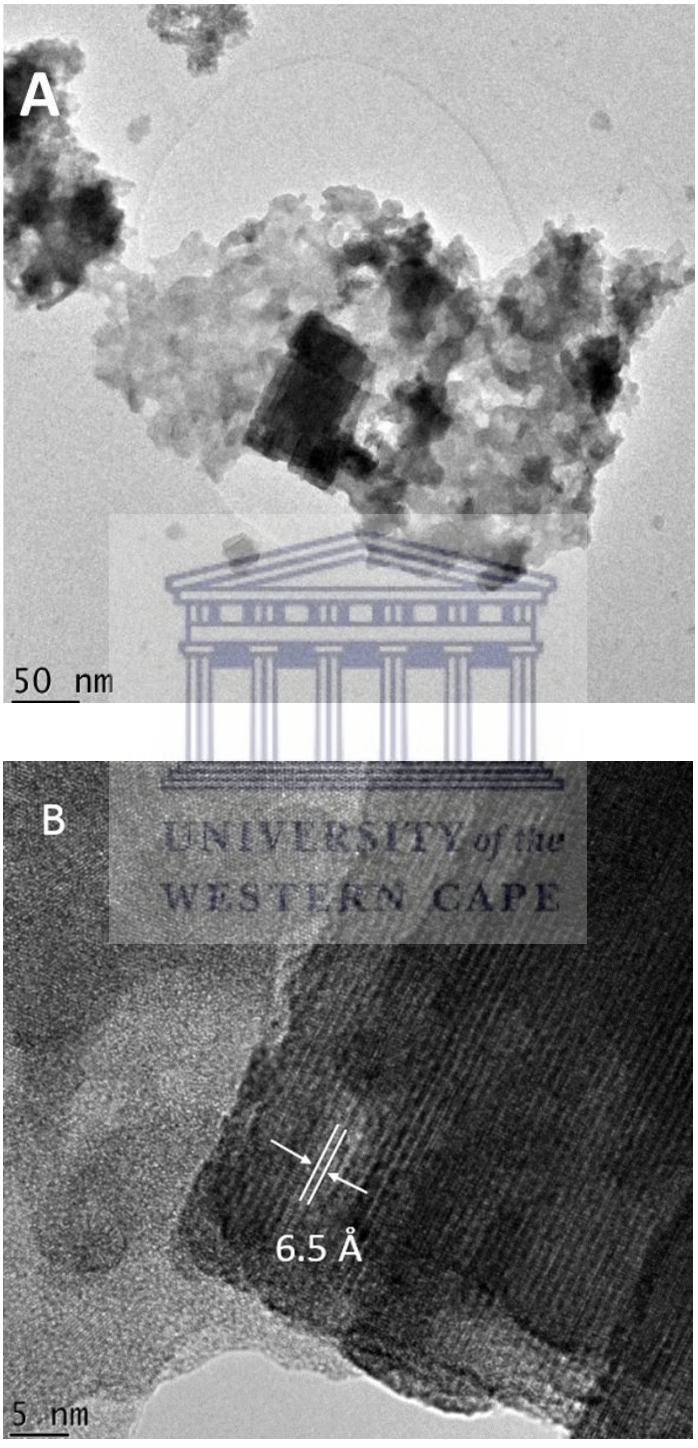

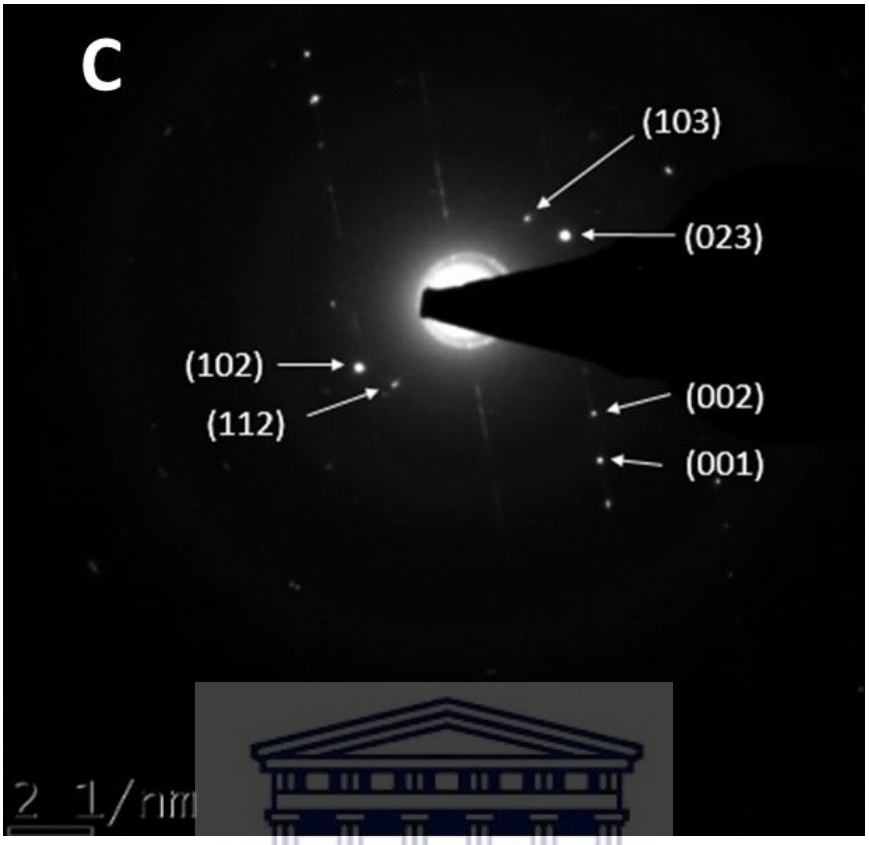


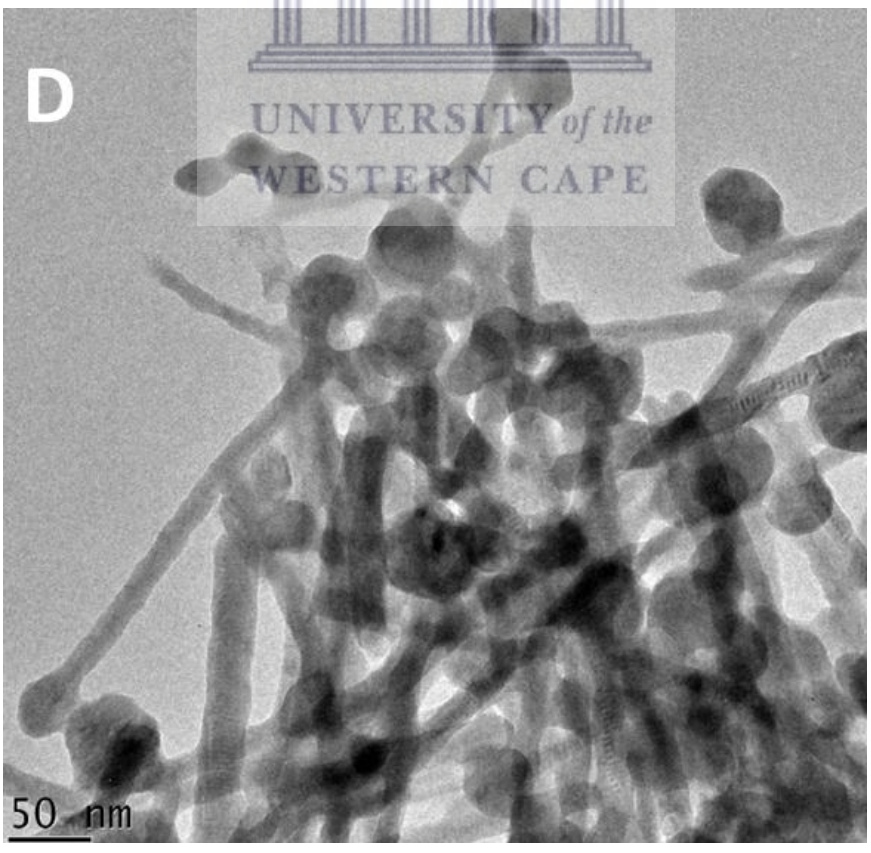

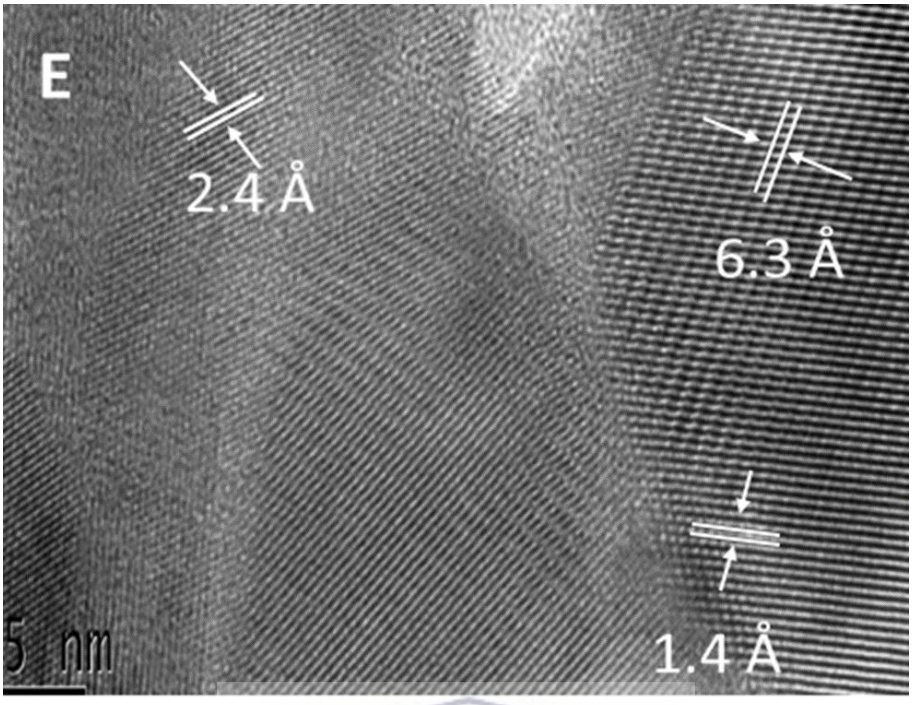


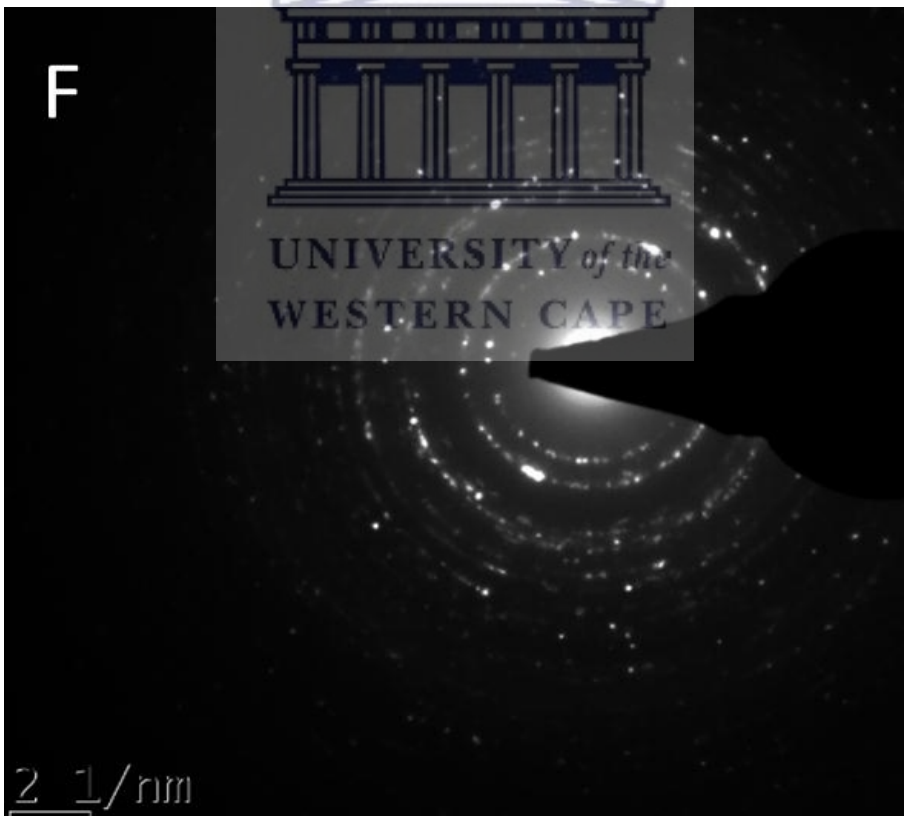

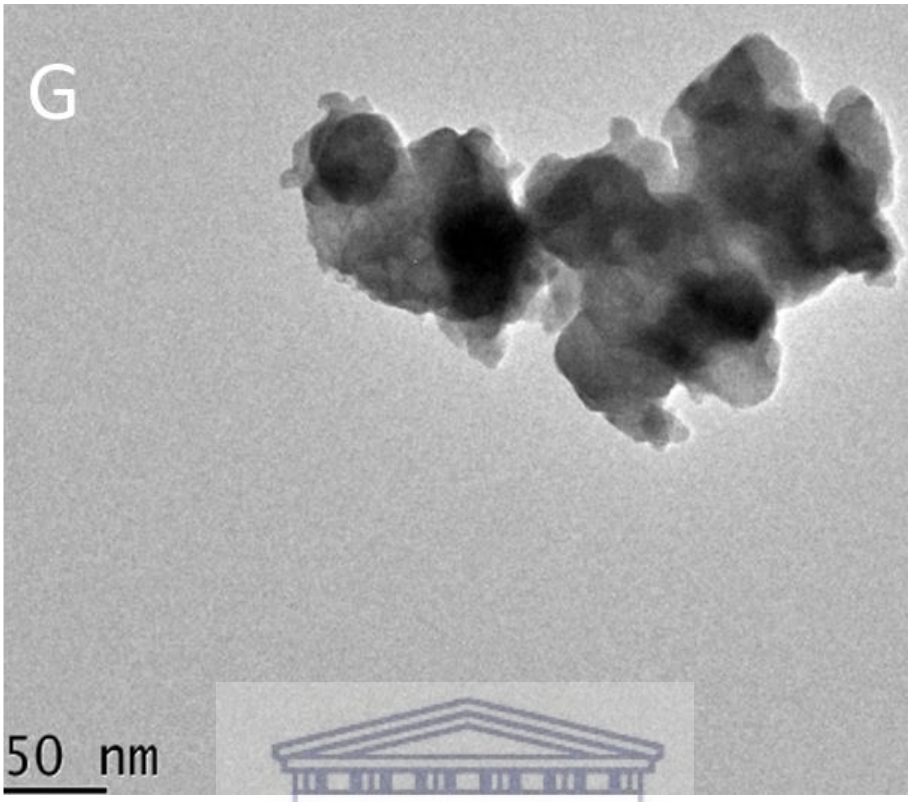


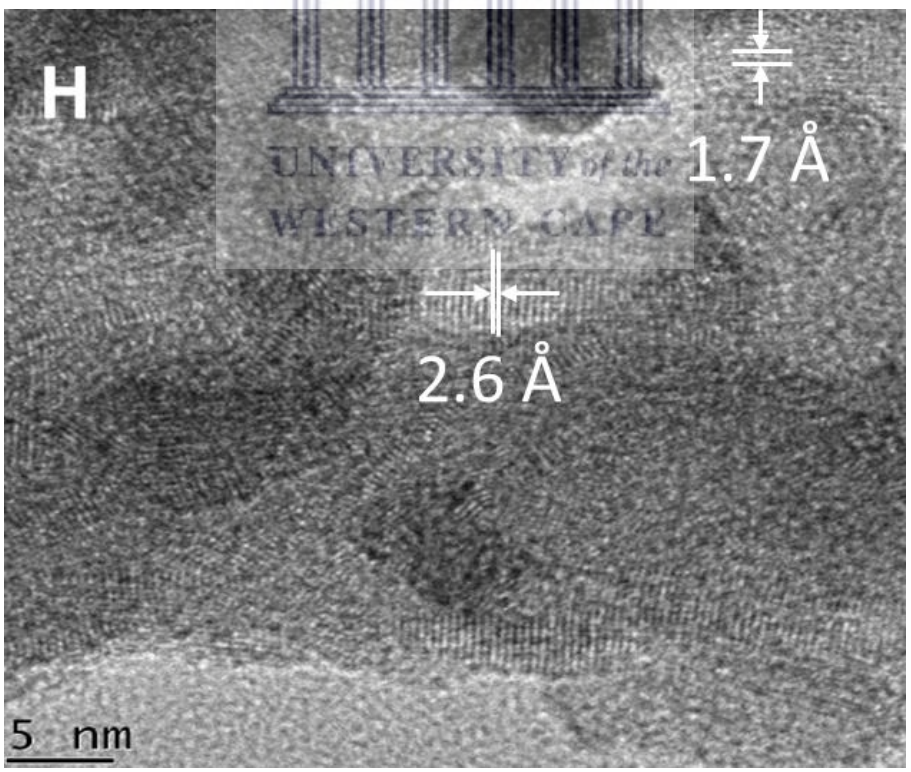

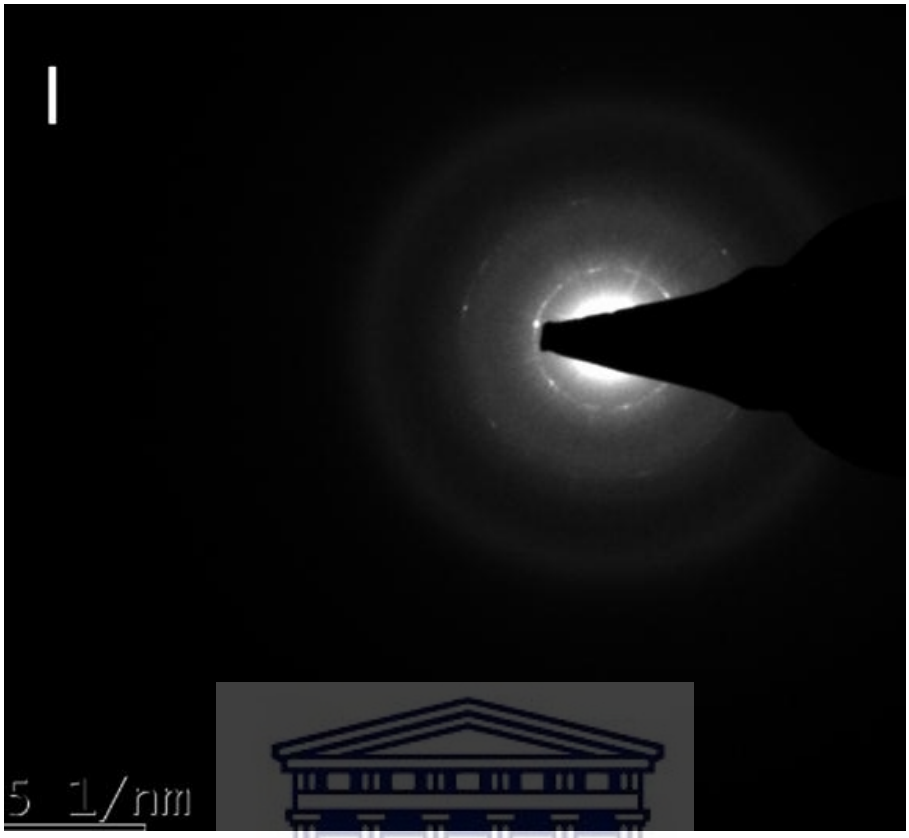


**Figure 4.4:** (A) TEM image for $Gd_2(WO_4)_3$ (B) HRTEM image of $Gd_2(WO_4)_3$ (C) SAED pattern for $Gd_2(WO_4)_3$ (D) TEM image for $Te_{0.39}Se_{0.61}$ (E) HRTEM image for $Te_{0.39}Se_{0.61}$ (F) SAED pattern for $Te_{0.39}Se_{0.61}$ (G) TEM image $Gd_2(WO_4)_3/Te_{0.39}Se_{0.61}$ (H) $Gd_2(WO_4)_3/Te_{0.39}Se_{0.61}$ (I) $Gd_2(WO_4)_3/Te_{0.39}Se_{0.61}$.



## 4.4 Optical properties analysis

### 4.4.1 Ultraviolet-Visible Spectroscopy

UV-vis absorption spectroscopy measurements were carried through to evaluate the linear optical absorption for the synthesized nanoparticles. All the synthesized nanoparticles ($Gd_2(WO_4)_3$, $Te_{0.39}Se_{0.61}$ and $Gd_2(WO_4)_3/Te_{0.39}Se_{0.61}$) were dispersed in water and left undisturbed for a period of two weeks. After two weeks has elapsed, the optical absorption spectra of the synthesized nanoparticles were measured between the wavelength range 190 –

800 nm and presented in Figure 4.5. Figure 4.5A shows characteristic absorption bands in the wavelength range 240 – 433 nm, 204 nm and 233 – 247 nm for $Gd_2(WO_4)_3$, $Te_{0.39}Se_{0.61}$ and $Gd_2(WO_4)_3/Te_{0.31}Se_{0.61}$ samples respectively. It is notable that $Gd_2(WO_4)_3$ shows a fall in reflectance before and after doping which is due to band transition from the occupied O 2p

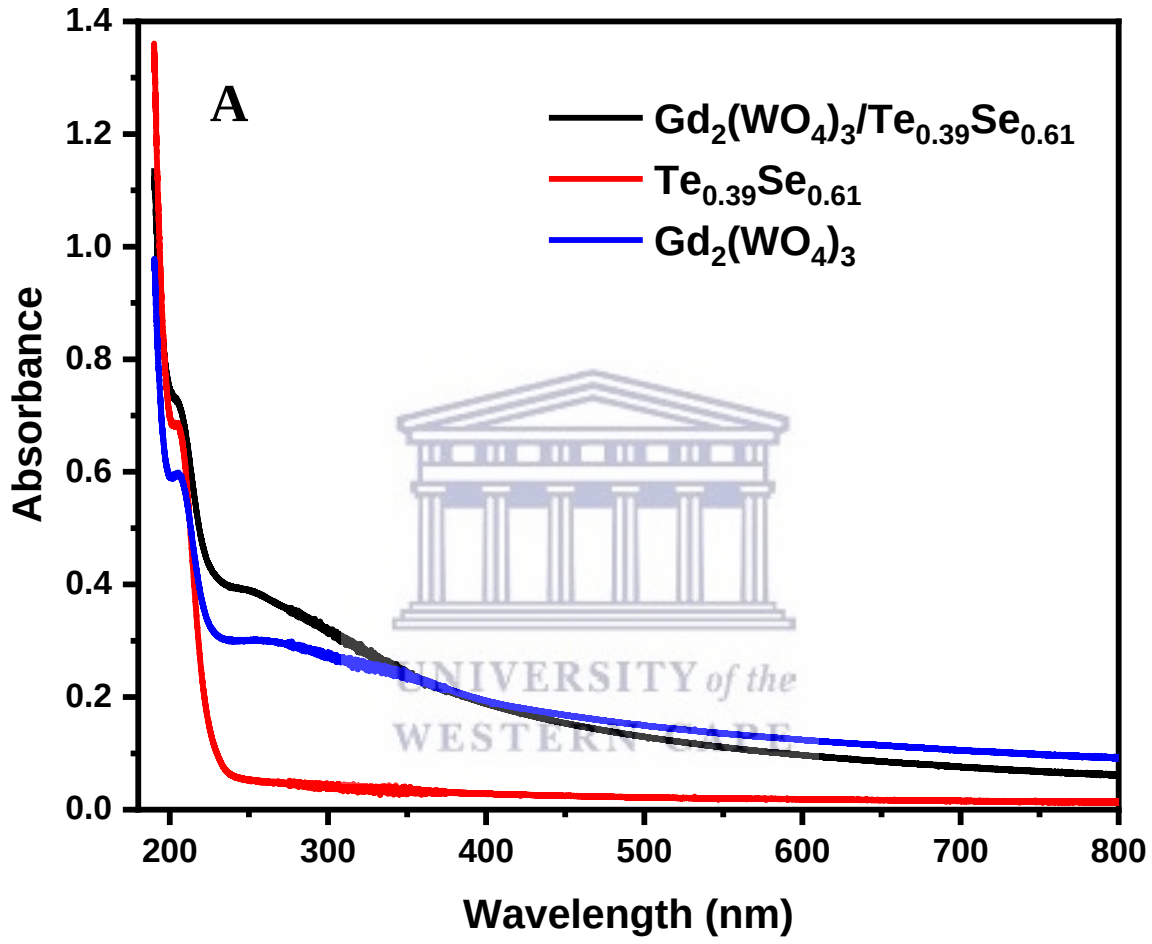

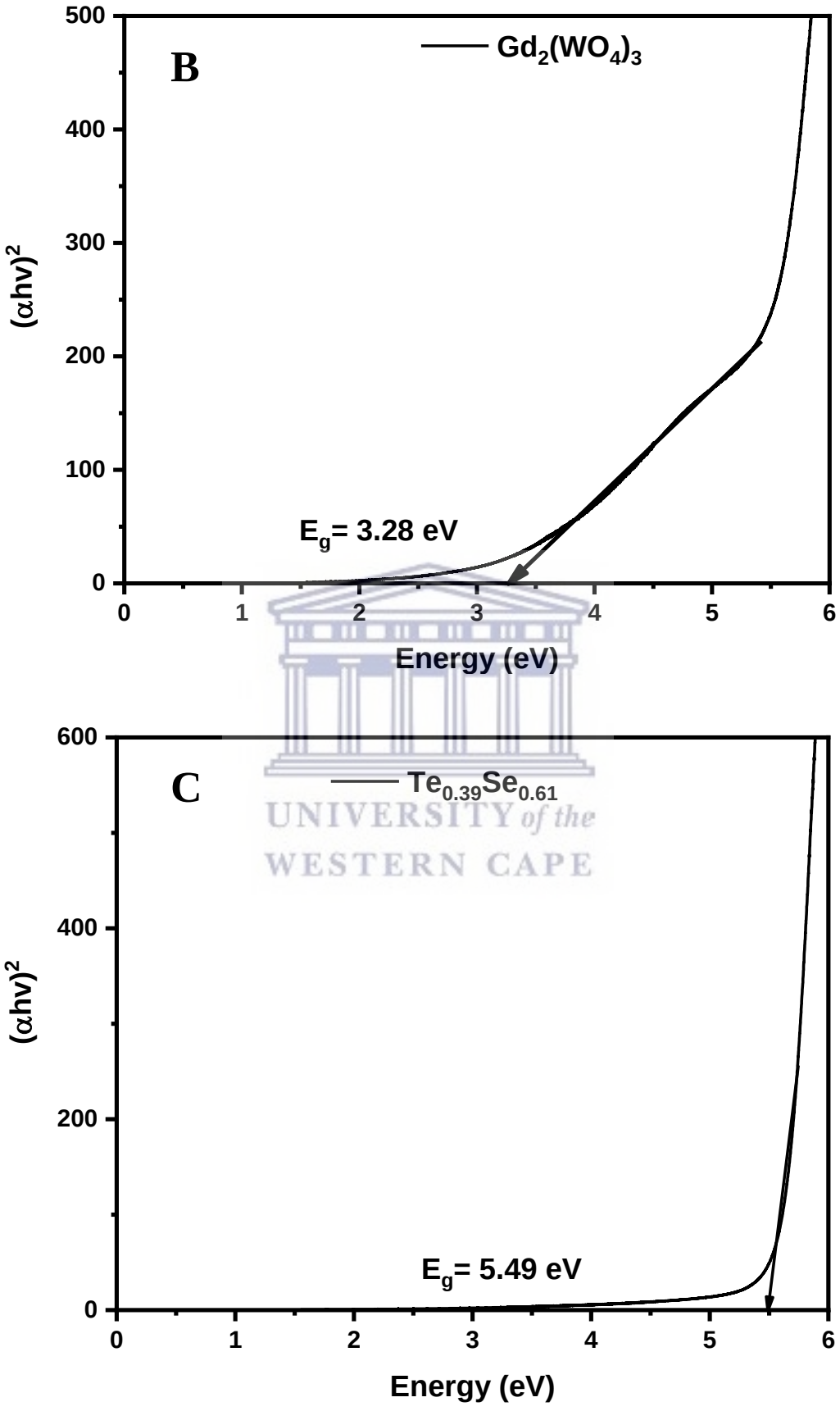

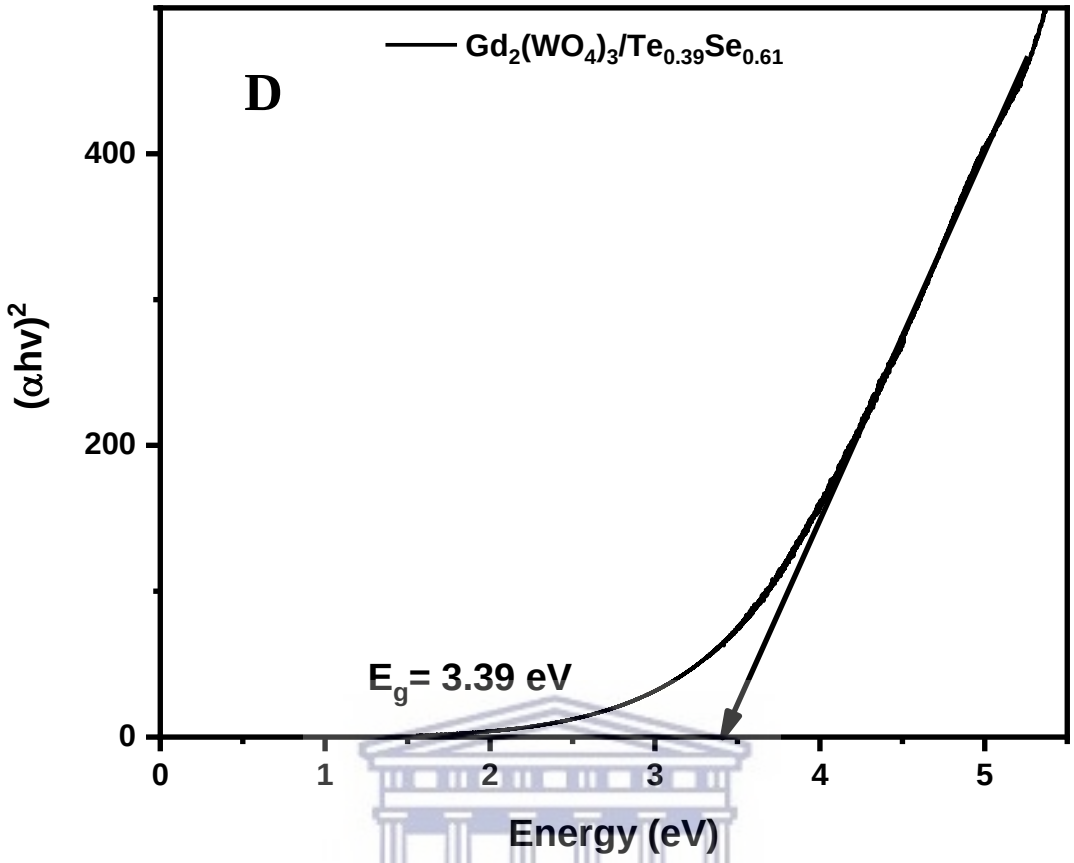


**Figure 4.5:** (A) Overlaid UV-vis spectra (B) Tauc plot for $Gd_2(WO_4)_3$ (C) Tauc plot for $Te_{0.39}Se_{0.61}$ (D) Tauc plot for $Gd_2(WO_4)_3/Te_{0.39}Se_{0.61}$.



orbital to the empty W 5d orbital [19-22]. The band gap energy ($E_g$) was also determined by plotting the product of photon energy versus photon energy, $(\alpha h\nu)^2$ vs $h\nu$. Then the band gap energy was found with the help of Tauc relation by extrapolating the straight line to zero absorption. The Tauc relation is described by the following equation:

$$\alpha h\nu = A\,[h\nu - Eg]^{\,n} \qquad (22)$$

where, α is the absorption coefficient, $h\nu$ is the photon energy, A is a band tailing parameter, $Eg$ is the optical band gap and n can be either 2 or ½ for direct and indirect transitions respectively. The results for band gap energy are summarized in table 6 below. The estimated band gaps at 3.28 eV ($Gd_2(WO_4)_3$), 5.49 eV ($Te_{0.39}Se_{0.61}$) and 3.39 eV ($Gd_2(WO_4)_3/Te_{0.39}Se_{0.61}$)

corresponds with the absorption edges around 269 nm, 228 nm and 256 nm, respectively. After incorporation of $Te_{0.39}Se_{0.61}$ to $Gd_2(WO_4)_3$, the band gap of gadolinium tungstate widened, resulting in poor semiconducting characteristics. This is probably due to the fact that, doped gadolinium tungstate showed an amorphous internal structure as seen from TEM and SAED patterns in Figure 4.4I.

**Table 3:** Band gap energy values for the synthesized nanoparticles from Tauc plot

| Sample | *Eg* (eV) |
|---|---|
| $Gd_2(WO_4)_3$ | 3.28 |
| $Gd_2(WO_4)_3/Te_{0.39}Se_{0.61}$ | 3.39 |



## 4.5 Size distribution

### 4.5.1 SAXS

The size distribution of the synthesized particles was studied and evaluated using SAXS. The summary of the size distribution is given in Figure 4.6 below. The PDDF function shows a solid sphere shape for $Gd_2(WO_4)_3$ and $Gd_2(WO_4)_3/Te_{0.39}Se_{0.61}$ with agglomerated particles. The PDDF distribution function also shows a poly-dispersion with r = 27 nm and r = 48 nm. The distribution by number in figure 4.6 b for $Gd_2(WO_4)_3$ had r = 5 nm with extended peaks at r = 12 nm, r = 19, r = 24 nm, r = 31 nm and r = 49 nm. But after incorporation of $Te_{0.39}Se_{0.61}$, the extended peaks were reduced (Figure 4.6d). The $Gd_2(WO_4)_3$ crystallinity for distribution by volume increased after $Te_{0.39}Se_{0.61}$ was incorporated.

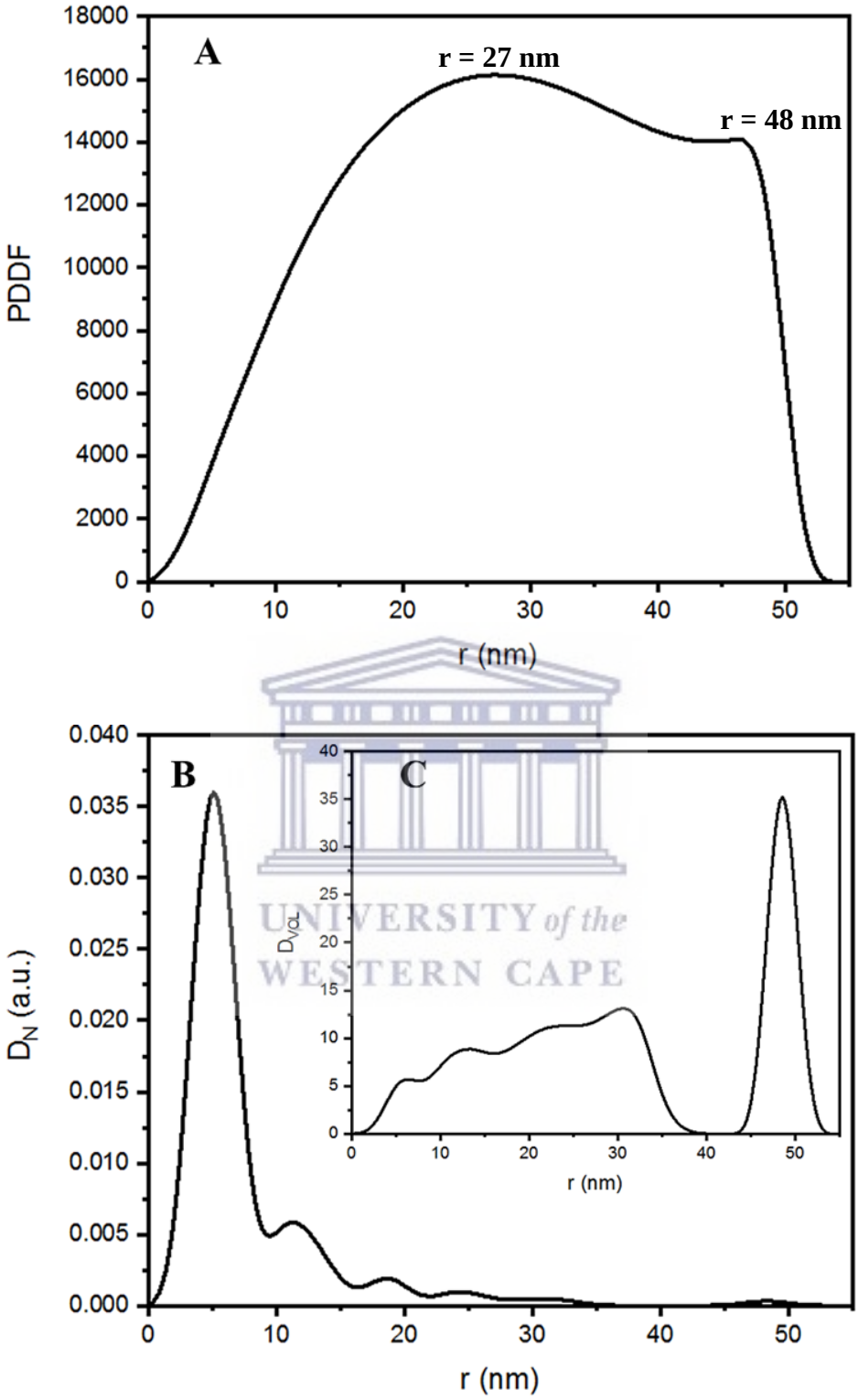

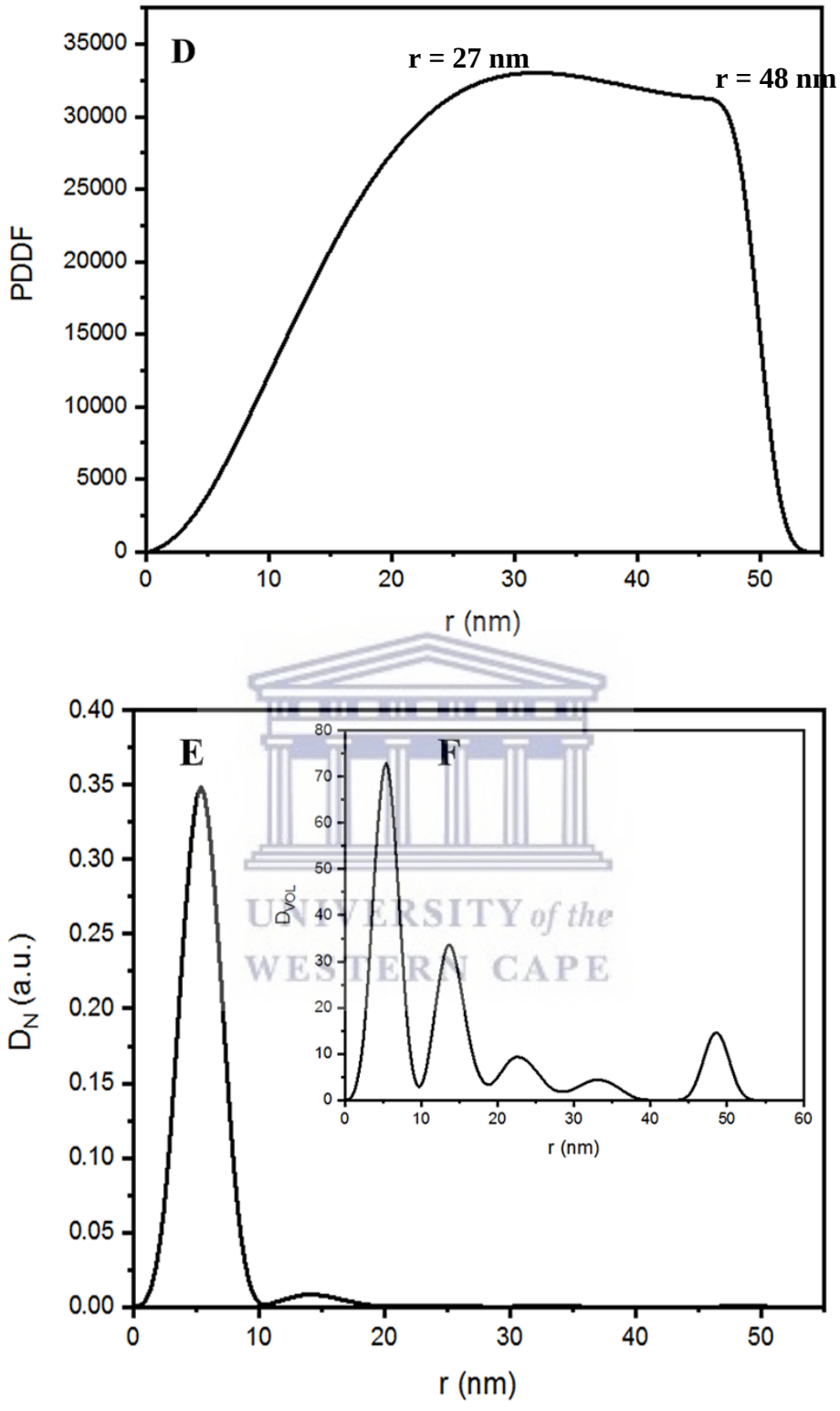


**Figure 4.6:** SAXS plot of the particle size distribution for (A-C) $Gd_2(WO_4)_3$, (D-F) $Gd_2(WO_4)_3/Te_{0.39}Se_{0.61}$.

## 4.6 Electrochemical characterization

### 4.6.1 Performance in three-electrode configuration

In order to determine the possible usage of the synthesized materials as suitable candidates for high performing super capacitive electrode materials, their electrochemical evaluation should be determined. In achieving that, the electrochemical evaluations for all the synthesized materials were carried out at room temperature using VMP-300 Biological potentiostat operated with the build in EC-lab software. All tests were carried out in a three-electrode system, where a platinum wire, Ag/AgCl and the prepared electrode coated on a nickel foam were used as counter, reference and working electrodes, respectively. To investigate the reduction and oxidation process of the prepared electrodes, a technique known as cyclic voltammetry (CV) was carried out at various scan rates. Galvanostatic charge-discharge (GCD) at various current densities and electrochemical impedance spectroscopy (EIS) techniques were also performed to investigate other electrochemical properties such as the charge and discharging rates, and electron mobility, respectively. All the electrochemical techniques were carried in 2 M KOH aqueous electrolyte.



#### 4.6.1.1 Cyclic Voltammetry

Figure 4.7 shows a comparative cyclic voltammetry electrochemical performance of precursor materials for $Gd_2(WO_4)_3$, $Se_{0.61}Te_{0.39}$ and $Gd_2(WO_4)_3/Te_{0.39}Se_{061}$. All samples were scanned from -0.4 V to 0.5 V giving a potential window of 0.9 V. The cyclic voltammogram profiles reveal that incorporation of $Te_{0.31}Se_{0.61}$ to $Gd_2(WO_4)_3$ resulted in an increase in current response at scan rate 10 $mVs^{-1}$ with large peak separations. The maximum anodic current ($I_{pa}$) observed for $Gd_2(WO_4)_3$ was 13.4 mA and the maximum cathodic current ($I_{pc}$) was observed to be -6.7 mA. The current/peak ratio ($I_{pa}/I_{pc}$) calculated was not equal to 1 which suggested a quasi-

reversible system (as well as other samples). Furthermore, another characteristic feature of the electrode was investigated by

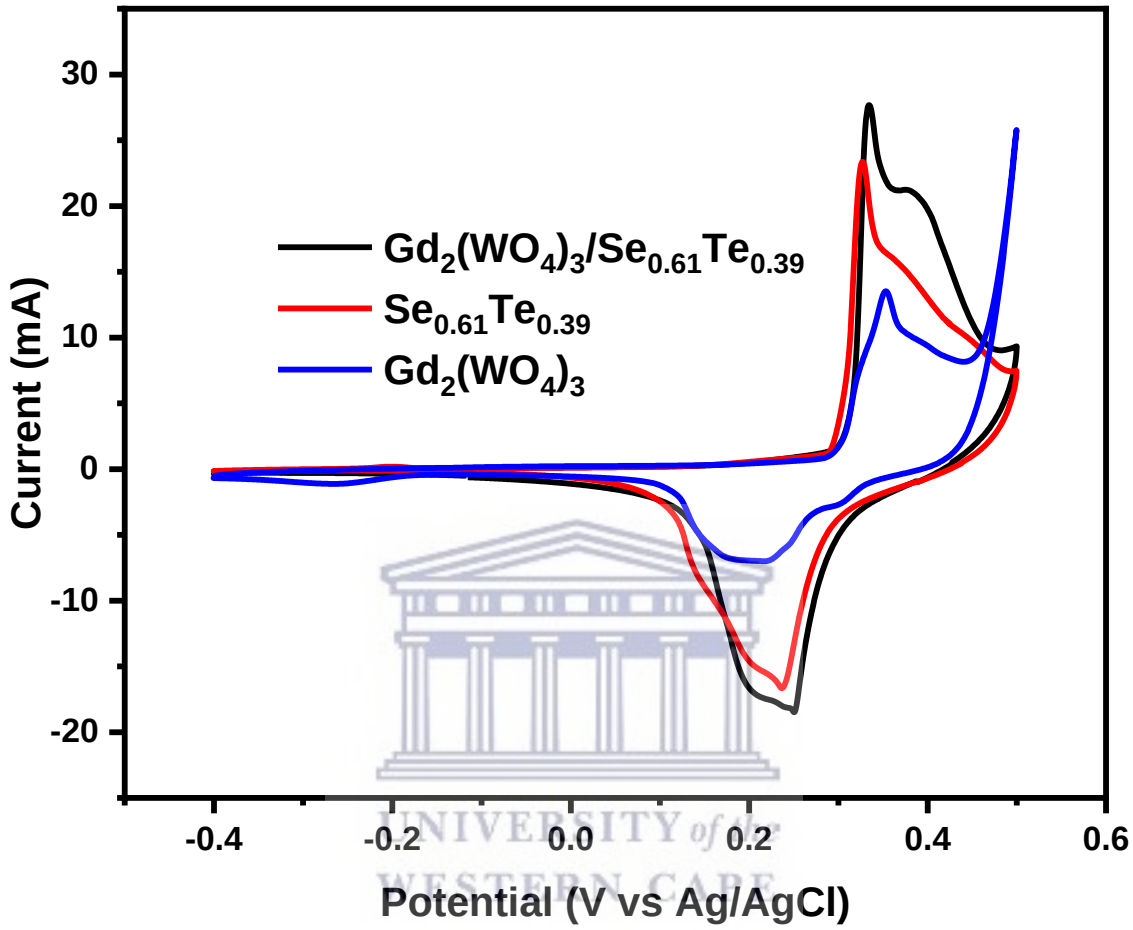


**Figure 4.7:** Cyclic voltammograms for $Gd_2(WO_4)_3$, $Se_{0.61}Te_{0,39}$ and $Gd_2(WO_4)_3/Te_{0.39}Se_{0.61}$ in 2 M KOH at 10 $mVs^{-1}$.

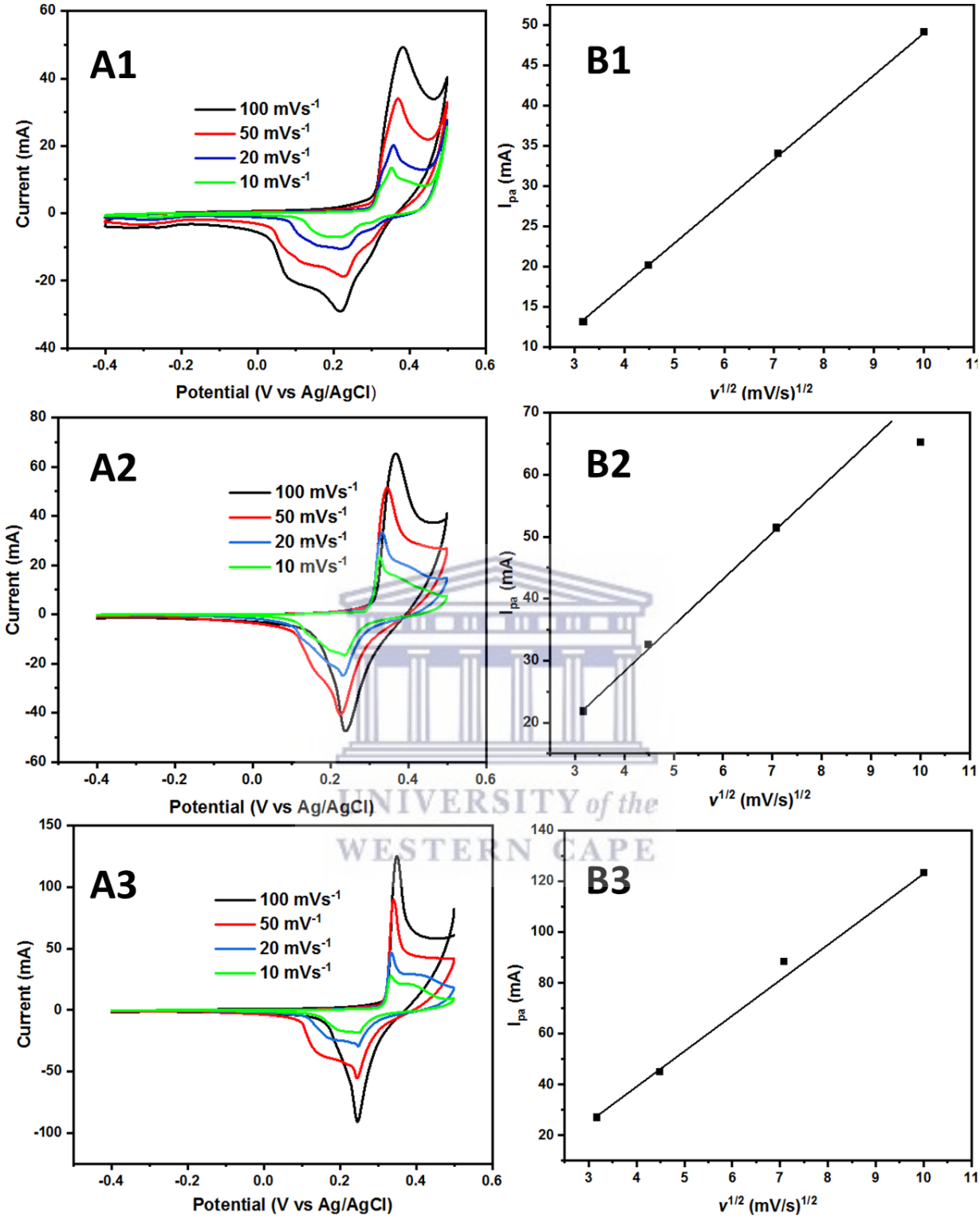




**Figure 4.8:** Multi-scan rates cyclic voltammograms of (A1) $Gd_2(WO_4)_3$ (A2) $Te_{0.39}Se_{0.61}$ (A3) $Gd_2(WO_4)_3/Te_{0.39}Se_{0.61}$ at scan rates 10 – 100 $mVs^-$ in 2 M KOH and (B1-B3) corresponding $I_{pa}$ proportion to the square root of scan rates.

examining the synthesized materials intrinsic charge storage kinetics. This was done with the aid of the method reported by Trasatti and co-workers, which is described by the following equation:

$$q\,(v) = q_{\infty} + kv^{-1/2} \quad (23)$$

where $q$ (v) is the total measured voltammetric charge, $q_{\infty}$ is the charge stored at high scanning rate, $k$ is a constant and $kv^{-1/2}$ represents charge storage that is related to semi-infinite diffusion. According to equation 16, the instant charge storage at the outer electrode surface is independent of the scanning rate (nondiffusion-controlled processes, associated with capacitive and pseudocapacitive electrode), while at the inner electrode surfaces the charge storage occurs via diffusion-controlled processes (battery-like electrode) [23-25]. The relationship between the current response (i) and scan rate (v) is given by the sum of surface-controlled and diffusion-controlled currents, and can be described by the following equation:

$$i = i_{capacitive} + i_{diffusion} = av^{b} \quad (24)$$



where "a" and "b" are adjustable parameters in the equation. Generally, by looking at power law dependence on equation 21, allows for a quick determination of the storage kinetics of the electrode. Figure 4.8, highlights the effect of scan rates on the oxidation-reduction processes of the synthesized materials. All the synthesized materials show an increasing current response trend with the increasing scanning rates (Figure 4.8 (A1-A3)). The current peak response ($I_{pa}$) is proportional to the square root of scan rates (v) which reveals a diffusion-controlled process, a battery-like behaviour of the synthesized electrodes. The diffusion coefficient ($D$) was determined with the help of the rearranged Randles-Sevcik equation for all the synthesized materials (26).

$$D = (slope/2.69*10\text{^}5AC)\text{^}2 \quad (25)$$

where the slope is determined from the plot of $I_p$ vs square root of scanning rates, A is the surface area of the coated nickel foam which is 0.25 $cm^2$ and C is the concentration of the medium used (2 M). The results calculated are listed in Table 4. The smaller *D* value, the slower the electron transfer is. So the calculated diffusion values show that tellurium selenide-gadolinium tungsten oxide has the slower electron transfer when compared to gadolinium oxide and tellurium selenide.

**Table 4:** Calculation of diffusion coefficient of the synthesized materials.

| Electrode | Slope | Diffusion coefficient, D ($cm^2/s$) |
|---|---|---|
| $Gd_2(WO_4)_3$ | 0.0053 | $1.55 \times 10^{-15}$ |
| $Se_{0.61}Te_{0.39}$ | 0.0063 | $2.19 \times 10^{-15}$ |
| $Gd_2(WO_4)_3/Te_{0.39}Se_{0.61}$ | 0.0144 | $1.14 \times 10^{-14}$ |



#### 4.5.1.2 Galvanostatic Charge-Discharge

The charging and discharging behaviour of the synthesized materials was evaluated with a GCD method at a potential range of – 0.4 to 0.5 V under the current density ranging from 1.2 to 1.8 A $g^{-1}$. From GCD technique, we were able to determine the specific capacity. Since the synthesized material have a battery-like behaviour, then the specific capacity $Q_s$ (C $g^{-1}$) was calculated using equation 19.

$$Q_s = I\Delta t/m \quad (26)$$

where *I* (A) is the current density, $\Delta t$ is discharging time (s) and *m* is the deposited mass of an active species in a nickel foam.

Figure 4.9a shows GCD curves of $Gd_2(WO_4)_3$, $Se_{0.61}Te_{0.39}$ and $Gd_2(WO_4)_3/Se_{0.61}Te_{0.39}$ at a current density of 1.2 A $g^{-1}$ and their corresponding specific capacities calculated from the GCD curves. The GCD profiles of all the synthesized materials formed a sloping and plateau regions in the plot of potential vs time curves, which is one of the main characteristics of the battery-like electrodes [27]. The possible reasons behind such response could be attributed to the formation of solid solutions, and secondly, to the formation of two phased reactions. This behaviour of the synthesized materials correlates with the results seen for cyclic voltammetry which also revealed the battery-type electrodes behaviour. The calculated specific capacities values showed an increasing trend of the specific capacities with decreasing current densities (a trend usually observed for hybrid electrode materials for supercapacitors). The highest specific capacities were obtained at a low current density of 1.2 A $g^{-1}$ which were 64.3 C $g^{-1}$, 17.3 C $g^{-1}$ and 23.8 C $g^{-1}$ for $Gd_2(WO_4)_3$, $Se_{0.61}Te_{0.39}$ and $Gd_2(WO_4)_3/Se_{0.61}Te_{0.39}$, respectively. From the results, $Gd_2(WO_4)_3$ alone showed superior charging-discharging response compared to selenium telluride and the composite. Figure 4.10 shows the charging-discharging response of the synthesized particles at various current densities.

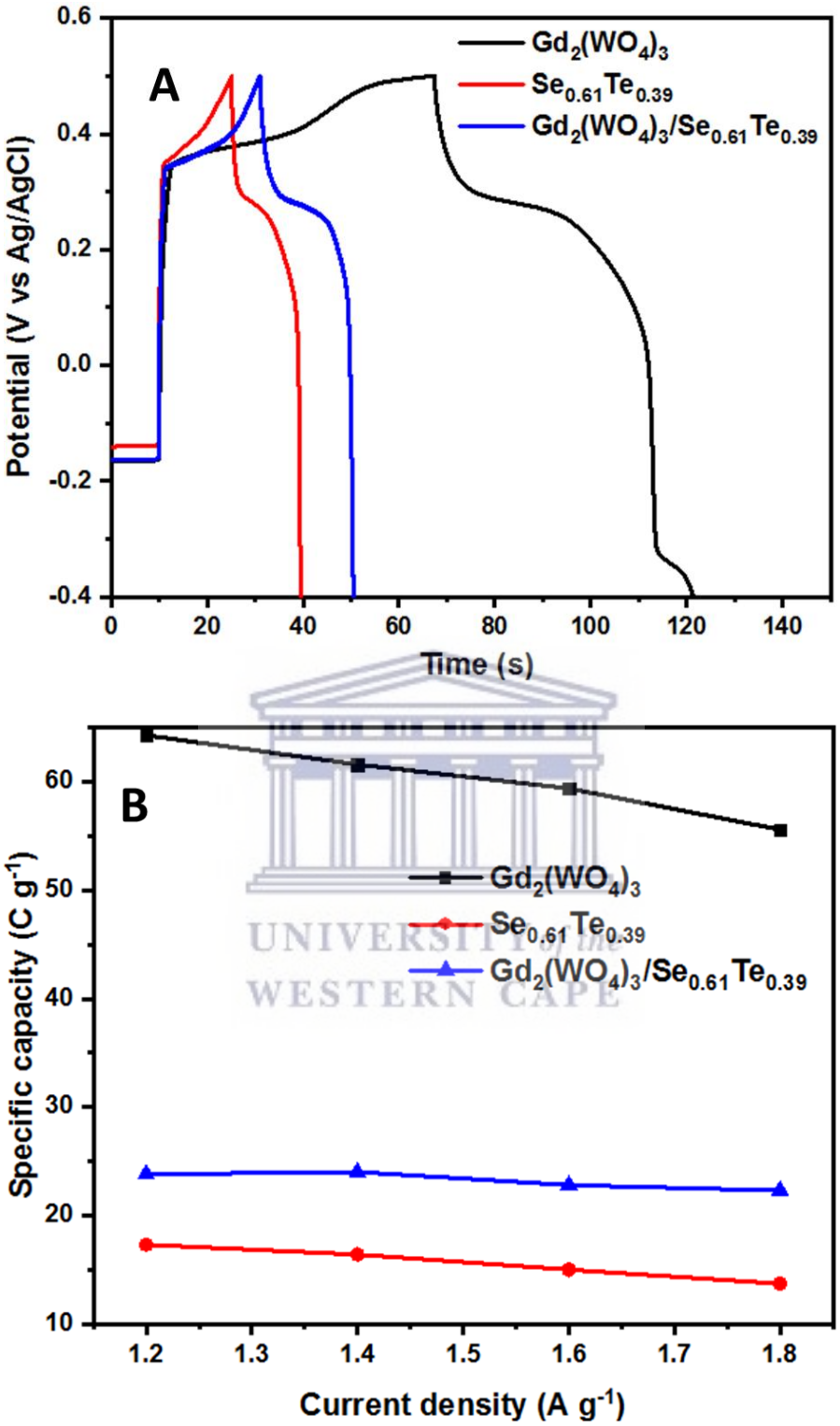


**Figure 4.9:** (A) GCD curves at current density of 1.2 A $g^{-1}$ of $Gd_2(WO_4)_3$, $Te_{0.39}Se_{0.61}$, $Gd_2(WO_4)_3/Te_{0.39}Se_{0.61}$ (B) $Q_s$ vs current density plot of $Gd_2(WO_4)_3$, $Te_{0.39}Se_{0.61}$, $Gd_2(WO_4)_3/Te_{0.39}Se_{0.61}$.

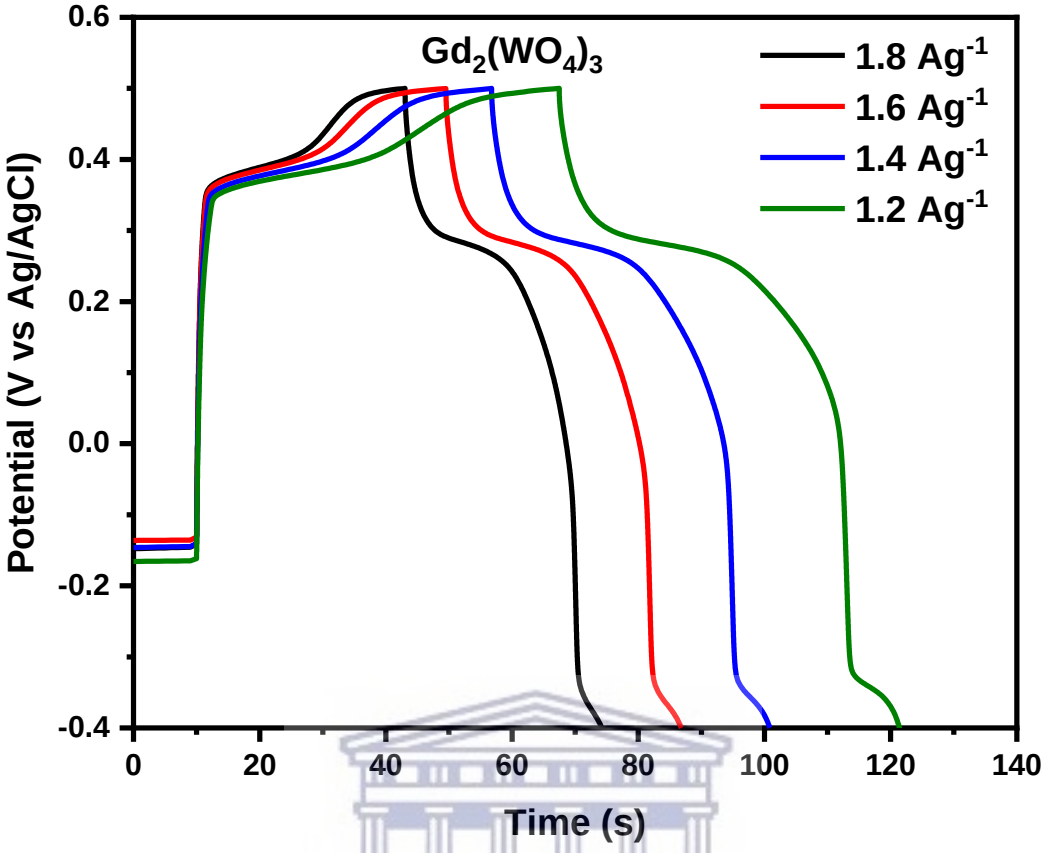


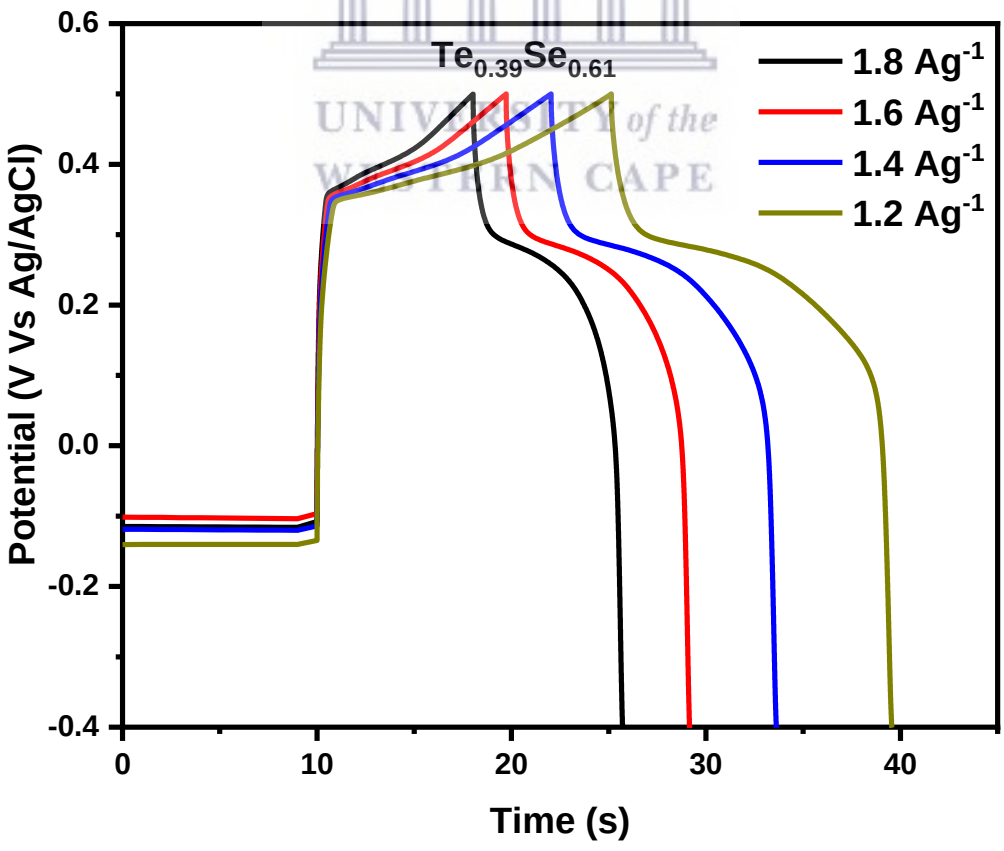

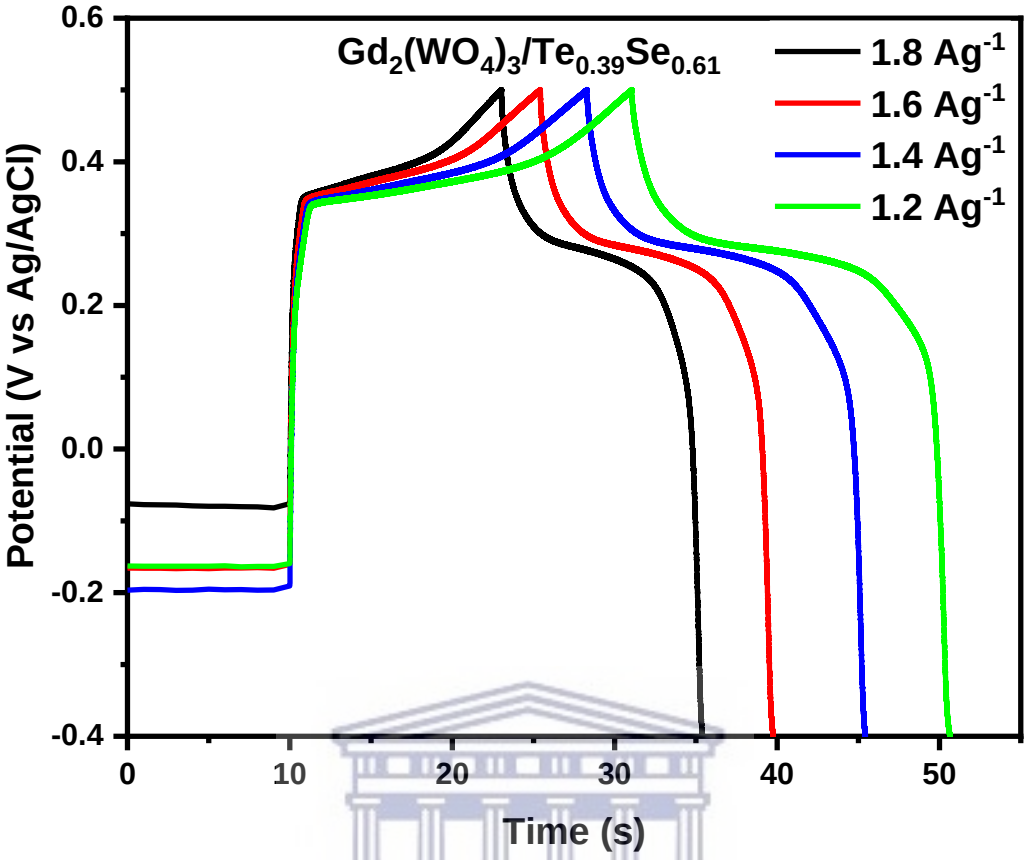


**Figure 4.10:** Shows GCD curves at various current density for $Gd_2(WO_4)_3$, $Te_{0.39}Se_{0.61}$, $Gd_2(WO_4)_3/Te_{0.39}Se_{0.61}$.



#### 4.5.1.3 Electrochemical Impedance Spectroscopy

Electrochemical Impedance Spectroscopy (EIS) is another important technique that used to characterize electrochemical cell in various frequency regimes in order to understand charge mobility and electron transfer mechanism at the interface of the electrode. Practically speaking, this technique measures resistance (R), capacitance (C) and inductance when a specific voltage is applied in an electrochemical cell. This technique is useful for both two and three electrode systems which also are distinguishable by the voltage applied (i.e. Direct current voltage or Alternating current voltage). In carrying out this technique, the EIS data was collected from a potentiostat apparatus and subjected under a mathematical model (i.e. fitted in an equivalent

electrical circuit) for its interpretation and analysis. The spectrum for the collected data can be plotted and presented in two ways i.e. the Nyquist plot and Bode plot. The EIS spectra was measured at an open circuit voltage (OCV) and figure 4.11 shows Nyquist plots and their fitted equivalent circuits for the synthesized nanoparticles. From the results, it is clearly observable that the nyquist plots show two distinct regions, (i) a semicircle that is observable in a high frequency range which is due to electron-limited process. (ii) a long tail situated at lower frequency region representing a Warburg component which is attributed to diffusion-limited process. This behaviour of the synthesised materials suggested that the electrochemical performance of these nanoparticles was in fact governed by two mechanisms, i.e. kinetics and diffusion processes. The behaviour and the Nyquist plot profiles seen for the synthesized materials confirmed the battery type behaviour which is in good agreement with the results observed in cyclic voltammetry and galvanostatic charge-discharge techniques.

The recorded values for the fitted equivalents circuits for the synthesized nanomaterials can be seen in table 8 below. For comparative studies, $R_{ct}$ (charge resistance transfer) values tells us about the charge transfer of a material. A material with low $R_{ct}$ value will have faster electron transfer and higher conductivity. The precursor material $Gd_2(WO_4)_3$ showed a higher $R_{ct}$ value of 1.341 $\boldsymbol{\Omega}$ compared to $Gd_2(WO_4)_3/Se_{0.61}Te_{0.39}$ and $Te_{0.39}Se_{0.61}$ (i.e. 0.7657 $\boldsymbol{\Omega}$ and 0.7154 $\boldsymbol{\Omega}$, respectively). This increased conductivity nature of the doped gadolinium tungsten oxide comes from the high conductivity nature of tellurium selenide which is also observed in cyclic voltammogram in figure 4.7.

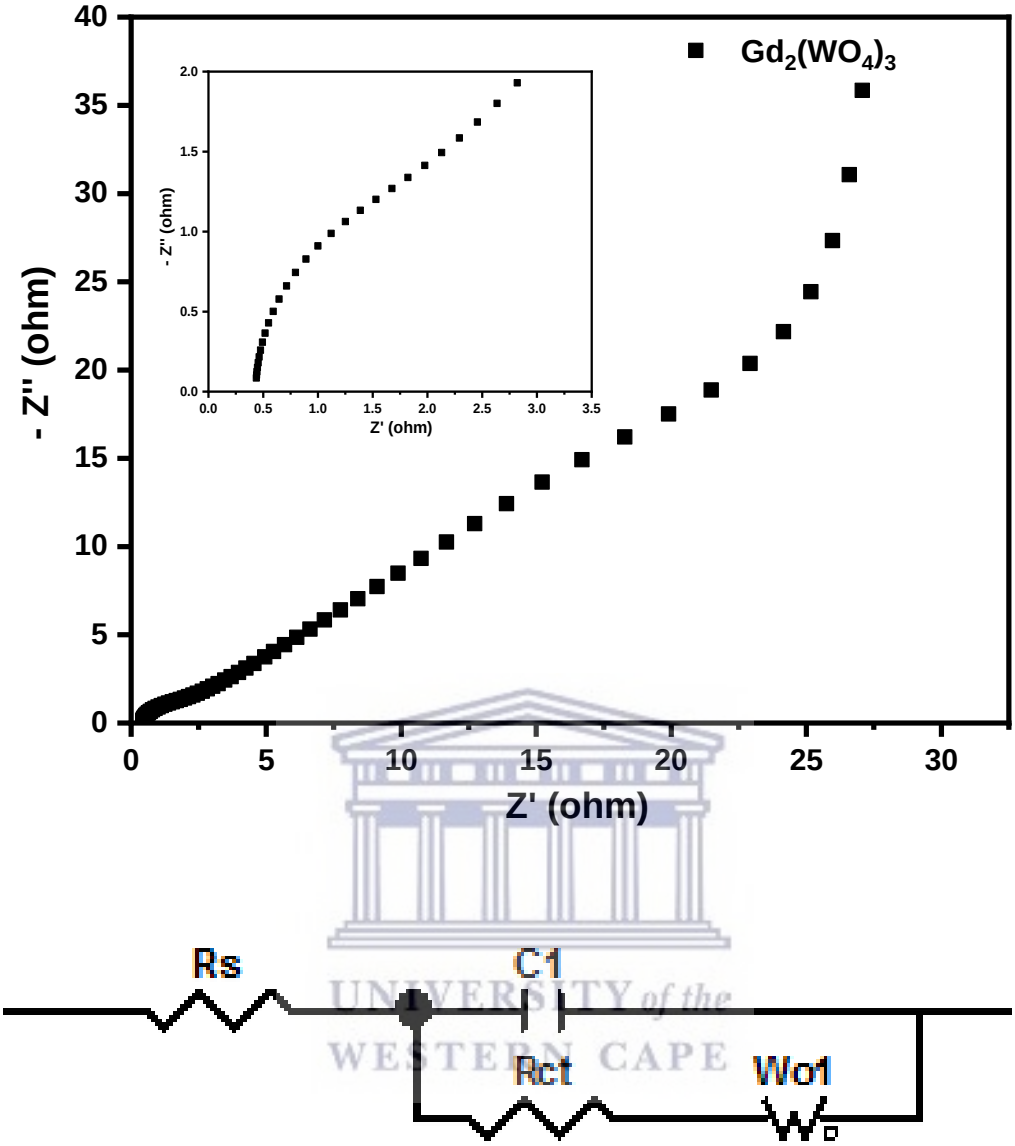

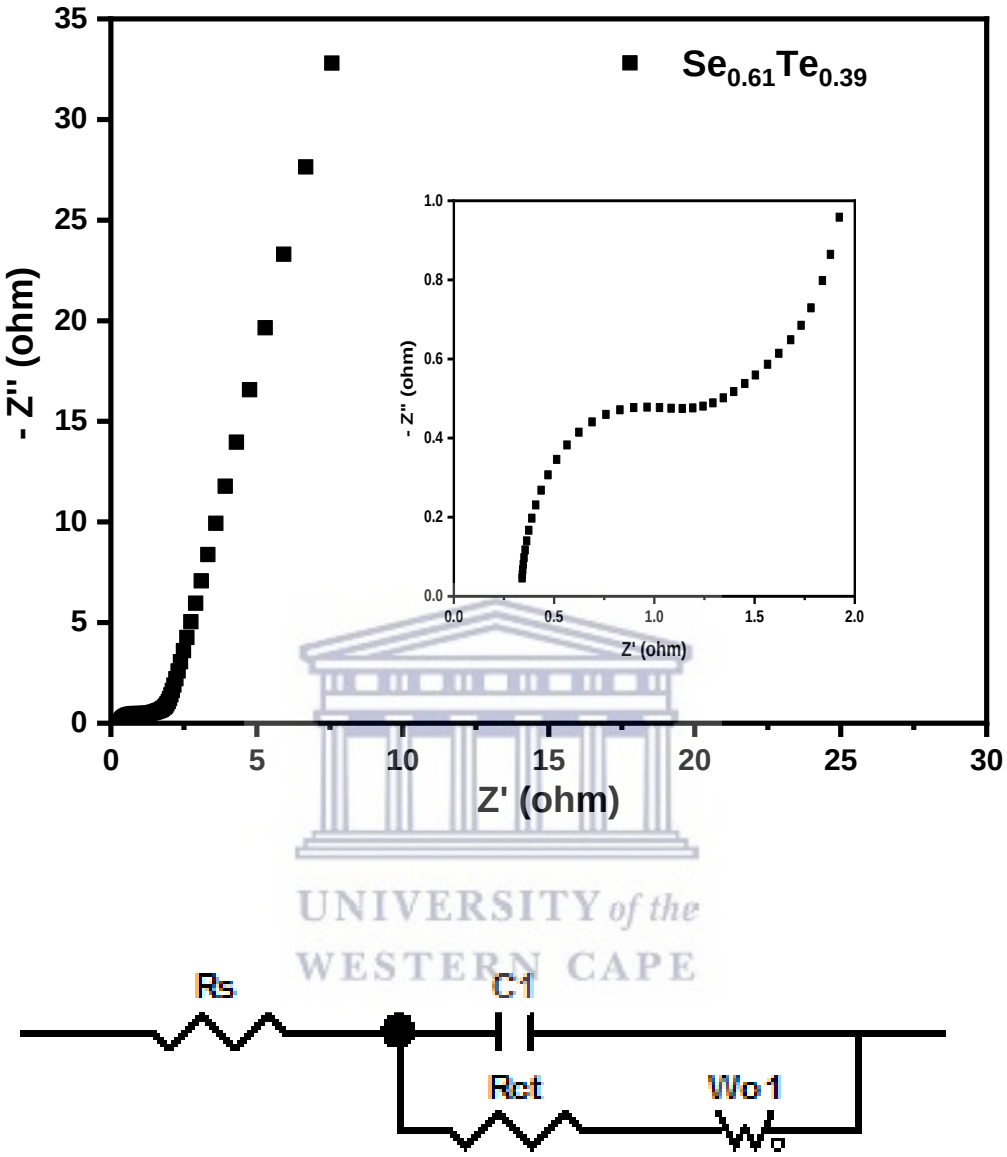

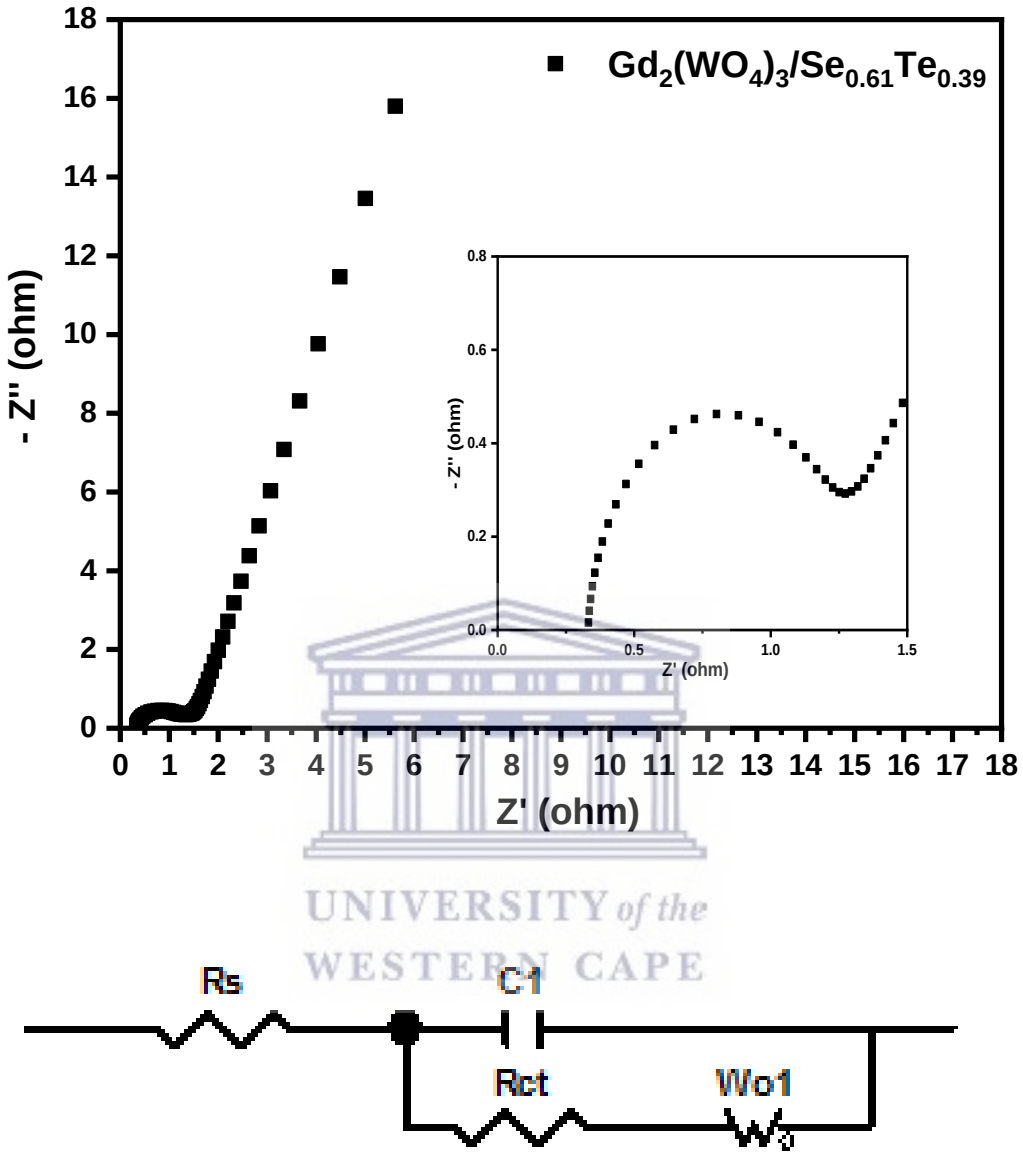


**Figure 4.11:** Shows Nyquist plots and their equivalent circuits for synthesized nanoparticles.

**Table 5:** Fitted equivalent circuit values for the synthesized nanoparticles.

| Material | $R_s$ (Ω) | $C_1$ (μF) | $R_{ct}$ (Ω) | W (Ω/√s) |
|---|---|---|---|---|
| $Gd_2(WO_4)_3$ | 0.4325 | 22.33 | 1.341 | 0.4967 |
| $Se_{0.61}Te_{0.39}$ | 0.3378 | 41.48 | 0.7154 | 0.4449 |
| $Gd_2(WO_4)_3/Se_{0.61}Te_{0.39}$ | 0.3386 | 43.19 | 0.7657 | 0.4185 |

## 4.6 References


[1] N. Sharma, M. Deepa, P. Varshney, and S. A. Agnihotry, "FTIR and absorption edge studies on tungsten oxide based precursor materials synthesized by sol-gel technique," *J. Non. Cryst. Solids*, vol. 306, no. 2, pp. 129–137, 2002, doi: 10.1016/S0022-3093(02)01134-1.

[2] Jin Li and Saki Kawi, "Synthesis, characterization and sensing application of novel semiconductor oxides," *Talanta*, vol. 45, no. 4, pp. 759–766, 1998, doi: 10.1016/S0039-9140(97)00295-6.

[3] Lay Gaik, Teoh Jiann, Shieh ,Wei Hao Lai, Ming Hung, and Min Hsiung Hon, "Structure and optical properties of mesoporous tungsten oxide," *J. Alloys Compd.*, vol. 396, no. 1–2, pp. 251–254, 2005, doi: 10.1016/j.jallcom.2004.12.005.

[4] Robert Geffers, Simone Sell, Rüdiger Cerff, and Reinhard Hehl, "The observation of cubic tungsten trioxide at high-temperature dehydration of tungstic acid hydrate," in *Solid State Ionics*, 2001, vol. 141–142, pp. 411–416, doi: 10.1016/S0167-2738(01)00806-2.

[5] Kazusuke Yamanaka1, Hiroshi Oakamoto, Hirokazu Kidou and Tetsuichi Kudo, "Peroxotungstic acid coated films for electrochromic display devices," *Jpn. J. Appl. Phys.*, vol. 25, no. 9 R, pp. 1420–1426, 1986, doi: 10.1143/JJAP.25.1420.

[6] Juan Xu ,Taotao Ding, Jin Wang, Jun Zhang, Shuai Wang, Changqing Chen, Yanyan Fang, Zhihao Wu, Kaifu Huo, and Jiangnan Dai, "Tungsten Oxide Nanofibers Self-assembled Mesoscopic Microspheres as High-performance Electrodes for Supercapacitor," *Electrochim. Acta*, vol. 174, pp. 728–734, 2015, doi: 10.1016/j.electacta.2015.06.044.

[7] E. Salje, "/ 800 600 400," pp. 360–363, 1975.

[8] B. Desbat and J. C. Lassegues, “Infrared and Raman Study of $WO_3$ Tungsten $xH_2O$ Tungsten Trioxide Hydrates Trioxides and $WO_3$,” vol. 247, pp. 235–247, 1987.

[9] Vaibhav Lokhande, Abhishek Lokhande, Gon Namkoong, Jin Hyeok Kim, and Taeksoo Ji, “Charge storage in $WO_3$ polymorphs and their application as supercapacitor electrode material,” *Results Phys.*, vol. 12, no. February 2019, pp. 2012–2020, 2019, doi: 10.1016/j.rinp.2019.02.012.

[10] Biyin Qin, Yan Bai, Yanhui Zhou, Jie Liu, Xinyuan Xie, and Wenjie Zheng, “Structure and characterization of $TeO_2$ nanoparticles prepared in acid medium,” *Mater. Lett.*, vol. 63, no. 22, pp. 1949–1951, 2009, doi: 10.1016/j.matlet.2009.06.018.

[11] Han Li., “Facile electrochemical synthesis of tellurium nanorods and their photoconductive properties,” *Cryst. Res. Technol.*, vol. 47, no. 10, pp. 1069–1074, 2012, doi: 10.1002/crat.201200273.

[12] Gianfranco Carotenuto, Mariano Palomba, Sergio De Nicola, Giuseppina Ambrosone, and Ubaldo Coscia, “Structural and Photoconductivity Properties of Tellurium/PMMA Films,” *Nanoscale Res. Lett.*, vol. 10, no. 1, 2015, doi: 10.1186/s11671-015-1007-z.

[13] Mousavi-Kamazani and Salavati-Niasari, “Synthesis, characterization, and optical properties of Te, $Te/TeO_2$ and $TeO_2$ nanostructures: Via a one-pot hydrothermal method,” *RSC Adv.*, vol. 6, no. 75, pp. 71472–71480, 2016, doi: 10.1039/c6ra10770b.

[14] Sobhani-Nasab and Rahimi-Nasrabadi, “Evaluation of supercapacitive behavior of samarium tungstate nanoparticles synthesized via sonochemical method,” *J. Mater. Sci. Mater. Electron.*, vol. 28, no. 12, pp. 8588–8595, 2017, doi: 10.1007/s10854-017-6582-6.

[15] Yang Liu, Jie Li, Wenzhang Li, Yahui Yang, Yaomin Li, and Qiyuan Chen, “Enhancement of the Photoelectrochemical Performance of $WO_3$ Vertical Arrays Film

for Solar Water Splitting by Gadolinium Doping," *J. Phys. Chem. C*, vol. 119, no. 27, pp. 14834–14842, 2015, doi: 10.1021/acs.jpcc.5b00966.

[16] Weichun Huang, Ye Zhang, Qi You, Pu Huang, Yunzheng Wang, Ziyin Huang, Yanqi Ge, Leiming Wu, Zhijun Dong, Xiaoyu Dai, Yuanjiang Xiang, Jianqing Li, Xiuwen Zhang, and Han Zhang, "Enhanced Photodetection Properties of Tellurium@Selenium Roll-to-Roll Nanotube Heterojunctions," *Small*, vol. 15, no. 23, pp. 1–10, 2019, doi: 10.1002/smll.201900902.

[17] Wen-Jie Lan, Shu-Hong Yu, Hai-Sheng Qian, and Yong Wan, "Dispersibility, stabilization, and chemical stability of ultrathin tellurium nanowires in acetone: Morphology change, crystallization, and transformation into $TeO_2$ in different solvents," *Langmuir*, vol. 23, no. 6, pp. 3409–3417, 2007, doi: 10.1021/la063272+.

[18] Luke Geoffrion and Grégory Guisbiers, "Physico-chemical properties of selenium-tellurium alloys across the scales," *Nanoscale Adv.*, vol. 3, no. 14, pp. 4254–4270, 2021, doi: 10.1039/d1na00087j.

[19] Pieer Atanasov, Jean Perriere, and Rebeek Defourneau, "Composition, structural and electrical properties of thin films prepared by laser ablation of neodymium-doped potassium gadolinium tungstate," *Thin Solid Films*, vol. 515, no. 5, pp. 3052–3056, 2007, doi: 10.1016/j.tsf.2006.08.018.

[20] A. Lacinska, J. Rushton, S. Burgess, E. A. Deady, and G. Turner, "The effect of x-ray energy overlaps on the microanalysis of chevkinite," *Minerals*, vol. 11, no. 10, 2021, doi: 10.3390/min11101063.

[21] P. L. Roeder, "Use of Calculated Peak-Overlap," *Can. Mineral.*, vol. 23, pp. 263–271, 1985.

[22] Mohsin Ganaie and Zulfequar, "Structural, electrical and dielectric properties of CNT doped SeTe glassy alloys," *Mater. Chem. Phys.*, vol. 177, pp. 455–462, 2016, doi:

10.1016/j.matchemphys.2016.04.053.

[23] Jagannatha Reddy, and Anil Kumar, "Synthesis, structural and spectroscopic investigation of $Gd_2(WO_4)_3$ phosphor," *J. Phys. Conf. Ser.*, vol. 1644, no. 1, 2020, doi: 10.1088/1742-6596/1644/1/012049.

[24] Rahimi-Nasrabadi, "Optimizing the procedure for the synthesis of nanoscale gadolinium(III) tungstate as efficient photocatalyst," *J. Mater. Sci. Mater. Electron.*, vol. 28, no. 4, pp. 3780–3788, 2017, doi: 10.1007/s10854-016-5988-x.

[25] Dama Bojang and Ho Shing Wu, "Characterization of Electrode Performance in," *Catalysts*, vol. 10, no. Cv, p. 782, 2020.

[26] B. De, S. Banerjee, K. D. Verma, T. Pal, P. K. Manna, and K. K. Kar, "*Transition metal oxides as electrode materials for supercapacitors"*, vol. 302. Springer International Publishing, 2020.

[27] Linpo Yu and George Zheng Chen, "Supercapatteries as High-Performance Electrochemical Energy Storage Devices," *Electrochem. Energy Rev.*, vol. 3, no. 2, pp. 271–285, 2020, doi: 10.1007/s41918-020-00063-6.

[28] Michael Hu and Ting Zhu, "Semiconductor Nanocrystal Quantum Dot Synthesis Approaches Towards Large-Scale Industrial Production for Energy Applications," *Nanoscale Res. Lett.*, vol. 10, no. 1, pp. 1–15, 2015, doi: 10.1186/s11671-015-1166-y.

[29] Jing Han, Hong-Yan Zeng, Xi Cao and Chao-Rong Chen, "Cycling stability of iron-based layered double hydroxide thin-films for battery-type electrode materials," *J. Mater. Sci. Mater. Electron.*, vol. 28, no. 3, pp. 2754–2762, 2017, doi: 10.1007/s10854-016-5855-9.

# Chapter 5

# 5. Conclusion and recommendation

## 5.1 Conclusion

In this study we explored the potential application of a newly developed electrode material for a supercapacitor by incorporating a double chalcogenide into gadolinium tungsten oxide ($Gd_2(WO_4)_3/Te_{0.39}Se_{0.61}$). In summary, the synthesis was carried successfully with a hydrothermal route. Firstly, $Gd_2(WO_4)_3$ was synthesized as a parent material followed by a synthesis of $Te_{0.39}Se_{0.61}$. Then tellurium selenide was incorporated into gadolinium tungsten oxide to form $Gd_2(WO_4)_3/Te_{0.39}Se_{0.61}$ using one pot method in an autoclave. The parent material $Gd_2(WO_4)_3$, gave XRD results with the main diffraction peaks at $2\theta$ = 20.3°, 22.9° and 27° corresponding to (001), (002) and (102) reflections, respectively. After incorporation of $Te_{0.39}Se_{0.61}$, the main diffraction peaks were still present with emergence of new diffraction peaks which confirmed the incorporation of selenium telluride. The temperature variation for annealing revealed that $Gd_2(WO_4)_3/Te_{0.39}Se_{0.61}$ becomes amorphous at lower temperatures of up to 600 ° C but becomes well crystalline at 800 ° C (observed by well separated sharp peaks). Furthermore, the FT-IR of $Gd_2(WO_4)_3/Te_{0.39}Se_{0.61}$ at 800 ° C showed shifted characteristic bands corresponding to both gadolinium tungsten oxide and selenium telluride with elimination of water molecules compared to the structure observed at 300 ° C. SEM image of $Gd_2(WO_4)_3$ showed a spherical morphology with a porous structure while that of $Gd_2(WO_4)_3/Te_{0.39}Se_{0.61}$ showed a cube like morphology. The elemental composition analysis by EDS for the synthesized $Gd_2(WO_4)_3$ and $Te_{0.39}Se_{0.61}$ showed that all the elements were present in the

structure but Se was undetected in the nanocomposite. The reason for this lies with the possibility of overlap between REE with selenium. EDS is unable to resolve the peak overlaps with Pr, Eu, Gd, Ho, Er, Tm, and Lu. The internal structure from HRTEM revealed a cubic structure for $Gd_2(WO_4)_3$, a combination of nanowires (Te) and spheres (Se) for $Te_{0.39}Se_{0.61}$ but for the nanocomposite there was no clear information about the internal structure. SAED patterns confirmed a single crystalline structure for $Gd_2(WO_4)_3$ while $Te_{0.39}Se_{0.61}$ was polycrystalline. Again the SAED pattern for nanocomposite confirmed that the structure was amorphous which was observed by unclear rings. The optical properties of the synthesized materials were studied with UV-vis and the band gap energy determined by means of Tauc plot. The band gap energy values gave a clear indication as to whether the synthesized nanoparticles can be used as materials for supercapacitors. The band gap for gadolinium tungsten oxide was determined to be 3.28 eV but after incorporation tellurium selenide, the band gap increased to 3.39 eV. This prevents $Te_{0.39}Se_{0.61}$ to be used as the supercapacitor material. The electrochemical response of the materials was studied using CV, GCD and EIS. This was done with a three electrode system where a Ni foam was used as a current collector and 2 M KOH was used as an aqueous electrolyte. From the results, all the materials were scan depended meaning the current response observed was increasing with the increasing scan rate, the current peak ratio was not equal to 1 which suggested a quasi-reversible system for all the materials. Furthermore, the charge storage mechanism at the inner electrode surfaces occurred via diffusion-controlled processes which suggested that the electrode materials were behaving in a battery-like electrodes. The highest calculated specific capacitances from GCD were achieved at low current density of 1.2 A $g^{-1}$ which were 64.3 C $g^{-1}$, 17.3 C $g^{-1}$ and 23.8 C $g^{-1}$ for $Gd_2(WO_4)_3$, $Te_{0.39}Se_{0.61}$ and the composite material, respectively. Low $R_{ct}$ values from EIS give an indication that the material is more conductive compared to others and vice versa. The

$R_{ct}$ values were determined to be 1.341 $\boldsymbol{\Omega}$, 0.7154 $\boldsymbol{\Omega}$ and 0.7657 $\boldsymbol{\Omega}$ for $Gd_2(WO_4)_3$, $Te_{0.39}Se_{0.61}$ and $Gd_2(WO_4)_3/Te_{0.39}Se_{0.61}$, respectively. Even though $Gd_2(WO_4)_3$ behaves like a battery-type electrode, the composite is more pseudo capacitive but not suitable as an electrode for a supercapacitor.

### 5.2 Recommendation

Further investigation of chalcogenide doped gadolinium tungsten oxide still need to be done. These aspects are:

- To achieve a well doped material it is advisable to mix the two already made powders of the precursors (parent material and dopant) with a suitable solvent to carry out the hydrothermal treatment at high temperatures instead of mixing the two solution that represent the precursor materials. This is due to the fact that that the resulting structure might be amorphous even though all the elements making the composition might be present. Meaning mixing the two solution might result in an uncontrolled structure.
- The annealing temperature for selenium telluride doped gadolinium oxide should be in the range 800-1000 ° C.
- Two electrode configuration for evaluating the electrochemical performance should be conducted to evaluate the behaviour of the parent material and the doped composite in a full cell conditions.

**Appendix: Figure 6a**

SPRINGER NATURE LICENSE

TERMS AND CONDITIONS

Feb 02, 2022

This Agreement between Mr. Sinethemba Kaba ("You") and Springer Nature ("SpringerNature") consists of your license details and the terms and conditions provided by SpringerNature and Copyright Clearance Center.

| | |
|---|---|
| License Number | 5240120971764 |
| License date | Feb 01, 2022 |
| Licensed ContentPublisher | Springer Nature |
| Journal of Materials Science | Materials in Electronics |
| Licensed Content Title | Evaluation of supercapacitive behaviour of samarium tungstate nanoparticles synthesized via sonochemical method |
| Licensed Content Author | Ali Sobhani-Nasab et al |
| Licensed Content Date | Mar 28, 2017 |
| Type of Use | Thesis/Dissertation |
| Requestor type | academic/university or research institute |
| Format | print and electronic |
| Portion | figures/tables/illustrations |

Number of figures/tables/illustrations1

Will you be translating? no

2/2/22, 9:16 PM Right slink Printable License

https://s100.copyright.com/CustomerAdmin/PLF.jsp?ref=bf2ebf7f-b0f0-4f1a-973c-aeaa1c8197e1 2/5

| | |
|---|---|
| Circulation/distribution | 1 - 29 |
| Author of this SpringerNature content | no |
| Title | tellurium selenide-gadolinium tungsten oxide quantum dot material for supercapacitor |
| Institution name | University of Western Cape |
| Expected presentation date | Feb 2022 |
| Order reference number | 1961 |
| Portions | figure 6a |
| Requestor Location | Mr. Sinethemba Kaba<br>5934 Polar park, Dimbaza<br>Bisho, Eastern Cape 5671<br>South Africa |
| Attn | Mr. Sinethemba Kaba |
| Customer VAT ID | ZA0637892258 |

Total 0.00 USD

Terms and Conditions

Springer Nature Customer Service Centre GmbH

Terms and Conditions

This agreement sets out the terms and conditions of the licence (the Licence) between you and Springer Nature Customer Service Centre GmbH (the Licensor). By clicking ‘accept' and completing the transaction for the material (Licensed Material), you also confirm your acceptance of these terms and conditions.

1.Grant of License

1. 1. The Licensor grants you a personal, non-exclusive, non-transferable, world-wide licence to reproduce the Licensed Material for the purpose specified in your order only. Licences are granted for the specific use requested in the order and for no other use, subject to the conditions below.





1. 2.

The Licensor warrants that it has, to the best of its knowledge, the rights to license reuse of the Licensed Material. However, you should ensure that the material you are requesting is original to the Licensor and does not carry the copyright of another entity (as credited in the published version).

1. 3. If the credit line on any part of the material you have requested indicates that itwas reprinted or adapted with permission from another source, then you should also seek permission from that source to reuse the material.

2. Scope of Licence

2. 1. You may only use the Licensed Content in the manner and to the extent permitted by these Ts & Cs and any applicable laws.

2. 2. A separate licence may be required for any additional use of the Licensed Material, e.g. where a licence has been purchased for print only use, separate permission must be obtained for electronic re-use. Similarly, a licence is only valid in the language selected and does not apply for editions in other languages unless additional translation rights have been granted separately in the licence. Any content owned by third parties are expressly excluded from the licence.



2. 3. Similarly, rights for additional components such as custom editions and derivatives require additional permission and may be subject to an additional fee. Please apply to Journalpermissions@springernature.com/bookpermissions@springernature.com for these rights.

2. 4. Where permission has been granted free of charge for material in print, permission may also be granted for any electronic version of that work, provided thatthe material is incidental to your work as a whole and that the electronic version is essentially equivalent to, or substitutes for, the print version.

2. 5. An alternative scope of licence may apply to signatories of the STM Permissions Guidelines, as amended from time to time.

3. Duration of Licence

3. 1. A licence for is valid from the date of purchase ('Licence Date') at the end of the relevant period in the below table: Scope of Licence, Duration of Licence, Post on a website, 12 months, Presentations, 12 months, Books and journals, Lifetime of the edition in the language purchased.

4. Acknowledgement

4. 1. The Licensor's permission must be acknowledged next to the Licenced Material in print. In electronic form, this acknowledgement must be visible at the same time as the figures/tables/illustrations or abstract, and must be hyperlinked to the journal/book's homepage. Our required acknowledgement format is in the Appendix below.



5. Restrictions on use

5. 1. Use of the Licensed Material may be permitted for incidental promotional use and minor editing privileges e.g. minor adaptations of single figures, changes of format, colour and/or style where the adaptation is credited as set out in Appendix 1 below. Another changes including but not limited to, cropping, adapting, omitting material that affect the meaning, intention or moral rights of the author are strictly prohibited.

5. 2. You must not use any Licensed Material as part of any design or trademark.

5. 3. Licensed Material may be used in Open Access Publications (OAP) before publication by Springer Nature, but any Licensed Material must be removed from OAP sites prior to final publication.

6. Ownership of Rights

6. 1. Licensed Material remains the property of either Licensor or the relevant third partyand any rights not explicitly granted herein are expressly reserved.

7. Warranty

IN NO EVENT SHALL LICENSOR BE LIABLE TO YOU OR ANY OTHER PARTY ORANY OTHER PERSON OR FOR ANY SPECIAL, CONSEQUENTIAL, INCIDENTALOR INDIRECT DAMAGES, HOWEVER CAUSED, ARISING OUT OF OR INCONNECTION WITH THE DOWNLOADING, VIEWING OR USE OF THEMATERIALS REGARDLESS OF THE FORM OF ACTION, WHETHER FOR BREACHOF CONTRACT, BREACH OF WARRANTY, TORT, NEGLIGENCE, INFRINGEMENTOR OTHERWISE (INCLUDING, WITHOUT LIMITATION, DAMAGES BASED ONLOSS OF PROFITS, DATA, FILES, USE, BUSINESS OPPORTUNITY OR CLAIMS OFTHIRD PARTIES), AND

WHETHER OR NOT THE PARTY HAS BEEN ADVISED OF THE POSSIBILITY OFSUCH DAMAGES. THIS LIMITATION SHALL APPLY NOTWITHSTANDING ANYFAILURE OF ESSENTIAL PURPOSE OF ANY LIMITED REMEDY PROVIDEDHEREIN.

8. Limitations

8. 1. *BOOKS ONLY:* Where ‘reuse in a dissertation/thesis' has been selected the following terms apply: Print rights of the final author's accepted manuscript (for clarity, NOT the published version) for up to 100 copies, electronic rights for use only on personal website or institutional repository as defined by the Sherpa guideline(www.sherpa.ac.uk/romeo/).

8. 2. For content reuse requests that qualify for permission under the STM Permissions Guidelines, which may be updated from time to time, the STM Permissions Guidelines supersede the terms and conditions contained in this licence.

9. Termination and Cancellation

2/2/22, 9:16 PM Rights Link Printable License

https://s100.copyright.com/CustomerAdmin/PLF.jsp?ref=bf2ebf7f-b0f0-4f1a-973c-aeaa1c8197e1 5/5



9. 1. Licences will expire after the period shown in Clause 3 (above).

9. 2. Licensee reserves the right to terminate the Licence in the event that payment is not received in full or if there has been a breach of this agreement by you.

Appendix 1 — Acknowledgements: For Journal Content: Reprinted by permission from [the Licensor]: [Journal Publisher (e.g. Nature/Springer/Palgrave)] [JOURNAL NAME] [REFERENCE CITATION (Article name, Author(s) Name), [COPYRIGHT] (year of publication)

For Advance Online Publication papers: Reprinted by permission from [the Licensor]: [Journal Publisher (e.g. Nature/Springer/Palgrave)] [JOURNAL NAME] [REFERENCE CITATION

(Article name, Author(s) Name), [COPYRIGHT] (year of publication), advance online publication, day month year (doi: 10.1038/sj.[JOURNAL ACRONYM].)

For Adaptations/Translations: Adapted/Translated by permission from [the Licensor]: [Journal Publisher (e.g. Nature/Springer/Palgrave)] [JOURNAL NAME] [REFERENCE CITATION (Article name, Author(s) Name), [COPYRIGHT] (year of publication)

Note: For any republication from the British Journal of Cancer, the following credit line style applies:

Reprinted/adapted/translated by permission from [the Licensor]: on behalf of Cancer Research UK: [Journal Publisher (e.g. Nature/Springer/Palgrave)] [JOURNALNAME] [REFERENCE CITATION (Article name, Author(s) Name), [COPYRIGHT] (year of publication)

For Advance Online Publication papers: Reprinted by permission from The [the Licensor]: on behalf of Cancer Research UK: [Journal Publisher (e.g. Nature/Springer/Palgrave)] [JOURNAL NAME] [REFERENCE CITATION (Article name, Author(s) Name), [COPYRIGHT] (year of publication), advance online publication, day month year (doi: 10.1038/sj.[JOURNAL ACRONYM])

For Book content:

Reprinted/adapted by permission from [the Licensor]: [Book Publisher (e.g. Palgrave Macmillan, Springer etc.) [Book Title] by [Book author (s)] [COPYRIGHT] (year of publication)

Other Conditions: Version 1.3

Questions?

customercare@copyright.com

or +1-855-239-3415 (toll free in the US) or+1-978-646-2777.